Decline of the lunar core dynamo

Sonia M. Tikoo [a,*], Benjamin P. Weiss [a], William S. Cassata [b], David L. Shuster [c,d], Jérôme Gattacceca [a,e], Eduardo A. Lima [a], Clément Suavet [a], Francis Nimmo [f], Michael D. Fuller [g]

[a] Department of Earth, Atmospheric, and Planetary Sciences, Massachusetts Institute of Technology (MIT), 77 Massachusetts Avenue, Cambridge, MA 02139, USA
[b] Chemical Sciences Division, Lawrence Livermore National Laboratory, 7000 East Avenue, Livermore, CA 94550, USA
[c] Department of Earth and Planetary Science, University of California, Berkeley, CA 94720, USA
[d] Berkeley Geochronology Center, 2455 Ridge Road, Berkeley, CA 94709, USA
[e] Centre Européen de Recherche et d'Enseignement, UM34, CNRS/Université Aix-Marseille, France
[f] Department of Earth and Planetary Sciences, University of California, Santa Cruz, CA 95064, USA
[g] University of Hawaii at Manoa, Honolulu, HI 96822, USA

A B S T R A C T

Recent analyses of Apollo samples have demonstrated that a core dynamo existed on the Moon between at least 4.25 and 3.56 billion years ago (Ga) with surface field intensities reaching ∼70 μT. However, it is unknown when the Moon's magnetic field declined. Determining the temporal evolution of the dynamo is important because it constrains secular changes in power at the lunar core–mantle boundary and, by implication, the Moon's thermal and orbital evolution and the field generation mechanism. Here we present paleomagnetic data from several younger mare basalts which demonstrate that the surface magnetic field had declined precipitously to <∼4 μT by 3.19 Ga. It is currently unclear whether such a rapid decrease in field strength reflects either the cessation of the dynamo during this period or its persistence beyond 3.19 Ga in a drastically weakened state.

© 2014 Elsevier B.V. All rights reserved.

1. Introduction

A variety of geophysical and geochemical data have established that the Moon is a differentiated body with a small (∼350 km diameter) liquid outer core (Weber et al., 2011; Wieczorek et al., 2006). Remanent magnetization in lunar rocks and the crust indicates that there were substantial ancient magnetic fields on the surface of the Moon (Fuller and Cisowski, 1987). Although impact-generated plasmas are a potential source of magnetic fields (Hood and Artemieva, 2008), recent paleomagnetic studies of Apollo samples and the association of central magnetic anomalies with Nectarian impact basins indicate that a lunar core dynamo existed between at least ∼4.25 and 3.56 billion years ago (Ga) with surface field intensities of ∼30–110 μT (Cournède et al., 2012; Garrick-Bethell et al., 2009; Garrick-Bethell and Weiss, 2013; Hood, 2011; Shea et al., 2012; Suavet et al., 2013). The lack of detailed paleomagnetic studies of lunar rocks younger than 3.56 Ga has

meant that it is currently unclear when the dynamo weakened and ultimately ceased (Fuller and Cisowski, 1987; Tikoo et al., 2012).

The intensity and longevity of thermally convective dynamos depend on the superadiabatic heat flux at the core–mantle boundary (Christensen et al., 2009). However, estimates for this adiabatic threshold are poorly constrained. Lunar thermal evolution models suggest that a thermally convective lunar dynamo can persist until sometime between ∼3.7 and ∼2.5 Ga for adiabatic thresholds ranging from 10 to 3 mW m^{-2} (Evans et al., 2014; Konrad and Spohn, 1997; Laneuville et al., 2013; Stegman et al., 2003). This has motivated alternative proposals that the core dynamo was mechanically powered by differential rotation of the lunar mantle, driven by either large impacts (Le Bars et al., 2011) or precession (Dwyer et al., 2011), or thermochemically driven by core crystallization (Laneuville et al., 2014; Soderlund et al., 2013; Zhang et al., 2013). However, because impact-driven changes in rotation are unlikely to have generated a core dynamo after the final large basin-forming impact at 3.72 Ga (Suavet et al., 2013), the persistence of the dynamo until at least 3.56 Ga supports precession or core crystallization as the main field source at this time. By comparison, mantle precession (Dwyer et al., 2011) and core crystallization (Laneuville et al., 2014; Soderlund et al., 2013; Zhang et al., 2013) dynamos may be capable of persisting until as

* Corresponding author at: Department of Earth and Planetary Science, University of California, Berkeley, CA 94720, USA. Tel.: +1 573 382 6948; fax: +1 510 644 9201.
E-mail address: smtikoo@berkeley.edu (S.M. Tikoo).

late as a few hundred million years ago under certain conditions (Supplementary material).

Constraints on when the dynamo declined in intensity would constrain the power sources and, by implication, the field-generating mechanism(s) for the dynamo. In particular, given that at least thermally convective and perhaps also precession dynamo field intensities are thought to scale with the available (i.e., superadiabatic, not total) power (Christensen et al., 2009), evidence for a decline in the field intensity after 3.56 Ga could constrain the thermal and orbital evolution of the Moon.

Two key impediments to lunar paleomagnetic studies are that the majority of lunar samples have poor magnetic recording properties (Tikoo et al., 2012) and complex thermal and shock deformational histories (Supplementary material). Therefore, many earlier paleomagnetic studies are unreliable both in inferred paleointensities and age of magnetization. Consequently, since the end of the Apollo era, there have been two competing hypotheses about the state of the late lunar magnetic field. Fuller (1998) suggested that there was no evidence for a dynamo after 3.72 Ga, whereas Runcorn (1996) proposed that the dynamo persisted until at least ~3.2 Ga (the age of the youngest returned mare basalts). Distinguishing between these possibilities requires a combination of paleomagnetic and petrographic studies and thermochronometry to constrain the extent of post-formational shock and thermal processes that could have modified any primary magnetization in samples. Two recent studies of young (<3.56 Ga) samples did not come to firm conclusions about the origin of their natural remanent magnetization (NRM). Cournède et al. (2012) studied ~3.3 Ga mare basalt 12002, but did not confidently isolate a primary remanence (Supplementary material). Lawrence et al. (2008) suggested that the NRM of cataclastic anorthosite 60015 may not have been acquired from a dynamo field (i.e., their data imply any ambient field was <5 μT), but both this paleointensity constraint and the age to which it applies are uncertain because the sample may have been shocked or thermally demagnetized well after its ^{40}Ar/^{39}Ar plateau age of 3.46 Ga (Supplementary material). With the goal of resolving the state of the lunar dynamo at 3.2–3.3 Ga, we conducted a new paleomagnetic study of Apollo 12 and 15 mare basalts which accounts for secondary shock and thermal effects. Our goal is to constrain the paleointensity of the late lunar field.

2. Samples

We chose to focus on mare basalt samples 12022 and 15597 because Apollo-era analyses and our own measurements found that these rocks have unusually high fidelity magnetic recording properties relative to other young (<3.6 Ga) mare basalts (Supplementary material). Sample 12022 also offers a fortuitous opportunity for lunar paleomagnetic studies because it was sawn at Johnson Space Center (JSC) into multiple mutually oriented blocks in April and May 1970, just five months after return from the Moon (Supplementary material). These blocks were subsequently stored in unknown, almost certainly differing orientations without magnetic shielding. This early saw-cutting and subsequent long-term storage enables a test of whether NRM in 12022 was acquired as viscous remanent magnetization (VRM) contamination from long-term exposure to the terrestrial field (Supplementary material) or is pre-terrestrial in origin.

2.1. Petrographic descriptions and ages

12022 is a medium-grained porphyritic ilmenite basalt (Brett et al., 1971; James and Wright, 1972; McGee et al., 1977; Neal et al., 1994; Weill et al., 1971). The sample has an ^{40}Ar/^{39}Ar plateau age of 3.194 ± 0.025 Ga (Alexander et al., 1972; Supplementary material). The phenocrysts in 12022 are predominantly 1–2 mm
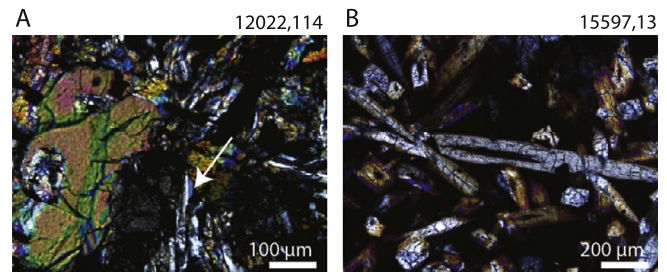

Fig. 1. Photographs of 30 μT thin sections in transmitted light with crossed polars. (A) 12022,114 and (B) 15597,13. White arrow points to a plagioclase crystal used for cooling rate determinations. Pyroxene is present as large phenocrysts displaying high order interference colors in sample 12022; it also appears as large laths within a glassy matrix in sample 15597.

diameter pyroxene crystals and ~300 μm diameter olivine crystals (Fig. 1A). Its matrix consists of 0.05–1 mm diameter feldspar laths, 30–200 μm long ilmenite laths, 600–800 μm diameter pyroxene grains and trace amounts of aluminosilicate glass.

15597 is a vitrophyric quartz-normative basalt (Ryder, 1985; Weigand and Hollister, 1973). It has whole-rock Rb and Sr isotope ratios consistent with a model age of ~3.3 Ga (Compston, 1972) and an ^{40}Ar/^{39}Ar plateau age of ~3.1–3.5 Ga (Kirsten et al., 1973). The sample contains elongated (up to 300 μm long) pyroxene phenocrysts in a brown glassy matrix with sparse vesicles ranging from 10 to 500 μm in size (Fig. 1B).

Our petrographic study indicates that both samples lack evidence for shock (peak pressures <5 GPa): plagioclase shows no mechanical twinning, fracturing, or alteration to maskelynite, and there is no undulatory extinction in olivine or pyroxene (Stöffler et al., 2006). Therefore, shock demagnetization or remagnetization of any existing primary thermoremanent magnetization (TRM) is likely modest and confined to low coercivity grains (Supplementary material).

2.2. Ferromagnetic mineralogy

Our electron microscopy analyses found that metal grains in 12022 have compositions of $Fe_{1-x}Ni_x$ with $0.05 < x < 0.19$ and no detectable P (<0.03% by mass). A previous study observed a similar compositional range along with an additional population of nearly pure Fe grains (Reid et al., 1970). Metal grains in 15597 have compositions of $Fe_{1-x}Ni_x$ with $0.02 < x < 0.12$ (with 2 out of 11 analyzed grains having $x < 0.03$) and trace P (0.02–0.08% by mass). These compositions, the samples' fast cooling rates (Section 2.3) and the homogeneity of Ni contents and lack of exsolution textures within most metal grains collectively indicate that both kamacite (α-Fe) (grains with $x < 0.05$) and martensite (α_2-Fe) (grains with $x > 0.05$) are the main ferromagnetic minerals in both rocks (Supplementary material). This is supported by our observation that laboratory anhysteretic remanent magnetization (ARM) and isothermal remanent magnetization (IRM) unblock mostly by ~600 °C [close to the austenite-finish temperatures (i.e., martensite recrystallization temperatures) expected for the observed range of Ni abundances] with a small fraction of IRM persisting to higher temperatures (consistent with kamacite's 780 °C Curie temperature) (Supplementary material). The presence of kamacite is also indicated by previous thermomagnetic analyses showing magnetization persisting to 780 °C (Helsley, 1971). Early-formed kamacite should acquire a TRM after cooling below its Curie temperature, while martensite should predominantly acquire a TRM after passing through the martensite-finish temperature (ranging from ~600 to 120 °C and 600 to 350 °C for the observed compositions in 12022 and 15597, respectively; Swartzendruber et al., 1991).

2.3. Cooling rate analyses and implications

Following Grove and Walker (1977), we determined that 12022 cooled below 1050 °C (when plagioclase crystallizes) at a rate of 19 °C h^{-1}. Using the same method, 15597 was determined to have a late-stage cooling rate of 300–500 °C h^{-1} at temperatures of 1050–975 °C when plagioclase crystallizes (Grove and Walker, 1977). This is broadly consistent with the sizes of pyroxene crystals, which indicate a cooling rate of 10–150 °C h^{-1} that reflects both early (1210–1050 °C) and late-stage (1050–975 °C) cooling. Using pyroxene sizes, Lofgren et al. (1979) determined a slower integrated cooling rate of 20–50 °C h^{-1}; differences in the type of sample container used for each study may have led to a difference in crystal nucleation kinetics (Grove and Walker, 1977 conducted Fe-capsule and Fe-loop crystallization experiments, while Lofgren et al., 1979 used Pt-loop crystallization experiments).

Assuming a 1000-s laboratory heating step, the maximum unblocking temperature of a ~40 yr terrestrial VRM would likely be ~125–200 °C (Garrick-Bethell and Weiss, 2010; Supplementary material). Therefore, any primary TRM in samples 12022 and 15597 would be mostly recorded in grains with laboratory unblocking temperatures between the kamacite Curie temperature of 780 °C and 200 °C. Our cooling rate analyses (mentioned above) suggest that 12022 cooled from the kamacite Curie temperature and the peak martensite-finish temperature of ~600 °C (Section 2.2) to 200 °C over a period of 31 and 21 hours, respectively. Conservatively assuming the fastest late-stage cooling rate of 500 °C h^{-1}, 15597 cooled from the kamacite Curie temperature and its peak martensite finish temperature (Section 2.2) to 200 °C over a period of at least 1.2 and 0.8 hours, respectively. While the largest, basin-forming impacts may have produced transient magnetic fields lasting <1 day (Hood and Artemieva, 2008), the smaller impacts post-dating 3.7 Ga (i.e., those actually occurring at the time 12022 and 15597 formed) likely only produced plasma fields lasting ≤1 second (Supplementary material). Therefore, any TRM in these samples is probably a record of a long-lived field like that from a core dynamo or remanent crustal field rather than from transient impact fields.

3. Natural remanent magnetization

Our 12022 subsamples were mutually oriented and collected from three parent blocks sawn in 1970 (splits 310, 308 and 305, which we subdivided into 4, 3, and 3 subsamples, respectively). Our six subsamples of 15597 were also mutually oriented and taken from a single parent chip (split 82). All paleomagnetic and rock magnetic measurements were made using a 2G Enterprises Superconducting Rock Magnetometer 755 which has a sensitivity of 10^{-12} Am^2 (at least two orders of magnitude greater than the magnetic moment of our subsamples) housed at the MIT Paleomagnetism Laboratory. The magnetometer is equipped with automated sample handling and demagnetization equipment (Kirschvink et al., 2008).

3.1. Methods

To prevent sample alteration from heating, we primarily used room-temperature alternating field (AF) demagnetization-based techniques rather than thermal methods for NRM characterization and paleointensity studies. All but three of our subsamples from 12022 and 15597 were subjected to three axis AF demagnetization up to either 85 or 290 mT following Garrick-Bethell et al. (2009), Shea et al. (2012), and Suavet et al. (2013). Their magnetic moments were measured after AF application in each of the three orthogonal directions. To reduce the acquisition of spurious gyroremanent magnetization (GRM) and ARM, we repeated AF applications 5–10 times for each AF level and averaged the measurements following the Zijderveld–Dunlop method (Stephenson, 1993). The remaining three subsamples (12022,305d 12022,310c, and 15597,82f) were thermally demagnetized. To prevent alteration of metal grains at high temperatures, thermal demagnetization was conducted in a controlled oxygen fugacity atmosphere (using a calibrated mixture of CO_2 and H_2 with the concentration of CO_2 increasing from 3% at 50 °C to 21% at 800 °C) (Suavet et al., in press).

NRM components (Table S2) were identified and fit using principal component analysis (PCA) (Kirschvink, 1980). The highest coercivity or highest blocking temperature component from each subsample was subjected to the deviation angle (DANG)/maximum angular deviation (MAD) test (Lawrence et al., 2008) as a qualitative way to determine whether it was origin-trending (and therefore whether it is a candidate for the primary magnetization that formed after primary cooling). The test compares the angular difference between an unconstrained least squares fit of the NRM component and the centroid of the least squares fit (DANG) to the MAD of the fit. A drawback of using the DANG/MAD test is that it does not assign any confidence interval to the hypothesis that a magnetization component is origin-trending.

3.2. Demagnetization results

Depending on the subsample, we identified either two or three magnetization components in 12022: low coercivity (LC) and low blocking temperature (LT) components were blocked up to a maximum of 8 mT or 86 °C, and one or two additional medium coercivity (MC) and medium blocking temperature (MT) components were present at higher AF levels and unblocking temperatures (Supplementary material, Table S2). Within each parent chip, the LC and LT directions were similar, as were the MC and MT directions (Fig. 2), indicating that AF and thermal demagnetization are isolating the same underlying magnetization components. The first MC/MT component (which we refer to as MC1/MT1) was typically blocked from the end of the LC/LT component up to 23–85 mT during AF demagnetization and up to 200–240 °C during thermal demagnetization. A second MC/MT component (which we refer to as MC2/MT2), present in 5 out of 11 subsamples, was blocked from the end of the MC1 component up to ~110 mT and ~325 °C. These results are broadly consistent with previous studies of 12022 (Fuller et al., 1979; Helsley, 1971; Helsley, 1972; Supplementary material). No components were observed for any sample beyond the MC1/MT1 and MC2/MT2 identified above.

All five AF-demagnetized subsamples from 15597 had one LC component blocked up to ~9.5 mT. Two subsamples apparently had no higher coercivity components, while the other three subsamples had one additional poorly-defined MC1 component blocked up to 19 mT (Supplementary material, Table S2). Thermal demagnetization of one subsample revealed an LT component blocked to 110 °C and an MT1 component blocked to 240 °C. The LC, LT, MC1, and MT1 components are collectively non-unidirectional between subsamples (Supplementary material, Fig. S10). The observed instability and low maximum coercivity of the NRM is similar to that previously observed for 15597 (Cournède et al., 2012; Fuller et al., 1979).

3.3. Interpretation of NRM components

The grouping of LC/LT components of 12022 subsamples within each parent block cut in 1970 and the collectively scattered directions among the multiple parent blocks are consistent with their origin as VRM acquired during the 40 years of exposure to the Earth's magnetic field following cutting at JSC. A VRM origin is
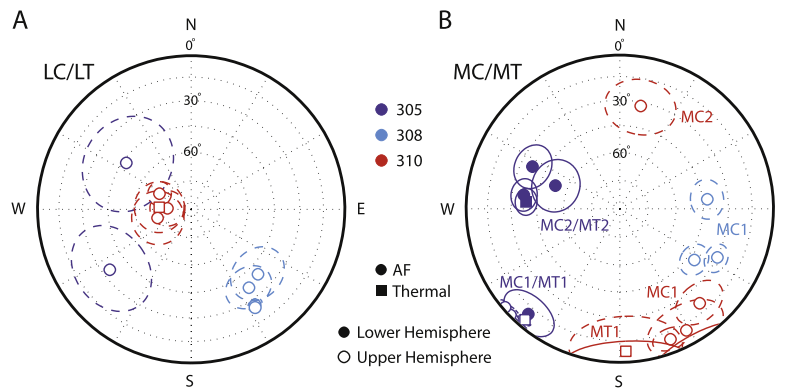
Fig. 2. Magnetization components observed for mutually oriented samples of 12022. Shown is an equal area stereographic projection of component directions, with symbols and surrounding ellipses representing directions and associated maximum angular deviation values obtained from principal component analyses (Supplementary material). (A) LC (circles) and LT (squares) component directions. (B) MC (circles) MT (squares) component directions. Subsamples from parent blocks 305, 308, and 310 are shown in dark blue, light blue, and red circles, respectively. Open symbols (dashed lines) represent directions in the upper hemisphere and filled symbols (solid lines) represent directions in the lower hemisphere. MC1, MC2, MT1, and MT2 components are labeled in (B).
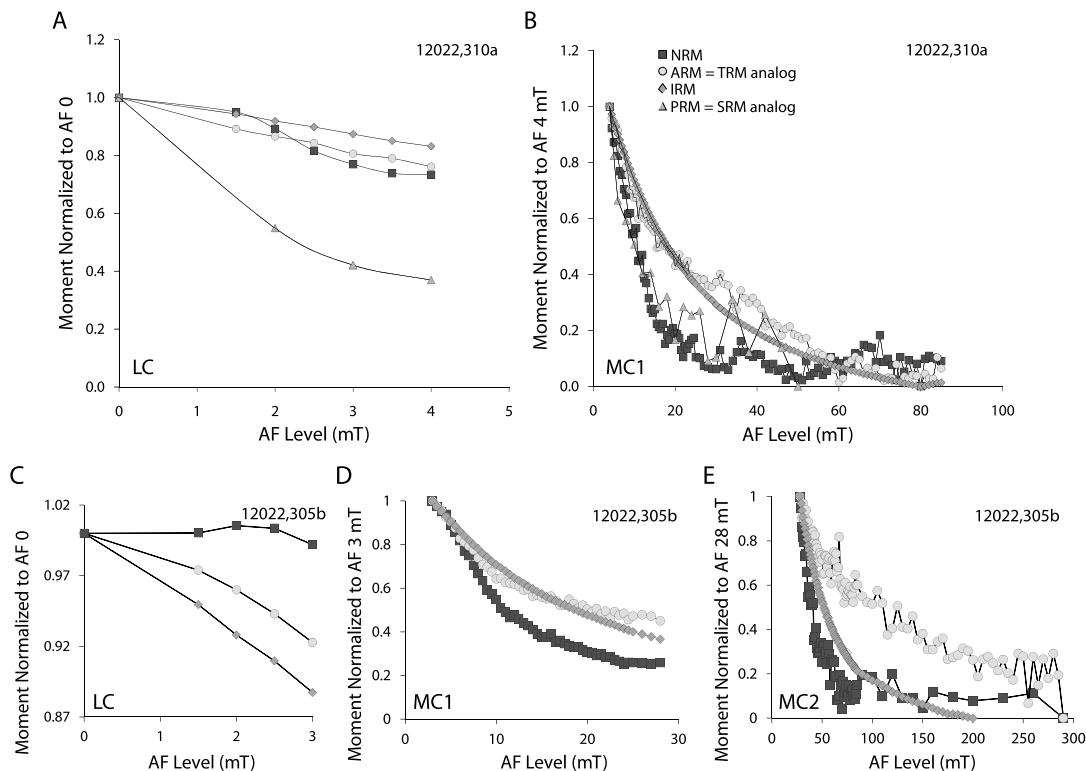

Fig. 3. AF demagnetization of sample 12022,310a and 12022,305b. Shown is the intensity of NRM (squares) during AF demagnetization compared to that of various forms of laboratory-induced magnetization: ARM acquired in an 85 mT AC field and 0.2 mT DC bias field (circles), IRM acquired in a 200 mT field (diamonds), and PRM acquired in a field of 0.75 mT at a pressure of 1.08 GPa (triangles). (A) Sample 12022,310a magnetization normalized to initial (undemagnetized) step to emphasize comparison between LC component and laboratory magnetizations. (B) Sample 12022,310a magnetization normalized to the 4 mT AF step to emphasize comparison between MC1 component and laboratory magnetizations. (C) Sample 12022,305b LC component normalized to initial step. (D) Sample 12022,305b MC1 component normalized to the 3 mT AF step. (E) Sample 12022,305b MC2 component normalized to the 28 mT AF step.

also strongly supported by our laboratory VRM acquisition experiments (Supplementary material), as well as the low (86 °C) peak unblocking temperature and the ∼46 μT (Earth field-strength) average LC/LT component paleointensity (Supplementary material, Table S3).

Comparison of the AF demagnetization of NRM in sample 12022 to that of laboratory ARM (a proxy for TRM) or saturation IRM indicates that both the MC1/MT1 and MC2/MT2 components are inconsistent with being total TRM or IRM (Fig. 3). This is corroborated by our thermal demagnetization experiments on two subsamples, which show that the NRM in each sample is

only blocked to ∼240–325 °C, well below the sample's peak demagnetization temperature (Section 3.2 and Supplementary material). Shock remanent magnetization (SRM) is likely precluded by the non-unidirectionality of these components across the entire sample. Fuller and Cisowski (1987) hypothesized that some lunar rocks may have acquired partial TRM (pTRM) as a result of heating during dry saw cutting at JSC. Our investigation into the cutting history of sample 12022 strongly suggests that the MC2/MT2 in parent block 305 and possibly also the MC1/MT1 components in blocks 308 and 310 were likely acquired by samples as a result of heating during JSC cutting in the ambient laboratory field

(Supplementary material). Regardless of the origin of the MC and MT components, their non-unidirectionality across all three parent blocks as well as the lack of resemblance between demagnetization of NRM and ARM suggest that they cannot be TRM from a dynamo field.

The non-unidirectionality of the LC/LT and MC1/MT1 components in 15597 excludes total TRM and SRM as the source of magnetization. Chemical remanent magnetization (CRM) may be ruled out by the lack of aqueous alteration features. While IRM may be capable of inducing non-unidirectional overprints on the samples due to the curved nature of fields near strongly magnetized objects, the NRM/IRM ratios for the coercivity ranges of these components are below the values (<0.1–1) typically indicative of IRM. The logarithmic time-dependence of VRM acquisition might challenge a VRM origin for both components. However, both our study and previous work have shown that 15597 is extremely susceptible to VRM acquisition (Supplementary material). It is almost certain that the sample was rotated multiple times after return to Earth. Therefore, it is possible that different regions within the sample acquired VRM at different rates, causing non-unidirectional NRM. The low coercivities and peak unblocking temperatures (110 °C and 240 °C) of these components are also consistent with a VRM origin (Supplementary material).

4. Paleointensity constraints

4.1. Introduction

We primarily used the nondestructive, AF-based, ARM and IRM methods to determine paleointensities for the magnetization components present in our samples (Garrick-Bethell et al., 2009; Shea et al., 2012; Suavet et al., 2013; Yu, 2010; Supplementary material). Thermal paleointensity experiments were conducted on one subsample from each parent rock using a pTRM method (Supplementary material). Paleointensities from the ARM (P_{ARM}) and IRM (P_{IRM}) methods were calculated using the following formulas:

$$P_{\mathrm{ARM}} = \frac{\triangle \mathrm{NRM}}{\triangle \mathrm{ARM}} \cdot \frac{b}{f'} \tag{1}$$

$$P_{\mathrm{IRM}} = \frac{\triangle \mathrm{NRM}}{\triangle \mathrm{IRM}} \cdot a \tag{2}$$

where $\triangle$NRM, $\triangle$ARM and $\triangle$IRM are the changes in moment between AF demagnetization steps for NRM, ARM, and IRM, respectively, b is a dc bias field, f' is the TRM/ARM ratio, and a is a calibration constant with units of field that is inversely proportional to the TRM/IRM ratio. Here we adopt values of 1.34 for f' and 3000 μT for a (Gattacceca and Rochette, 2004; Stephenson and Collinson, 1974). Note that values of a similar to the latter have also been measured for martensite-bearing samples (Wasilewski, 1981).

4.2. Paleointensity results

The LC, MC1, and MC2 components of subsamples from 12022 yielded paleointensities ranging from 20 to 144 μT and the LC and MC1 components for 15597 yielded paleointensity values between 6 and 72 μT (Table S3). At AF levels beyond these components, all subsamples from both 12022 and 15597 either yielded paleointensities formally within error of zero or else below the minimum values that can be accurately retrieved using AF methods (see Section 4.3 below and Tables S3 and S4). In summary, our ARM and IRM acquisition experiments indicate that, while magnetic grains capable of carrying remanence with high coercivities are present in these rocks, they carry essentially no NRM (Fig. 4, Fig. S14).
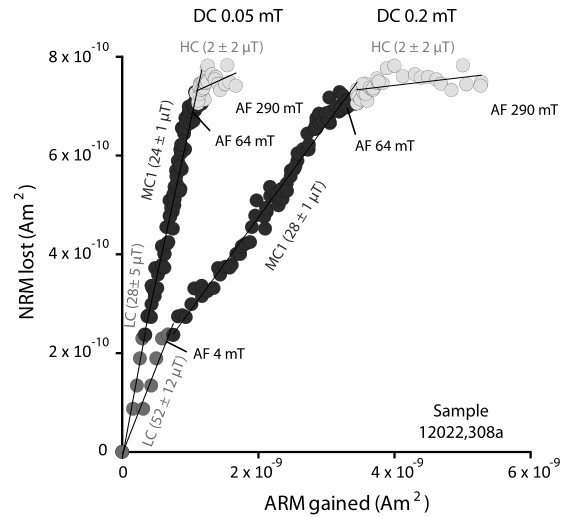

Fig. 4. ARM paleointensity experiments for subsample 12022,308a. Shown is NRM lost during AF demagnetization as a function of ARM gained during stepwise ARM acquisition (AC field increasing to 85 or 290 mT, DC bias field = 0.05 and 0.2 mT) at an equivalent AC field. Points corresponding to the LC and MC1 components in samples are shown with medium gray and dark gray circles respectively. Data from higher AF levels (HC) are shown in light gray.

4.3. Constraining the lunar paleofield at ∼3.2–3.3 Ga

AF methods may introduce undesirable magnetic contamination to samples via acquisition of spurious ARM and GRM (Tikoo et al., 2012). As the demagnetization experiment proceeds, spurious ARM and GRM become increasingly strong until they eventually overwhelm the remaining NRM at high AF levels. This ultimately places a lower limit on the paleointensity that can be recovered from a given sample which depends on its rock magnetic properties (Tikoo et al., 2012). We refer to this as the paleointensity fidelity limit. The question we seek to address here is: what is the maximum possible paleofield consistent with the apparent lack of high coercivity remanence in 12022 and 15597?

4.3.1. Methods

Following Tikoo et al. (2012), we determined paleointensity fidelity limits for 12022 and 15597 as well as our previously studied 3.2–3.3 Ga Apollo 12 and 15 basalts 12017, 15016, and 15556. Multiple subsamples of each rock were given a laboratory ARM (as an analog of thermoremanent NRM) that was then AF demagnetized. The laboratory ARMs were produced using an AC field of 85 mT and DC fields ranging from 3 to 200 μT (corresponding to TRM-equivalent fields from 2 to 150 μT, using the TRM/ARM ratio of 1.34 discussed above). The ARM method was then used to retrieve a paleointensity value from each of these laboratory-induced magnetizations. To ensure that we were only determining paleointensity fidelity limits for grains which could have retained magnetization acquired on the Moon, we only included those AF levels above which any confirmed post-lunar overprints were identified by PCA. For subsample 12022,310b, we only used AF levels beyond the end of the MC1 component while for subsample 15597,82b, we only used AF levels above the end of the LC component. This procedure differs from and is more conservative than that utilized by Tikoo et al. (2012), in which fidelity limits were calculated using the full range of AF levels. A sample was considered to have acceptable magnetic fidelity at fields where either the percentage difference between the retrieved paleointensity and the laboratory field, or the percentage difference between the formal uncertainty (the 95% confidence interval determined using a two-tailed Student's t-test) and the laboratory field, were less than 100% (whichever occurred at a higher laboratory DC field value).
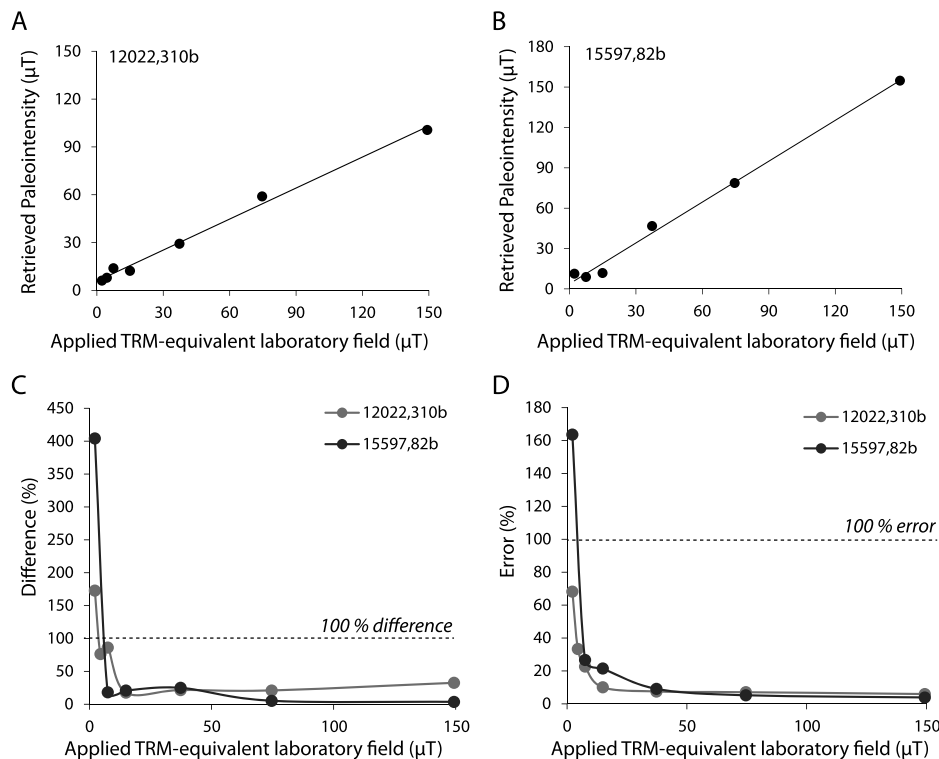
Fig. 5. Paleointensity fidelity limit tests. Recovered paleointensities versus TRM-equivalent applied laboratory field for (A) 12022,310b and (B) 15597,82b. (C) Difference and (D) error for retrieved paleointensities versus applied laboratory field for 12022 (light gray circles) and 15597 (dark gray circles). In (C), the dashed horizontal line denotes the threshold of 100% difference between the applied field and the retrieved paleointensity. In (D), the dashed horizontal line marks the threshold where the width of the 95% confidence interval (e.g., the formal uncertainty) of the retrieved paleointensity value is equal in magnitude to the applied laboratory field.

4.3.2. Paleointensity fidelity limits

We found that best behaved subsamples of 15597 and 12022 had minimum paleointensity fidelity thresholds of ~7 and ~4 µT, respectively (Fig. 5, Table S4), indicating that the lunar surface field was weaker than these values at the times these samples formed. Using our adjusted procedure of disregarding AF levels from LC components, we recalculated the paleointensity fidelity thresholds for the exact same subsamples of 15556 (split 221g), 15016 (split b21), and 12017 (split 12a1c) that we previously reported fidelity limits for in Tikoo et al. (2012). Following this method, 15556, 15016, and 12017 have revised thresholds of ~75, ~37, and ~37 µT, respectively. Therefore, while all five samples give consistent results, the lower paleointensity fidelity thresholds from 12022 and 15597 place a stronger constraint on the maximum possible lunar paleofield at 3.2–3.3 Ga than what may be obtained from the previously studied samples.

4.4. Constraining the decline in lunar paleointensities

Each of the paleointensity limits discussed in Section 4.3 are subject to the typical factor of 3–5 systematic errors associated with the ARM paleointensity method discussed in Section 4.1. It is therefore important to assess whether the decline in mean lunar paleointensities that we observe between 3.56 Ga and 3.19 Ga is statistically significant given these uncertainties. To determine this, we use the Kolmogorov–Smirnov (K–S) statistical test to compare the average lunar paleointensities computed for samples older than 3.5 Ga to the upper paleofield limits inferred above for the younger samples 15597 and 12022 at ~3.3 and ~3.2 Ga, respectively. We exclude the paleofield limits inferred for 15556, 15016, and 12017 because, as described in the preceding section, these samples are low-fidelity paleomagnetic recorders. We use the K–S test to assess the null hypothesis that the pre-3.5 Ga paleointensities and the younger upper paleofield limits from 12022 and 15597 are de-

rived from the same distribution of paleointensity values at the 5% significance value (p).

Average paleointensities reported for pre-3.5 Ga samples 76535, 10020, 10017, and 10049 are 30, 60, 70, and 70 µT, respectively (Garrick-Bethell and Weiss, 2013; Shea et al., 2012; Suavet et al., 2013). As reported in Section 4.3, the paleointensity fidelity limits for 15597 and 12022 are 7 and 4 µT, respectively. By comparing the pre-3.5 Ga paleointensities to the post-3.5 Ga paleointensity limits using the K–S test, we can reject the null hypothesis that both datasets are from the same distribution with a p-value of 0.0469 ($>$95% confidence). However, this calculation does not consider the factor of 3–5 uncertainties associated with each of these paleointensity determinations, which we showed empirically are accurately described by a lognormal distribution (Supplementary material). To address this, we randomly selected sets of six multiplier values (which we call M values) from the probability distribution obtained by fitting a lognormal distribution to the paleointensity data in Fig. S13. These M-values were multiplied by the four pre-3.5 Ga and two post-3.5 Ga paleointensities listed above (which we call I values) to produce a new set of six generated paleointensities (P_L) to use in K–S testing:

$$P_L = MI \tag{3}$$

We then applied the K–S test to each of 1000 sets of six P_L values. Using the K–S test, we could reject the null hypothesis (i.e., $p < 0.05$) that both the pre- and post-3.5 Ga datasets were drawn from the same distribution for 91.5% of these 1000 lognormally generated paleointensity datasets. To incorporate paleointensities and upper limits from other recent studies, we repeated the above procedure while appending the 42, 95, and 111 µT paleointensities obtained for mare basalts 70017, 71505, and 71567, respectively (Cournède et al., 2012), to the above dataset of pre-3.5 Ga paleointensities. We also added the 5 µT upper limit inferred for sample
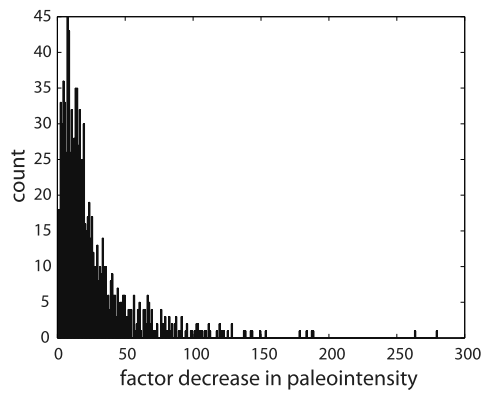
Fig. 6. Histogram showing the decline in paleointensities between 3.56 and 3.19 Ga. The vertical axis gives the number of counts (out of 1000 values) per bin of data. The horizontal axis gives the factor decrease in paleointensities, defined to be the (lognormally generated) pre-3.5 Ga paleointensity value divided by the post-3.5 Ga paleointensity value.

60015 (Section 1) to the post-3.5 Ga dataset (such that ten values were compared instead of six). Again, using the K–S test, we can reject the null hypothesis (i.e., $p < 0.05$) 97.2% of the time (out of 1000 trials). Based on these results, we can confidently infer that the pre-3.5 Ga paleointensities are distinct from the post-3.5 Ga upper limits, and that there was indeed a significant decline in the intensity of surface fields between 3.56 and 3.3 Ga.

4.5. Implications of a paleointensity decline

We now discuss what the paleointensity record can tell us about the decline in power at the lunar core–mantle boundary over time. We used scaling laws to estimate the decline in superadiabatic power between 3.56 Ga and 3.19 Ga (Christensen et al., 2009; Dwyer et al., 2011), although we again note that precession or core crystallization dynamos could operate subadiabatically. We used 1000 pairs of randomly generated P_L-values (using the lognormal distribution method from Section 4.4) for the 70 and 4 μT I values at 3.56 and 3.19 Ga and Eq. (4) of Dwyer et al. (2011) to find the decrease in paleointensities and superadiabatic power between 3.56 and 3.19 Ga. We found that between these times, the intensity of the dynamo field declined by at least a factor of $\sim$18 (mean = factor of $\sim$27; 1 standard deviation = factor of $\sim$29) (Fig. 6). Assuming the scaling law used is applicable to the ancient lunar core dynamo, the decline in paleointensities from 70 to <4 μT suggests a factor of at least $\sim 1 \times 10^4$ drop in superadiabatic power during this period.

5. Thermochronometry

It is possible that any TRM acquired by 15597 and 12022 during primary cooling was affected by subsequent thermal events. The absence of shock features precludes direct shock heating, but low-grade metamorphism or burial in a hot ejecta blanket could have led to temperature excursions. To assess this possibility, we conducted ^{40}Ar/^{39}Ar thermochronometry on one subsample from 12022 (Supplementary material). Sample 15597 was also analyzed but yielded a complex, discordant age spectrum that appears to reflect both diffusive loss of ^{40}Ar and ^{39}Ar recoil. In the absence of reasonable constraints on the crystallization age of 15597, it is not possible to model its thermal history.

We found that 12022 has a ^{40}Ar/^{39}Ar plateau age of 3194 ± 12 (one standard deviation analytical uncertainty; ± 25 Ma when uncertainties in the decay constant and age of the fluence monitor are taken into account), which is indistinguishable from a previous age determination for this rock (Alexander et al., 1972), as well as

the mean crystallization ages of other Apollo 12 ilmenite basalts (see Table 5.8 of Stöffler et al., 2006). Its ^{38}Ar cosmogenic exposure age suggests that the rock was brought to the near-surface 262.7 ± 4.9 million years ago. At that time, the sample was likely incorporated into an ejecta blanket which our thermochronometry calculations suggest is unlikely to have reached peak temperatures in excess of $\sim$100–200 °C. 12022 likely also experienced modest gas loss due to solar heating during its near-surface residence (Supplementary material). Regardless of the sample's precise history, our models indicate that 12022 never experienced temperatures high enough to fully demagnetize or remagnetize the sample. Therefore, 12022 should have retained some primary TRM if it had formed in the presence of a stable field such as that from a core dynamo.

6. Discussion

12022 and 15597 do not retain a record of lunar magnetic fields despite not having been substantially demagnetized since their formation. Their lack of magnetization is not a result of their incapacity to carry a high fidelity magnetization: our paleointensity experiments establish that both samples have significant quantities of grains with coercivities above the maximum AF level to which the NRM is blocked (Section 4.2.1). As a result, our measured paleointensity values for this highest coercivity range are within error of zero. Moreover, we find that our ARM and IRM-based paleointensity techniques are capable of retrieving paleointensities down to fields as small as $\sim$4 and $\sim$7 μT for 12022 and 15597, respectively. Therefore, we conclude that the lunar field was weaker than these values when these rocks formed. This is consistent with the weak (<50 nT) remanent crustal fields at the Apollo 12 and 15 landing sites (Dyal et al., 1974). Our paleointensity constraints from 12022 and 15597 are much more restrictive than our results from other young samples such as 15016 and 12017, which place an upper paleofield limit of 37 μT at $\sim$3.3 and $\sim$3.2 Ga. Overall, our results suggest that lunar surface field intensities decreased dramatically (by at least a factor of $\sim$18) to below $\sim$4 μT and possibly even zero sometime between 3.56 ± 0.04 Ga and 3.19 ± 0.03 Ga (Fig. 7). This sharp decline in paleointensities is statistically significant despite the factor of $\sim$3–5 uncertainty on paleointensities obtained using the ARM and IRM methods (Supplementary material). Furthermore, our evidence for weak to null fields from samples collected from different Apollo landing sites ($\sim$1200 km apart) indicates a global-scale decline in the main dynamo field rather than regional phenomena such as a change in crustal magnetization or local fluctuations in the nondipolar components of the dynamo.

A dynamo powered by thermal convection would be expected to weaken as the Moon cooled. For such a dynamo, our inferred decrease in paleointensity would indicate a ≥ 4 order of magnitude drop in superadiabatic power at the lunar core–mantle boundary and that the rate of core cooling progressed to a point where core thermal gradients were greatly weakened (Supplementary material). This is consistent with some thermal evolution models predicting that a thermal convection dynamo operating in a Moon with water-enriched mantle reservoirs would cease between 3.56 and 3.19 Ga (Evans et al., 2014). Although the latent heat release (Zhang et al., 2013) and chemical buoyancy of sulfur-rich liquids resulting from inner core crystallization (Laneuville et al., 2014; Soderlund et al., 2013) could have driven a lunar dynamo until well past 2 Ga (possibly until the present day), a transition from bottom-up to top-down core crystallization could have caused the dynamo to cease much earlier (Laneuville et al., 2014). If the dynamo was instead powered by precession, a decline in paleointensities would reflect the outward migration of the lunar orbit. Consideration of end-member model parameters may permit a preces-
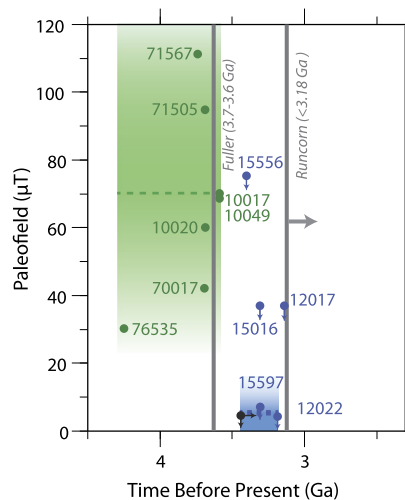
Fig. 7. Paleointensity of the lunar field as a function of time. Each symbol represents a paleointensity measurement from an individual Apollo sample. Paleointensity determinations measured in 2009 and later using the ARM and IRM methods are shown in green (from Garrick-Bethell et al., 2009; Garrick-Bethell and Weiss, 2013; Cournède et al., 2012; Shea et al., 2012; and Suavet et al., 2013). Upper limit on the Thellier–Thellier paleointensity value from Lawrence et al. (2008) is shown in black (note that there is only an upper limit on the age of this constraint), while upper limit ARM paleointensities obtained from the present study are shown in blue. Gray vertical lines denote proposed age for lunar dynamo cessation from Fuller (1998) and upper limit on age of dynamo cessation from Runcorn (1996). Each of our ARM and IRM paleointensity values has an uncertainty of a factor of ∼3 [green and blue gradient boxes surrounding mean pre-3.56 Ga values and post-3.46 Ga upper limit values from 15597 and 12022 (dashed lines), respectively] associated with the unknown ratio of ARM and IRM to TRM. Nevertheless, the sharp decline in paleointensity after 3.56 Ga is statistically significant (see text).

sion dynamo to cease between 3.56 and 3.19 Ga (Supplementary material).

It is currently unclear which of the above mechanisms (or combination thereof) powered the dynamo during the high field period between ∼3.85 and 3.56 Ga. This is because no currently published model for either convective (Evans et al., 2014; Konrad and Spohn, 1997; Laneuville et al., 2013, 2014; Soderlund et al., 2013; Stegman et al., 2003; Zhang et al., 2013) or mechanical (Dwyer et al., 2011; Le Bars et al., 2011) dynamos has been able to produce ∼70 µT lunar surface fields using conventional scaling laws which depend on the superadiabatic power (reviewed by Christensen, 2010). These scalings may incorrectly estimate the lunar paleofield intensity because they are based on simulated dynamos which are far more viscosity-dependent than what is expected for at least the geodynamo (King and Buffett, 2013). In addition, the values of several scaling parameters such as ohmic dissipation, ratio of dipolar to total field, core conductivity, and adiabatic threshold are poorly constrained (Christensen et al., 2009; Gomi et al., 2013; Supplementary material). Furthermore, the conventional (although likely inaccurate) assumption of an initially uniform core surface temperature in dynamo models will lead to underestimated surface fields (Buffett, 2009; Sakuraba and Roberts, 2009). Finally, because these scaling laws do not account for mechanical forcing of core fluid, they may be inapplicable to the precession and impact-driven dynamo mechanisms. Magnetohydrodynamic simulations are required to properly assess the capabilities of mechanical dynamos. In fact, a very recent such simulation suggests that surface fields of up to 100 µT could be generated by a precession dynamo during the high paleointensity epoch before 3.7 Ga (Tian et al., 2014).

Given the current uncertainties in model parameters (Supplementary material) and field scalings, it remains unclear which dynamo generation mechanism(s) is most consistent with the lunar paleomagnetic record. Regardless, the precipitous drop in paleoin-

tensities we infer between 3.56 Ga and 3.19 Ga suggests that at least one of the major dynamo power sources ceased or at least declined dramatically during this period.

7. Conclusions

- Paleomagnetic studies of Apollo samples have demonstrated that the Moon had a core dynamo which generated surface fields of ∼30–100 µT between at least 4.2 and 3.56 Ga.
- The poor magnetic recording properties and complex thermal and deformational histories of the vast majority of lunar rocks have hindered prior efforts to determine when the lunar core dynamo declined and ultimately ceased.
- The absence of high coercivity magnetization in the high magnetic fidelity mare basalts 12022 and 15597 suggests that the lunar core dynamo field declined to <∼4 µT (possibly zero) by ∼3.19 Ga.
- The precipitous (at least factor ∼18) decrease in paleointensities (from ∼70 µT to <4 µT) between 3.56 and 3.19 Ga may be compatible with cessation of a thermal convection, mantle precession, or core crystallization-driven dynamo during this period. However, the incompatibility of the high observed paleointensities prior to 3.56 Ga with the fields predicted for thermal convection dynamos may favor alternative mechanisms such as a mechanical dynamo.

Appendix A. Supplementary material

Supplementary material related to this article can be found online at http://dx.doi.org/10.1016/j.epsl.2014.07.010.

References

Alexander, E.C., Davis, P.K., Reynolds, J.H., 1972. Rare-gas analysis on neutron irradiated Apollo 12 samples. Proc. Lunar Sci. Conf. 2, 1787–1795.

Brett, R., Butler, P., Meyer, C., Reid, A.M., Takeda, H., Williams, R., 1971. Apollo 12 igneous rocks 12004, 12008, 12009 and 12022: a mineralogical and petrological study. Proc. Lunar Sci. Conf. 2, 301–317.

Buffett, B.A., 2009. Geodynamo: a matter of boundaries. Nat. Geosci. 2, 741–742.

Christensen, U.R., 2010. Dynamo scaling laws and applications to the planets. Space Sci. Rev. 152, 565–590.

Christensen, U.R., Holzwarth, V., Rainers, A., 2009. Energy flux determines magnetic field strength of planets and stars. Nature 457, 167–169.

Compston, W., 1972. Strontium isotope geochemistry of Apollo 15 basalts. In: The Apollo 15 Lunar Samples. The Lunar Science Institute, Houston, pp. 348–351.

Cournède, C., Gattacceca, J., Rochette, P., 2012. Magnetic study of large Apollo samples: possible evidence for an ancient centered dipolar field on the Moon. Earth Planet. Sci. Lett. 331–332, 31–42.

Dwyer, C.A., Stevenson, D.J., Nimmo, F., 2011. A long-lived lunar dynamo driven by continuous mechanical stirring. Nature 479, 212–214.

Dyal, P., Parkin, C.W., Daily, W.D., 1974. Magnetism and the interior of the Moon. Rev. Geophys. Space Phys. 12, 568–591.

Evans, A.J., Zuber, M.T., Weiss, B.P., Tikoo, S.M., 2014. A wet, heterogeneous lunar interior: lower mantle & core dynamo evolution. J. Geophys. Res. – Planets 119 (5), 1061–1077.

Fuller, M., 1998. Lunar magnetism – a retrospective view of the Apollo sample magnetic studies. Phys. Chem. Earth 23, 725–735. http://dx.doi.org/10.1016/S0079-1946(98)00083-4.

Fuller, M., Cisowski, S.M., 1987. Lunar paleomagnetism. Geomagnetism 2, 307–455.

Fuller, M., Meshkov, E., Cisowski, S., Hale, C., 1979. On the natural remanent magnetization of certain mare basalts. Proc. Lunar Planet. Sci. Conf. 10, 2211–2233.

Garrick-Bethell, I., Weiss, B.P., 2010. Kamacite blocking temperatures and applications to lunar magnetism. Earth Planet. Sci. Lett. 294, 1–7.

Garrick-Bethell, I., Weiss, B.P., 2013. New lunar magnetic field paleointensity estimate from troctolite 76535. Proc. Lunar Sci. Forum.

Garrick-Bethell, I., Weiss, B.P., Shuster, D.L., Buz, J., 2009. Early lunar magnetism. Science 323, 356–359.

Gattacceca, J., Rochette, P., 2004. Toward a robust normalized magnetic paleointensity method applied to meteorites. Earth Planet. Sci. Lett. 227, 377–393.

Gomi, H., Ohta, K., Hirose, K., Labrosse, S., Caracas, R., Verstraete, M.J., Hernlud, J.W., 2013. The high conductivity of iron and thermal evolution of the Earth's core. Phys. Earth Planet. Inter. 224, 88–103.

Grove, T.L., Walker, D., 1977. Cooling histories of Apollo 15 quartz-normative basalts. Proc. Lunar Planet. Sci. Conf. 8, 1501–1520.

Helsley, C.E., 1971. Evidence for an ancient lunar magnetic field. Proc. Lunar Sci. Conf. 3, 2485–2490.

Helsley, C.E., 1972. The significance of the magnetism observed in lunar rocks. Proc. Conf. Lunar Geophys. 159, 158–160.

Hood, L.L., 2011. Central magnetic anomalies of Nectarian-aged lunar impact basins: probable evidence for an early core dynamo. Icarus 211, 1109–1128.

Hood, L.L., Artemieva, N.A., 2008. Antipodal effects of lunar basin-forming impacts: initial 3D simulations and comparisons with observations. Icarus 193, 485–502.

James, O.B., Wright, T.L., 1972. Apollo 11 and 12 mare basalts and gabbros: classification, compositional variations and possible petrogenetic relations. Geol. Soc. Am. Bull. 83, 2357–2382.

King, E.M., Buffett, B.A., 2013. Flow speeds and length scales in geodynamo models: the role of viscosity. Earth Planet. Sci. Lett. 371–372, 156–162.

Kirschvink, J., 1980. The least-squares line and plane and the analysis of palaeomagnetic data. Geophys. J. R. Astron. Soc. 62, 699–718.

Kirschvink, J., Kopp, R., Raub, T., Baumgartner, C., Holt, J., 2008. Rapid, precise, and high-sensitivity acquisition of paleomagnetic and rock magnetic data: development of a low-noise automatic sample changing system for superconducting rock magnetometers. Geochem. Geophys. Geosyst. 9, 1–18.

Kirsten, T., Horn, P., Kiko, J., 1973. Ar40–Ar39 dating of Apollo 16 and Apollo 15 rocks and rare gas analysis of Apollo 16 soils. Proc. Lunar Sci. Conf. 4, 438–440.

Konrad, W., Spohn, T., 1997. Thermal history of the Moon: implications for an early core dynamo and post-accretional magmatism. Adv. Space Res. 19, 1511–1521.

Laneuville, M., Wieczorek, M.A., Breuer, D., Tosi, N., 2013. Asymmetric thermal evolution of the Moon. J. Geophys. Res. 118, 1435–1452.

Laneuville, M., Wieczorek, M.A., Breuer, D., Aubert, J., Morard, G., Rückriemen, T., 2014. A long-lived lunar dynamo powered by core crystallization. Earth Planet. Sci. Lett. 401, 251–260.

Lawrence, K., Johnson, C., Tauxe, L., Gee, J.S., 2008. Lunar paleointensity measurements: implications for lunar magnetic evolution. Phys. Earth Planet. Inter. 168, 71–87.

Le Bars, M., Wieczorek, M.A., Karatekin, O., Cebron, D., Laneuville, M., 2011. An impact-driven dynamo for the early Moon. Nature 479, 215–218.

Lofgren, G.E., Grove, T.L., Brown, R.W., Smith, D.P., 1979. Comparison of dynamic crystallization techniques on Apollo 15 quartz normative basalts. Proc. Lunar Planet. Sci. 10, 423–438.

McGee, P.E., Warner, J.L., Simonds, C.H., 1977. Introduction to the Apollo Collections. Part I: Lunar Igneous Rocks. Curators Office, NASA Johnson Space Center.

Neal, C.R., Hacker, M.D., Snyder, G.A., Taylor, L.A., Liu, Y.-G., Schmitt, R.A., 1994. Basalt generation at the Apollo 12 site. Part 2: Source heterogeneity, multiple melts, and crustal contamination. Meteoritics 29, 349–361.

Reid, A.M., Meyer, C., Harmon, R.S., Brett, R., 1970. Metal grains in Apollo 12 igneous rocks. Earth Planet. Sci. Lett. 9, 1–5.

Runcorn, S.K., 1996. The formation of the lunar core. Geochim. Cosmochim. Acta 60, 1205–1208.

Ryder, G. (Ed.), 1985. Catalog of Apollo 15 Rocks. NASA Curatorial Branch, Houston.

Sakuraba, A., Roberts, P.H., 2009. Generation of a strong magnetic field using uniform heat flux at the surface of the core. Nat. Geosci. 2, 802–805.

Shea, E.K., Weiss, B.P., Cassata, W.S., Shuster, D.L., Tikoo, S.M., Gattacceca, J., Grove, T.L., Fuller, M.D., 2012. A long-lived lunar core dynamo. Science 335, 453–456.

Soderlund, K.M., Schubert, G., Scheinberg, A.L., 2013. Persistence of the lunar dynamo: the role of compositional convection. In: American Geophysical Union Fall Meeting, #GP41D-1157.

Stegman, D.R., Jellinek, A.M., Zatman, S.A., Baumgardner, J.R., Richards, M.A., 2003. An early lunar dynamo driven by thermochemical mantle convection. Nature 421, 143–146.

Stephenson, A., 1993. Three-axis static alternating field demagnetization of rocks and the identification of natural remanent magnetization, gyroremanent magnetization, and anisotropy. J. Geophys. Res. 98, 373–381.

Stephenson, A., Collinson, D.W., 1974. Lunar magnetic field paleointensities determined by an anhysteretic remanent magnetization method. Earth Planet. Sci. Lett. 23, 220–228.

Stöffler, D., Ryder, G., Ivanov, B.A., Artemieva, N.A., Cintala, M.J., Grieve, R.A.F., 2006. Cratering history and lunar chronology. Rev. Mineral. Geochem. 60, 519–596.

Suavet, C., Weiss, B.P., Cassata, W.S., Shuster, D.L., Gattacceca, J., Chan, L., Garrick-Bethell, I., Head, J.W., Grove, T.L., Fuller, M.D., 2013. Persistence and origin of the lunar core dynamo. Proc. Natl. Acad. Sci. USA 110, 8453–8458.

Suavet, C., Weiss, B.P., Grove, T.L., in press. Controlled-atmosphere thermal demagnetization and paleointensity analyses of extraterrestrial rocks. Geochem. Geophys. Geosyst. http://dx.doi.org/10.1002/2013GC005215.

Swartzendruber, L.J., Itkin, V.P., Alcock, C.B., 1991. The Fe–Ni (iron–nickel) system. J. Phase Equilib. 12, 288–312.

Tian, B.Y., Stanley, S., Tikoo, S., Weiss, B., Wisdom, J., 2014. A precession-driven lunar dynamo model. Geophys. Res. Abstr. 16, EGU2014-8914-2011.

Tikoo, S.M., Weiss, B.P., Buz, J., Lima, E.A., Shea, E.K., Melo, G., Grove, T.L., 2012. Magnetic fidelity of lunar samples and implications for an ancient core dynamo. Earth Planet. Sci. Lett. 337–338, 93–103.

Wasilewski, P., 1981. Magnetization in small iron–nickel spheres. Phys. Earth Planet. Inter. 26, 149–161.

Weber, R.C., Lin, P., Garnero, E.J., Williams, Q., Lognonne, P., 2011. Seismic detection of the lunar core. Science 331, 309–312.

Weigand, P.W., Hollister, L.S., 1973. Basaltic vitrophyre 15597 – an undifferentiated melt sample. Earth Planet. Sci. Lett. 19, 61–74.

Weill, D.F., Grieve, R.A., McCallum, I.S., Bottinga, Y., 1971. Mineralogy–petrology of lunar samples. Microprobe studies of samples 12021 and 12022; viscosity of melts of selected lunar compositions. Proc. Lunar Sci. Conf. 2, 413–430.

Wieczorek, M.A., Jolliff, B.L., Khan, A., Pritchard, M.E., Weiss, B.P., 2006. The constitution and structure of the lunar interior. Rev. Mineral. Geochem. 60, 221–364.

Yu, Y., 2010. Paleointensity determination using anhysteretic remanence and saturation isothermal remanence. Geochem. Geophys. Geosyst. 11, Q02Z12.

Zhang, N., Parmentier, E.M., Liang, Y., 2013. A 3-D numerical study of the thermal evolution of the Moon after cumulate mantle overturn: the importance of rheology and core solidification. J. Geophys. Res. 118, 1789–1804.

Supplementary Material

for

Decline of the Lunar Core Dynamo

Sonia M. Tikoo*, Benjamin P. Weiss, William S. Cassata, David L. Shuster, Jérôme Gattacceca,

Eduardo A. Lima, Clément Suavet, Francis Nimmo, and Michael D. Fuller

*To whom correspondence should be addressed. Email: smtikoo@berkeley.edu

1. Introduction

1.1. Recent measurements of young lunar samples. As discussed in the main text, prior paleomagnetic studies have not been able to conclusively determine when the lunar dynamo field decayed nor when it ultimately ceased. This includes two recent paleomagnetic studies which reached contradicting conclusions about the late dynamo: the first suggested the absence of a lunar core dynamo at 3.34 billion years ago (Ga), while the second purported to have evidence for >10 µT dynamo surface fields at 3.3 Ga. We briefly discuss the contexts of these two studies.

One study analyzed cataclastic anorthosite 60015 (Lawrence et al., 2008). The study failed to identify a stable thermoremanent (TRM) component in 60015 but argued that the sample was capable of recording a 5 µT laboratory TRM (with the caveat that their sample may have experienced some alteration during a prior thermal experiment). This was interpreted as indicating that the lunar field was weaker than 5 µT at the time of the sample's $^{40}Ar/^{39}Ar$ plateau age [3.46 ± 0.05 Ga when adjusting the data of Schaeffer and Husain (1974) using current knowledge of decay constants and fluence monitors (Renne et al., 2010; Renne et al., 2011)]. However, sample 60015 has abundant petrographic evidence of shock including undulatory extinction and localized impact melting (Dixon and Papike, 1975; Sclar et al., 1973; Sclar and Bauer, 1974). In addition, its $^{40}Ar/^{39}Ar$ age spectrum indicates partial loss of radiogenic ^{40}Ar (at release steps below 1600°C) [e.g., Phinney et al. (1975)], suggesting that significant thermal disturbances likely occurred even after the 3.45 Ga plateau age. Furthermore, more than half of the sample is covered with a thick (locally up to 5 mm) layer of young impact glass, which has been variably estimated to have formed 2 million years ago (Ma) (See, 1986) and 1 billion years ago (Sclar and Bauer, 1974). Therefore, it is unclear whether 60015 experienced shock heating in the absence of a lunar core dynamo magnetic field at ~3.45 Ga or whether this sample was thermally and/or shock-demagnetized by later processes [e.g., Bezaeva et al. (2010)]. Therefore, both the age of this sample's paleointensity constraint and the paleointensity upper limit itself (which assumes the sample was not demagnetized) are uncertain. Nevertheless, this study provides the only modern Thellier-Thellier paleointensity constraint on the late lunar magnetic field.

The second recent paleomagnetic study (Cournède et al., 2012) suggested that one 3.3 Ga mare basalt, 12002, may have recorded a lunar dynamo field of several tens of µT. However, as discussed by Suavet et al. (2013), there are several factors which indicate that the natural remanent magnetization (NRM) observed in this study may not be consistent with a TRM acquired in a lunar core dynamo field. During all experiments, the sample was encased in a container whose magnetic moment was approximately the same as the sample, and the NRM was not origin-trending. Furthermore, no mutually oriented subsamples were measured to assess the unidirectionality of NRM within the bulk sample. Lastly, the sample's remanent magnetization derivative (REM') paleointensity varies by nearly a factor of ~10 throughout the demagnetization, suggesting that the paleointensity values given in the study may be unreliable.

In view of the uncertainties associated with the aforementioned studies, we investigated the state of the lunar core dynamo after 3.56 Ga using new paleomagnetic, petrographic, and thermochronological studies of two high magnetic fidelity and pristine young samples (12022 and 15597).

1.2. Allocation of our samples. All subsamples measured in this study were chipped from the
non-space weathered interiors of their parent rocks using a non-magnetic stainless steel chisel at
the Lunar Sample Laboratory at NASA Johnson Space Center (JSC). They were shipped in a
magnetically shielded case (DC shielding factor of ~50) to the Massachusetts Institute of
Technology (MIT) Paleomagnetism Laboratory (http://web.mit.edu/paleomag), where they were
stored and analyzed in a magnetically shielded class ~10,000 clean room. Each subsample was
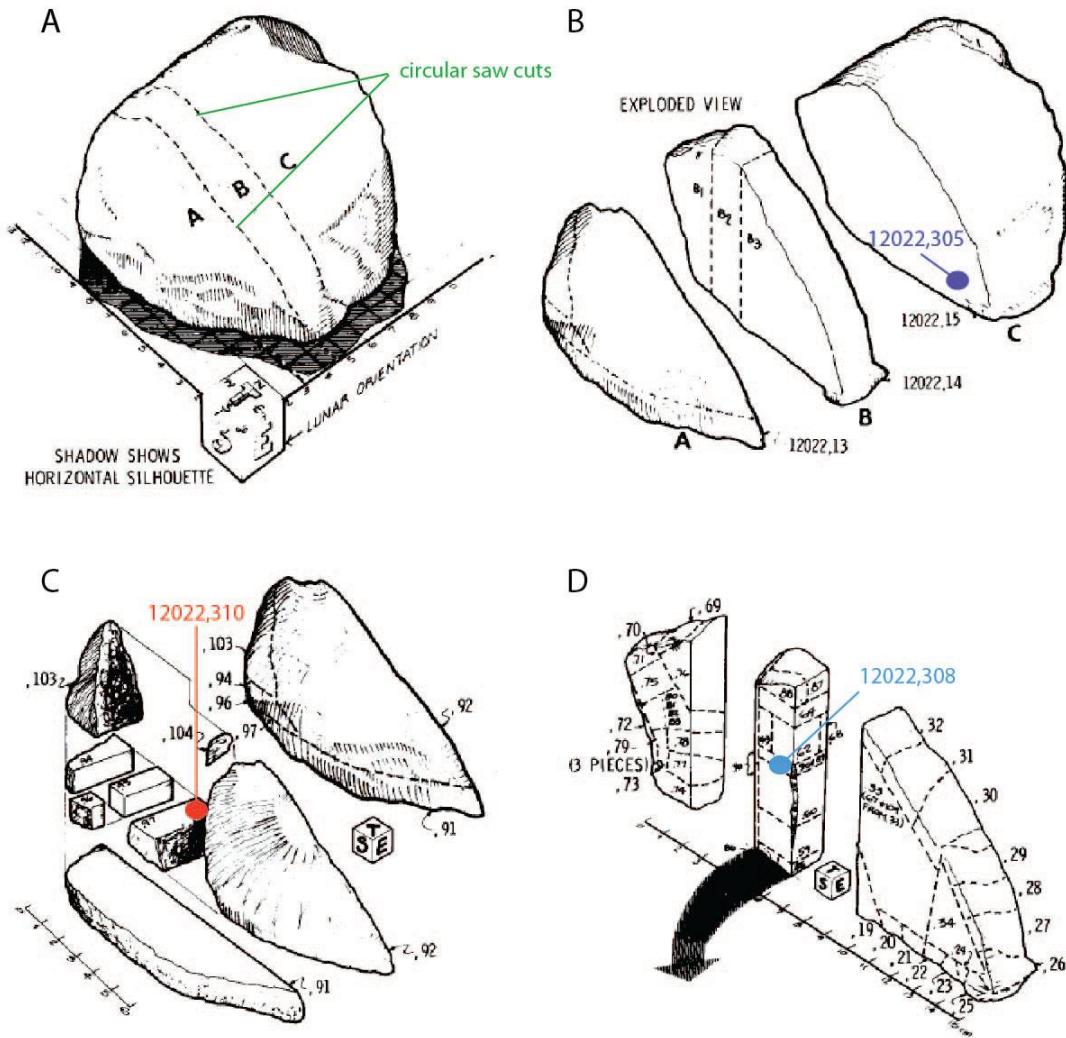
Figure S1. 1970 JSC cutting and sample allocation diagram for sample 12022. (A) Locations of dry
circular saw cut faces, which are associated with subdivision into blocks labeled "A", "B", and "C". (B)
Sampling location for sample 12022,305, which was chipped off the face of block "C". (C) Sampling
location for 12022,310 from block "A". Subdivision of block "A" was conducted with a wire saw. (D)
Sampling location for chip 12022,308 from block "B". Subdivisions from chipping and wire saw cuts are
shown by dashed lines. Note that "lunar orientation" cubes in this figure do correspond to the orientation
system used in our study. The scale bars in (A, C, and D) are in units of cm. JSC sample numbers are
labeled next to each subsample.

76 oriented and glued using non-magnetic cyanoacrylate adhesive onto non-magnetic GE 124
77 quartz mounts. Nearly all subsequent sample handling and experiments were performed in the
78 magnetically shielded room at MIT (ambient magnetic field < 200 nT).
79
80 *1.2.1. Sample 12022.* Sample 12022 was cut into multiple pieces at JSC using a circular tile saw
81 on April 30 and May 1, 1970, 157 days after being returned to Earth. These were then further
82 subdivided using a wire saw at JSC into additional pieces which included the parent samples of
83 our subsamples (12022,15, 12022,90, and 12022,97). These parent samples were then almost
84 certainly stored in different orientations with respect to the geomagnetic field until we were
85 allocated our subsamples. Our subsamples were chipped from these parent samples (305 from
86 15, 308 from 90, and 310 from 97) in December, 2010 at JSC (Fig. S1). After arrival at MIT,
87 subsample 305 was subdivided into four subsamples (305a, 305b, 305c and 305d), subsample
88 308 was subdivided into three subsamples (308a, 308b and 308c) and subsample 310 was
89 subdivided into four subsamples (310a, 310b, 310c and 310e) using a wire saw in our shielded
90 room. All eleven of our 12022 subsamples were mutually oriented using the 1970 cutting
91 diagram (Fig. S1) and photographic documentation of subsequent subsampling. All
92 paleomagnetic measurements were made using the same orientation system as shown in the JSC
93 cutting diagram.
94
95 *1.2.2. Sample 15597.* Subsample 82 was chipped from its parent rock, 15597,0, in 2010 at JSC.
96 The 15597,0 main mass has never been cut with a circular saw or band saw. At MIT, subsample
97 82 was further subdivided into six subsamples (82a, 82b, 82c, 82d, 82e and 82f). All subsamples
98 were mutually oriented with respect to each other. For our paleomagnetic analyses, we
99 established our own orientation system different from the JSC system.
100
101
102 **2. Samples**
103
104 *2.1. Geologic context and sample descriptions.*
105
106 *2.1.1 Sample 12022.* Petrographic features of ilmenite basalt 12022 are described in the main
107 text. 12022 was hammered out of the southeastern side of a mound of regolith located north-
108 northeast of Head Crater and approximately 120 m northwest of the Apollo 12 landing module.
109 The mound was likely excavated and transported to its present location by an impact event
110 (Shoemaker et al., 1970). Sample 12008 [which has a cosmic ray exposure (CRE) age of ~50
111 Ma (Stettler et al., 1973)] was also collected from the mound. Sample 12021 [which has a CRE
112 age ~303 Ma (Marti and Lugmair, 1971)] was collected a few meters away from the mound and
113 is thought to be part of a debris apron originating from the mound. The CRE age of 12022 has
114 previously been determined to range between ~120-220 Ma (Bogard et al., 1971), somewhat
115 younger than our measured Ar CRE age of ~263 Ma (Section 7). These ages suggest that 12022
116 may have been initially excavated from Surveyor Crater (Wanke et al., 1971), prior to a
117 secondary impact event which incorporated it into the mound. Given its 1.2 m height, the mound
118 in its present form cannot be older than the CRE ages of its constituent materials. Therefore, we
119 tentatively assign an upper limit of ~50 Ma (the CRE age of 12008) for the age of the mound.
120 The proximity of the mound to Head Crater motivated the initial hypothesis that the mound
121 originated from within Head Crater. However, the CRE ages of most rocks in the vicinity of

122 Head Crater, which should represent the age of the impact event, are much older (~130-145 Ma)
123 than the mound (Wanke et al., 1971). Therefore, it is unlikely that the Head Crater impact event
124 created the mound. Among the other craters dated by CRE age studies, the most likely origins
125 for the mound formation at or after ~50 Ma are Block Crater [~65 Ma (Wanke et al., 1971)] and
126 Bench Crater [~50-99 Ma (Arvidson et al., 1975; Wanke et al., 1971)]. Several other craters near
127 the Apollo 12 landing site were not sampled by the astronauts, so their ages or relationship to the
128 mound cannot be established.

130 *2.1.2. Sample 15597.* Petrographic features of quartz-normative basalt 15597 are described in
131 the main text. 15597 was collected from soil near the edge of Hadley Rille (Swann et al., 1972).
132 Its source lava, along with that of other Apollo 15 quartz-normative basalts, likely originated
133 from Hadley Rille (Spudis et al., 1988). The sample has a CRE age of 210 Ma, suggesting that it
134 was probably excavated by impact at that time (Kirsten et al., 1973). The vitrophyric, fast-
135 cooled texture of this sample indicates that it formed <10 cm away from a conductive cooling
136 boundary (Grove and Walker, 1977).

138 *2.1.3. Cooling rate implications for impact-generated magnetic fields.* As discussed in the main
139 text, transient impact plasma-generated fields have been proposed as an alternative source of
140 lunar magnetism. Therefore, to address whether TRM in a lunar sample could be from a core
141 dynamo magnetic field, it is important to first rule out impact plasma-generated fields as a
142 potential magnetizing source. Impact-generated fields from the largest, basin-forming impacts
143 are estimated to last < 1 day (Hood and Artemieva, 2008). These can be excluded for 12022 and
144 15597, which formed during the Late Imbrian and Eratosthenian periods and which postdate the
145 last large basin-forming impact, Orientale (Stöffler et al., 2006).
146   The smaller craters that formed after this time would have produced even shorter duration
147 fields. Cumulative crater frequency curves (Stöffler et al., 2006) indicate that a 1 km crater
148 formed on the Moon on average once every 1000 years during the Late Imbrian era. The chance
149 of such crater forming near our basalts during their primary cooling period is essentially
150 negligible. As we show next, fields produced by even a 1 km diameter crater-forming event are
151 estimated to be too short-lived to magnetize our rocks. Using equation 5.4 of Stöffler et al.
152 (2006), and assuming a transient crater diameter of 1 km, impactor velocity of 17 km s^{-1},
153 impactor and target densities of 3000 kg m^{-3}, and a lunar gravitational acceleration of 1.6 m s^{-2},
154 we calculate an impactor diameter of 27 m for typical impacts after 3.7 Ga. Using the
155 relationship $\tau \sim$ [20×(distance from impact)/(impactor velocity)] (where τ is the impact field
156 duration) from Crawford and Schultz (1999), and assuming a 17 km s^{-1} impact velocity, we
157 estimate impact field durations of 0.11-1.1 s for locations ranging between 0.1-1 km away from
158 the impact site. The cooling timescales for both 12022 and 15597 (both samples took at least ~1
159 h to cool from the Curie temperature of kamacite or their martensite finish temperatures to
160 200°C; see main text) are much greater than the duration of impact-generated fields. Therefore,
161 both samples are extremely unlikely to record TRM from an impact-generated field.

163 *2.1.4. Other samples.* In this study, we describe paleointensity experiments on three other lunar
164 samples previously analyzed by Tikoo et al. (2012) (see Section 4.3 of main text). Here we
165 briefly describe the petrologic properties of these samples. Sample 15556 is a fine-grained,
166 vesicular, olivine-normative basalt (McGee et al., 1977; Rhodes and Hubbard, 1973) with a K-Ar
167 age of ~3.4 ± 0.1 Ga (Kirsten et al., 1972). Sample 15016 is a medium-grained, vesicular,

168 olivine-normative basalt (McGee et al., 1977; Papike et al., 1976) with a Rb-Sr age of 3.29 ±
169 0.05 Ga (Evensen et al., 1973) and a K-Ar age of 3.38 ± 0.08 Ga (Kirsten et al., 1973). Sample
170 12017 is a medium-grained pigeonite basalt (James and Wright, 1972; Neal et al., 1994) with a
171 $^{40}Ar/^{39}Ar$ plateau age of 3.19 ± 0.07 Ga (Horn et al., 1975). Compositional analyses (Tikoo et
172 al., 2012) show that all of these samples have < 5 µm diameter blebs of kamacite with very low
173 (< 1%) Ni content in association with troilite, as well 2-30 µm diameter free grains of FeNi metal
174 with Ni abundances varying from < 1% Ni (kamacite) for 12017 up to 7-13% Ni for FeNi grains
175 in 15016.   Using the plagioclase width technique, Tikoo et al. (2012) determined late stage
176 (<1050°C) cooling rates ranging between 0.3-0.6°C hr^{-1} for 15556, 15016, and 12017, suggesting
177 that cooling from the kamacite Curie temperature to 0°C would have taken months. The cooling
178 timescales of these samples are much greater than the duration of impact-generated fields (see
179 Section 2.1.3). None of these samples show any petrographic evidence of shock (peak pressures
180 < 5 GPa).

182 *2.2. Ferromagnetic minerals*

184 *2.2.1. Methods.*   We used reflected light (RL) optical microscopy, backscattered scanning
185 electron microscopy (BSEM), electron dispersive spectroscopy (EDS) and wavelength dispersive
186 spectroscopy (WDS) to assess the mineralogical and elemental composition of the metallic
187 magnetization carriers in our samples (Table S1). Electron microscopy was conducted in the
188 MIT Electron Microprobe Facility using a JEOL-JXA-8200 electron microprobe.   WDS
189 measurements were acquired for Fe, Ni, Al, Si, W, Ti, Cr, Co, P, and S using a beam diameter of
190 1 µm and a counting time of 40 s.
191   We conducted compositional analyses on two samples of 12022 (thin section 114 and
192 polished thick section 308c) and two samples of 15597 (thin section 13 and thick section 82e).
193 Prior to analysis, the thick sections were etched with a solution of 2% nitric acid in ethanol
194 (nital) for 15 s to reveal any textures produced by variations in Ni content and mineralogy in
195 metal grains.

197 *2.2.2. Sample 12022.* We observed FeNi blebs 5-30 µm in diameter present in association with
198 chromite or troilite (Fig. S2a). We used WDS to measure a combination of single-point-per-
199 grain analyses as well as transects across selected grains. We observed metal compositions
200 ranging between $Fe_{0.79-0.93}Ni_{0.05-0.19}$, alloyed with trace (≤2 % by mass) of Co, Ti, and Cr (grains
201 #2, 4-6 in Table S1).   Two previous studies also identified a population of essentially pure Fe
202 associated with troilite (Brett et al., 1971; Reid et al., 1970). Our WDS transects measured
203 across five grains observed two textural populations of metal grains. The first population (3 out
204 of 5 grains, labeled #8, 9, and 11 in Table S1 and Fig. S3) had homogeneous Ni contents (<2%
205 variations across each grain). The second population (2 out of 5 grains, labeled #7 and 10 in
206 Table S1) showed intra-grain heterogeneities in Ni content of up to 10%.
207   Nital-etching of the homogeneous grains (#9 and 11) revealed no evidence of exsolution
208 of kamacite or any other prominent vertical relief (Fig. S3c, e). Martensite is expected to form in
209 low-P quickly-cooled samples [≤5°C minute^{-1} (Kaufman and Cohen, 1956)], but it has also been
210 created in experiments with cooling rates as slow as ~6°C day^{-1} (Wood, 1964). Our measured
211 metal compositions, the absence of exsolution textures, the absence of P, and the fast cooling rate
212 of this sample suggest that these homogeneous grains are martensite [compare with Reisener and
213 Goldstein (2003)].
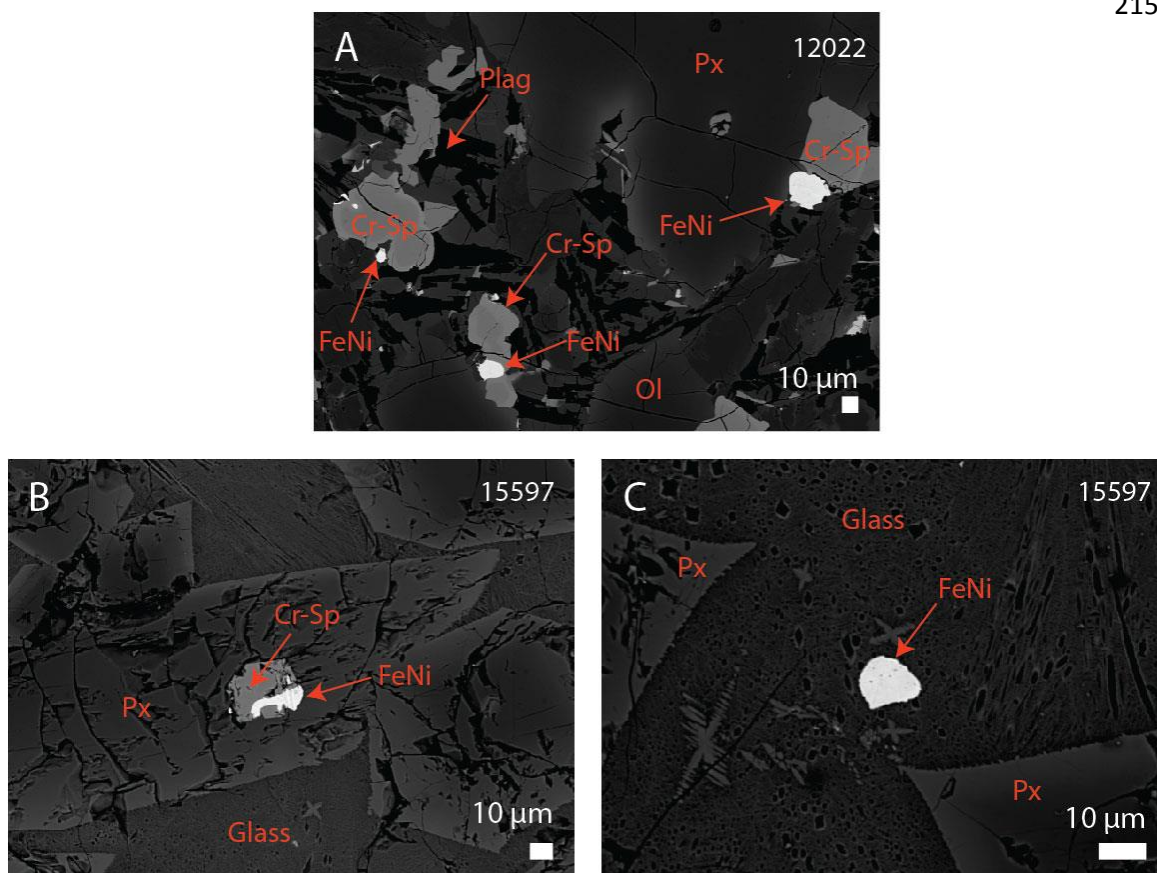
Figure S2. BSEM images of unetched metal grains in 30 μm thin sections. (A) Metal in assemblages with chromite in 12022,114. (B) Metal assembled with chromite inclusions in clinopyroxene in 15597,13. (C) Isolated metal in the glass of 15597,13.

216   Nital-etching revealed that the heterogeneous grain #10 (Fig. S3d) consists of flat, low-
217   lying regions with Ni contents of 7-8% with isolated <1.5 μm-long ridges (at the resolution of
218   our microprobe) with Ni contents of 12-18%. This texture suggests a small amount of Ni
219   migration in this grain and possible incipient kamacite formation during primary cooling of the
220   sample. We attribute the apparent absence of complementary low-Ni regions to the limited
221   resolution of our measurements (~1 μm). The formation of a small amount of kamacite at
222   taenite-taenite grain boundaries surrounded by predominantly martensite is consistent with the 3-
223   4°C day^{-1} cooling experiments of Reisener and Goldstein (2003). It is also conceivable that this
224   kamacite is the product of plessitic decomposition of martensite during a later reheating event.
225   However, we do not favor this because while martensite may decompose to plessite upon
226   extended exposure to high temperatures (e.g., 7-61 days at >600°C) (Romig and Goldstein, 1981;
227   Wood, 1964), such heating events are excluded by our thermochronology results (Section 7).
228   Regardless of whether and how kamacite exsolved in this grain, the majority of the other grains
229   appear to be primary homogenous grains of either martensite or kamacite. Preliminary

experiments (Wasilewski, 1981) indicate that martensite with these compositions formed during cooling in the geomagnetic field has NRM ranging from 2-10 times the TRM acquired by pure Fe (although this study did not control for grain size which has a large influence on TRM intensity).

In summary, our microscopy data indicate that both martensite and kamacite likely contribute to the NRM of 12022. Because of the relatively narrow temperature interval (<100°C) over which martensite forms (i.e., the difference between the martensite-start and -finish temperatures) for these bulk compositions (*31*), the martensite would have acquired mostly a TRM as it cooled with only a small contribution from thermochemical remanent magnetization (TCRM).
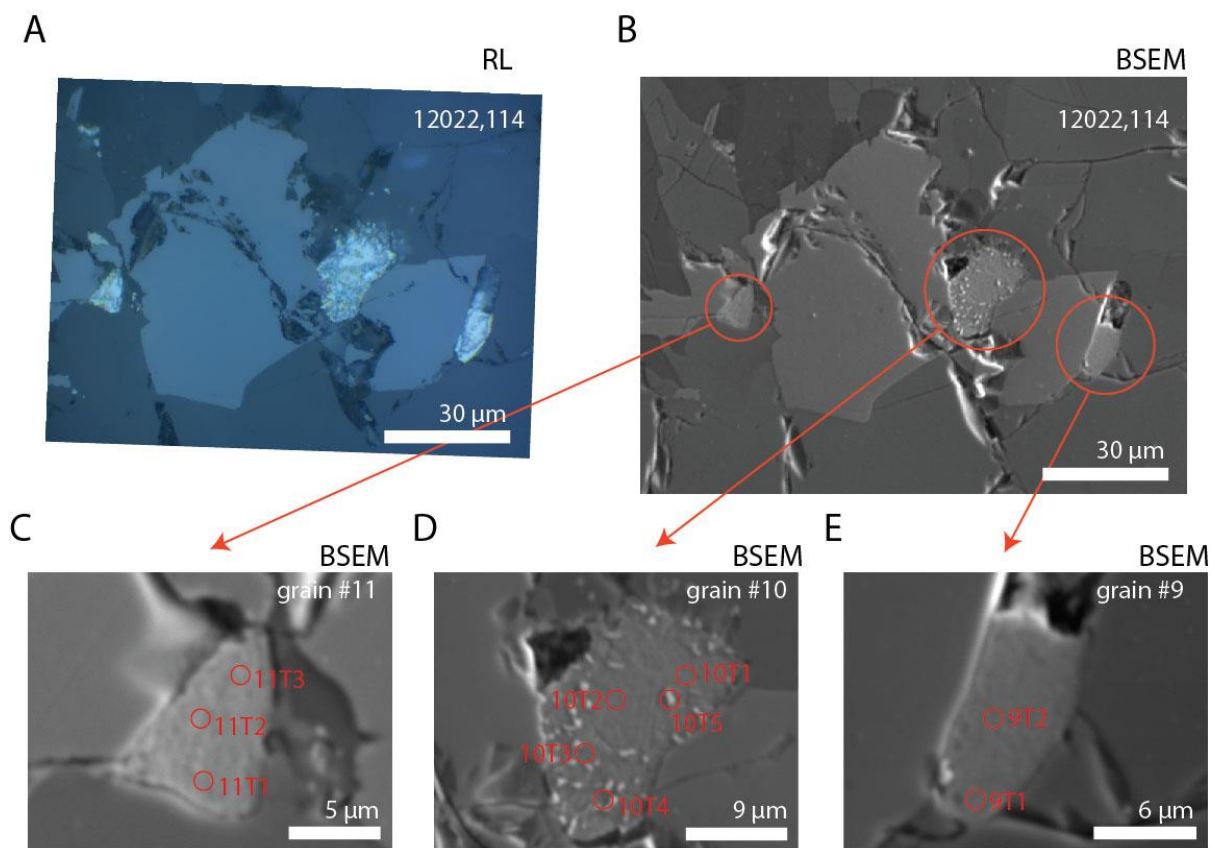
Figure S3. Images of nital-etched metal grains in thick section 12022,308c. (A) RL image of a set of three FeNi grains assembled with chromite. (B) SE image of the same region as Part A. (C) Magnified SE image of the left-most grain, which is likely martensite. (D) Magnified SE image showing topography in the central grain indicating of localized Ni (taenite) enrichment in the martensite. (E) Magnified SE image of the right-most martensite grain. Red circles in (C-E) indicate locations measured with the MIT microprobe (Table S1).

2.2.3. Sample 15597. We observed FeNi grains as irregularly shaped ~5-20 μm isolated inclusions in pyroxene ($Fe_{0.93-0.94}Ni_{0.06-0.07}$), as associations with chromite included in pyroxenes ($Fe_{0.97}Ni_{0.02}$) (Fig. S2b), or as ~10 μm grains ($Fe_{0.83-0.91}Ni_{0.07-0.12}$) in the mesostasis glass (Fig. S2c). These compositions and occurrences are consistent with a previous study of 15597 (Weigand and Hollister, 1973). Intra-grain variations in Ni content measured from transects

246 were limited to ≤2% (Table S1) and nital-etching revealed no evidence of exsolution or other
247 pronounced vertical relief in grains (Fig. S4). The homogeneity of Ni content within grains, the
248 fast ~5°C minute^{-1} cooling rate of the sample (Kaufman and Cohen, 1956), and the absence of
249 exsolution textures in this sample indicate that the main ferromagnetic phase is martensite,
250 although the presence of two (out of eleven) grains with <3% Ni (grains #15 and 19 in Table S1)
251 indicates that kamacite is also present. Like for 12022, the paleomagnetism of 15597 should be
252 carried by both martensite and kamacite and this remanence should be dominantly a TRM if
253 acquired during primary cooling.
254
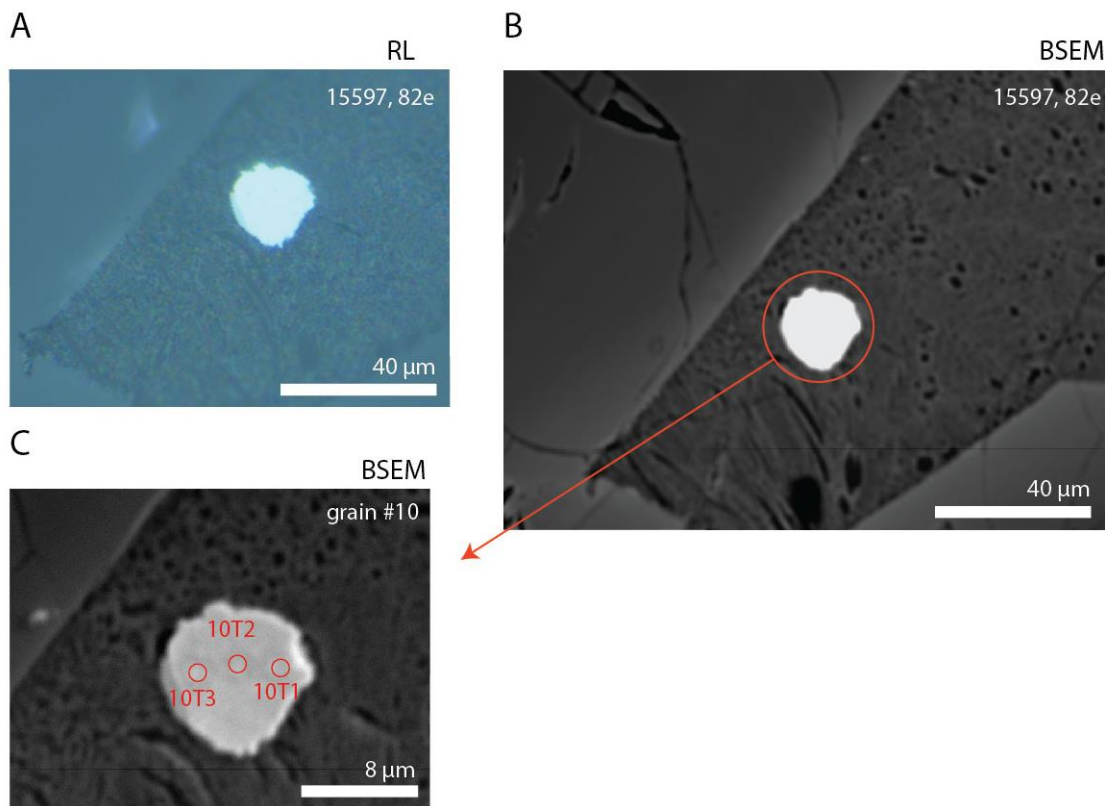
Figure S4. Images of a homogeneous nital-etched metal grain in thick section 15597,82e. (A) RL image. (B) BSEM image. (C) BSEM image with red circles indicate locations measured with the MIT microprobe (Table S1).

255 **3. Natural remanent magnetization (NRM)**
256
257 *3.1. Previous NRM studies of 12022 and 15597.*   A previous alternating field (AF)
258 demagnetization study of two subsamples from parent sample 12022,52 (Fuller et al., 1979)
259 revealed two magnetization components: a low coercivity (LC) component removed by 10 mT,
260 and a second medium coercivity (MC) component which persisted to at least 30 mT (the
261 maximum AF field applied). The MC component directions of the two subsamples were ~20°
262 apart from each other, indicating a roughly unidirectional magnetization within the parent

263 sample. Thermal demagnetization from the same study showed that the NRM of the sample was
264 not significantly affected by heating to 100°C and that its magnetization was reduced
265 approximately in half by heating to 350°C (the maximum heating step applied). No information
266 regarding the nature of magnetic components or magnetization directions from the thermal
267 analysis was reported. A study of another subsample of 12022 observed a dominant component
268 of magnetization blocked below 300°C with an associated paleointensity of 4.8 µT (Helsley,
269 1971). Further heating to 350°C suggested that a separate, higher temperature component may
270 have been present above 300°C, but no paleointensity determinations or heating steps above
271 350°C were conducted. Therefore, it cannot be ruled out that the reported 4.8 µT paleointensity
272 might reflect a secondary magnetization event unrelated to a lunar core dynamo. A later study
273 claimed that Thellier-Thellier (1959) paleointensity results for this sample may be unreliable due
274 to magnetostatic interaction effects (Chowdhary et al., 1987). Another study obtained a residual
275 REM (after demagnetization to 10 mT) paleointensity of ~110 µT for 12022 (Cisowski et al.,
276 1977), contrasting strongly with the thermal paleointensity. However, the same group
277 subsequently reported a residual REM (after demagnetization to 20 mT) paleointensity of ~6 µT
278 (Cisowski et al., 1983) (calculated assuming a calibration constant $a = 3000$; see Section 4.1.2).
279   We are aware of five prior paleomagnetic studies conducted on sample 15597. The first
280 study AF demagnetized two non-mutually oriented subsamples up to 30 mT. By 20 mT,
281 magnetization directions within each subsample after repeat AF applications at the same level
282 were ~20° apart, suggesting poor directional stability at higher AF levels (Fuller et al., 1979). A
283 more recent study could not identify any stable magnetization component in this sample
284 (Cournède et al., 2012). Another two studies attempted to obtain a Thellier-Thellier
285 paleointensity estimate for this sample but the experiment failed, possibly due to interaction
286 effects (Chowdhary et al., 1985, 1987). A residual REM (after demagnetization to 10 mT) study
287 obtained a paleointensity of ~300 µT for 15597 (Cisowski et al., 1977), but the same group later
288 reported a residual REM (after demagnetization to 20 mT) of just 8 µT (Cisowski et al., 1983)
289 (again calculated assuming a calibration constant $a = 3000$).
290   In view of the contradictions and caveats associated with the aforementioned studies, no
291 consensus has yet been reached regarding the origin of NRM in 12022 and 15597. This is
292 despite the fact that previous rock magnetic studies indicate that these samples are among those
293 capable of providing the highest fidelity paleointensity estimates, assuming that they formed in
294 the presence of a magnetic field (Section 5.1). While previous studies were in some cases able to
295 identify magnetization components in these rocks, the number of magnetic components present,
296 the demagnetization stability of these components, and their magnetizing source remain poorly
297 understood. Our goal is to clarify the magnetic history of these samples to assess the extent of
298 decline in lunar surface fields over time.
299
300 *3.2. Our methods.* As justified in our previous magnetic studies of lunar rocks (Garrick-Bethell et
301 al., 2009; Shea et al., 2012; Suavet et al., 2013), we have chosen to mainly use AF
302 demagnetization to analyze our samples due to its nondestructive nature and ability to remove
303 nonthermal overprints from shock and strong artificial magnetic fields. In addition, we
304 conducted thermal demagnetization experiments on two subsamples of 12022 and one subsample
305 of 15597 to investigate whether the NRM in these samples could be attributed to thermally
306 activated mechanisms such as viscous remanent magnetization (VRM), TRM, or partial
307 thermoremanent magnetization (pTRM).
308

10

3.3. Sample 12022. Most subsamples from 12022 contain a LC component and either one or two medium coercivity components (which we label MC1 and MC2) (Fig. S5a,b and Table S2). Thermal demagnetization experiments on two subsamples revealed low temperature (LT) and possibly one (MT1) (Fig. S6a) or two (MT1 and MT2) additional medium temperature components. The components isolated by AF and thermal demagnetization from a single parent chip had essentially indistinguishable directions [e.g., the LC and LT directions were similar to one another (i.e., had overlapping MAD ellipses), as were the MC1 and MT1, and MC2 and MT2 directions].   However, the LC/LT, MC1/MT1, and MC2/MT2 components were non-unidirectional when compared between parent blocks (see Fig. 2 in main text).

3.3.1. Demagnetization of subsample 12022,310a. This subsample had a LC overprint that was removed by 4 mT and an MC1 component blocked up to 35 mT that was origin-trending according to the DANG/MAD test. The sample appeared to stop demagnetizing (its moment magnitude and direction remained steady) between 35 and 85 mT (the highest AF field applied to this subsample). Because of this behavior, we define the MC1 component to span 4-85 mT for this subsample but fit paleointensity values only up to 35 mT.

3.3.2. Demagnetization of subsample 12022,310b. This subsample had a LC component that was removed by 8 mT, followed by an origin-trending (as indicated by the DANG/MAD test), stable MC1 component up to 23.5 mT, at which point the sample was completely demagnetized (the direction became highly unstable).

3.3.3. Demagnetization of subsample 12022,310e. The LC component of this subsample was removed by 8 mT, after which an MC1 component persisted up to 50 mT. Unlike the MC1 components of the other subsamples from block 310, the MC1 component of 310e formally failed the DANG/MAD test. However, the MC1 component direction in this subsample has essentially the same direction as the MC1 components for 310a and 310b, suggesting that it reflects the same magnetization component as identified in those subsamples. We therefore suggest that the MC1 component in 310e is the highest coercivity component in this sample and that spurious ARM acquisition deflected the NRM vector away from the origin during demagnetization.

   To test this proposal further, we computed a PCA fit to the AF data of 310e above 50 mT to attempt to identify a hypothetical MC2 component. We obtained an unconstrained MAD value of 35.7°, which is close to the MAD value ~44° that we computed for a synthetic, computer-generated, random distribution of 1,000 magnetization directions.   This provides additional support of identification of the MC1 component as the highest coercivity component. A third piece of evidence for this is our paleointensity experiments demonstrate the lack of substantial NRM blocked above 50 mT (see Section 4 of main text).

3.3.4. Demagnetization of subsample 12022,310c. Thermal demagnetization (conducted without any prior AF cleaning) revealed two components. The LT component was removed by ~86°C, while a second, non-origin-trending component (MT1) was removed by 240°C. A weak magnetization may exist above this temperature but it is obscured by anomalous demagnetization effects.

3.3.5. Demagnetization of subsample 12022,308a. This subsample had a LC component that was removed by 4 mT, and an origin-trending MC1 component which ranged from 4 mT until the sample was completely demagnetized at 64 mT.

3.3.6. Demagnetization of subsample 12022,308b. This subsample had a LC component that was blocked from NRM up to 8 mT, and an origin-trending MC1 component ranging from 8 mT up until the sample was fully demagnetized at 85 mT.

3.3.7. Demagnetization of subsample 12022,308c. This subsample had an LC component blocked between the NRM and 5 mT, as well as an origin-trending MC1 component blocked from the end of the LC component to 41 mT.

3.3.8. Demagnetization of subsample 12022,305a. The LC component of this subsample was removed by 4.5 mT. There were two MC components present in this sample. The MC1 component ranged from 4.5 to 25 mT, while an origin-trending MC2 component was blocked from 25 to 60 mT. The subsample was completely demagnetized at 60 mT.

3.3.9. Demagnetization of subsample 12022,305b. A LC component was blocked in this subsample between NRM and 3 mT. There were two MC components present in this sample. The MC1 component ranged from 3 to 28 mT, while the MC2 component was blocked from 28 to 78 mT. The subsample was fully demagnetized at 78 mT.

3.3.10. Demagnetization of subsample 12022,305c. This subsample lacked any obvious LC components. However, it did have two MC components: the first was blocked up to 22.5 mT (MC1), while the second, origin-trending component (MC2) spanned 22.5 to 65 mT.

3.3.11. Demagnetization of subsample 12022,305d. AF demagnetization pre-treatment to 8 mT did not remove any magnetization component. Subsequent thermal demagnetization revealed two MT components. The first (MT1) was removed by ~200°C, while the second, origin-trending component (MT2) was fully demagnetized by 325°C.

386
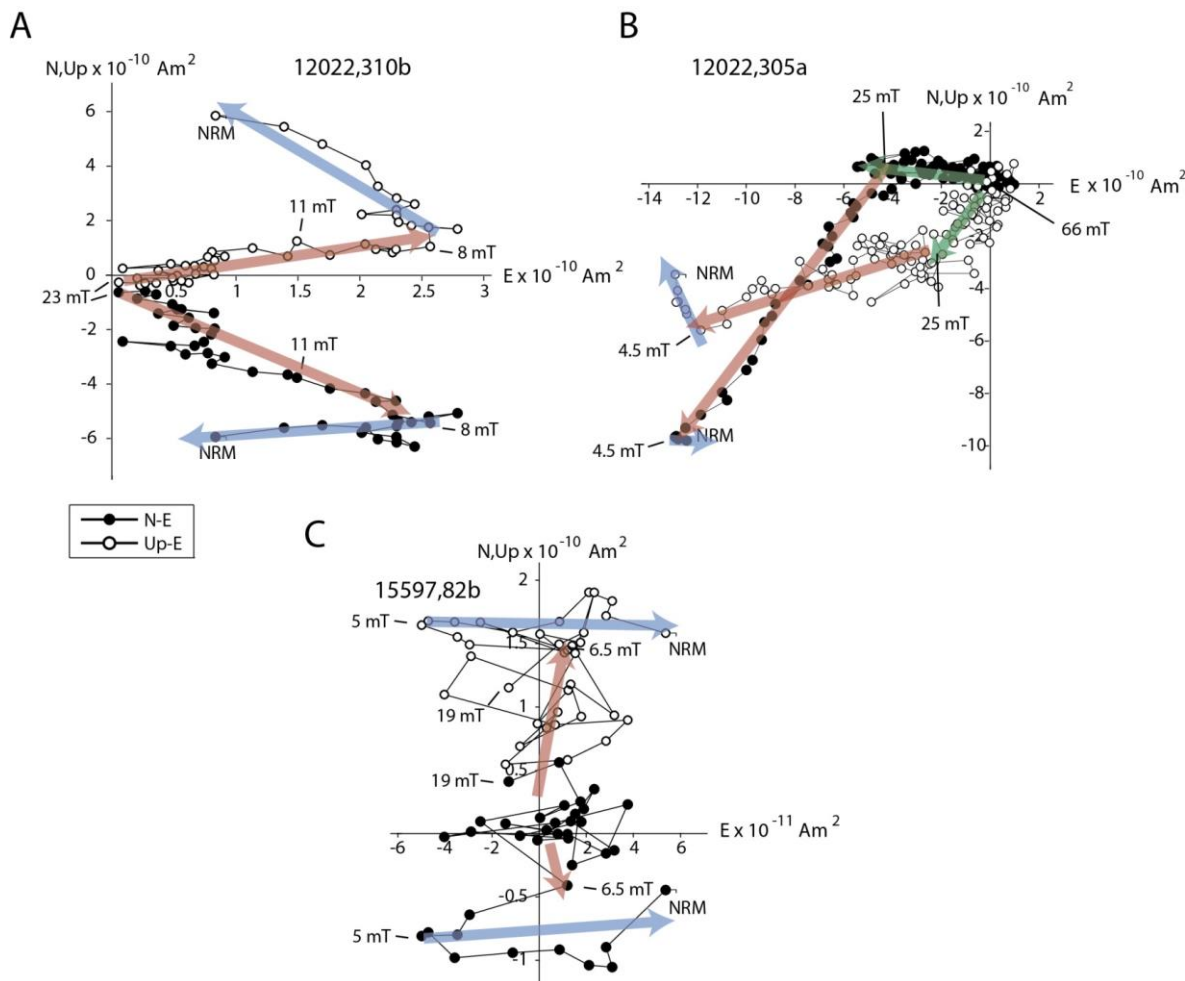
Figure S5. AF demagnetization of subsamples from 12022 and 15597. Open and closed circles represent projections of the NRM vector onto the vertical (Z-E) and horizontal planes (N-E), respectively. Blue, red, and green arrows denote LC, MC1, and MC2 components, respectively. Selected AF levels are labeled. (A) 12022,310b. (B) 12022,305a. (C) 15597,82b.

387

3.4. Interpretation of 12022 NRM demagnetization data

389

3.4.1. LC/LT components. We now discuss the origin of the LC/LT components, which are blocked up to 8 mT and 86°C. We take advantage of the fact that our subsamples were likely stored for 41 y in different orientations in the presence of Earth's magnetic field (see Section 2 of main text), which allows us to test for the acquisition of VRM. A long-term VRM should be approximately unidirectional across subsamples recently cut from the same parent chip, but non-unidirectional when comparing different parent chips that were in different relative orientations with respect to the ambient field over the last 40 y. We observe both of these properties for the LC/LT components from our 12022 subsamples.

398

13
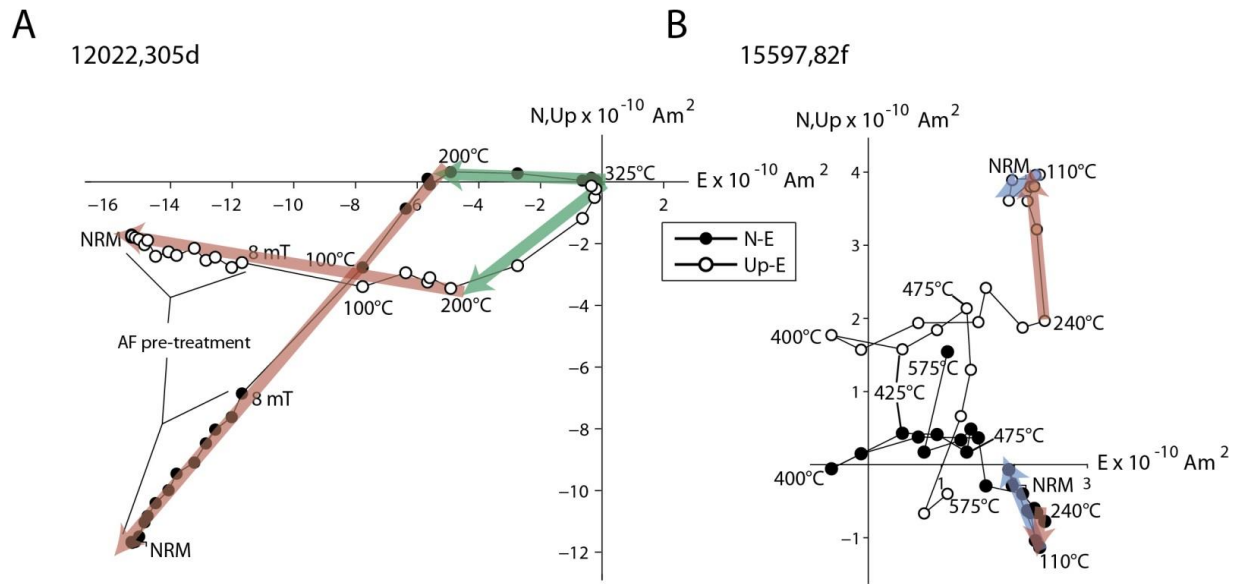
Figure S6. Thermal demagnetization of subsamples from 12022 and 15597. Open and closed circles represent projections of the NRM vector onto the vertical (Z-E) and horizontal planes (N-E), respectively. Blue, red, and green arrows denote LT, MT1, and MT2 components, respectively. Selected temperature steps are labeled. (A) 12022,305d. (B) 15597,82f.

An additional criterion for identifying VRM is that it should be blocked in grains with low blocking temperatures and mostly low coercivities. In particular, for single domain kamacite, VRM is expected to be carried by grains with 1000 s blocking temperatures of ~125°C (Garrick-Bethell and Weiss, 2010). With the caveats that 12022 is predominantly multidomain and contains both kamacite and martensite (Sections 2.2 and 5.2), this prediction is broadly consistent with the 86°C peak blocking temperature of the LT component (Section 3.3.4).

VRM is also consistent with the Earth-strength paleointensities we obtain for the LC component from our experiments (main text Section 4.2 and Table S3). Although an isothermal remanent magnetization (IRM) might also be blocked to low coercivities like VRM, the ratios of the LC magnetization intensity to that of IRM over its coercivity range of 0.01-0.03 are in the range expected for VRM acquired in Earth's field (main text Section 4.2 and Table S3) and far below the 0.1-1 values expected for an IRM. Furthermore, our laboratory VRM acquisition experiments (Section 5.5) on a 12022 subsample indicate that VRM could account for between 3% to 85% of its total NRM. These values bound the actual NRM fraction contained in its LC component (36%). Therefore, we conclude that the LC/LT components in 12022 are most likely VRM.

3.4.2. MC/MT components

3.4.2.1. Overview. As discussed above, we observed MC/MT components blocked up to ~85 mT and ~325°C. The MC1/MT1 components from the subsamples from each JSC parent block (e.g., 305, 308, and 310) are approximately unidirectional (mean directions range up to 40° apart), but are clearly divergent from the MC1/MT2 and MC2/MT2 directions of subsamples

14

from the other parent blocks. We found that the highest coercivity stable magnetization (MC1/MT1 or MC2/MT2) present in each subsample was nearly always origin-trending (with the exception of 310c), indicating that a characteristic magnetization component was isolated. Because the MC/MT components are unidirectional within each parent chip, we infer that they predate subsampling at MIT. Therefore, they either formed on the Moon or during subsequent sample handling during return to Earth or at JSC.

Since 12022 does not show any petrographic evidence of post-eruptive aqueous alteration, it is unlikely that the MC/MT components identified in the sample result from secondary chemical remanent magnetization (CRM). The remaining explanations for the origin of the 12022 MC magnetizations are VRM, total TRM, pTRM, IRM, shock remanent magnetization (SRM), and drilling-induced remanent magnetization (DIRM) (which is actually a poorly defined combination of the aforementioned processes). We can distinguish between these process by comparing their rate of AF demagnetization to that of various laboratory-induced magnetizations: ARM (acquired in a 85 mT AC field and 0.5 mT DC field) as a nondestructive analog for total TRM (Stephenson and Collinson, 1974), IRM (acquired in a 200 mT field) as an analog for strong fields during sample handling like application of magnets, and pressure remanent magnetization (PRM) (acquired in a 750 µT field at 1.08 GPa) as an analog for SRM (Section 5.4 and Fig. 3).

3.4.2.2. Total TRM and IRM. The MC1 component of 310a demagnetized at lower AF levels compared to ARM and IRM and has effectively been completely removed by ~35 mT. Similarly, the MC1 and MC2 components of 305b demagnetized at lower AF levels compared to ARM and IRM and all NRM is removed by 78 mT. This demonstrates that total TRM and IRM are unlikely to be the sources of the MC1 and MC2 components in 12022. Furthermore, the NRM/IRM ratios ranging from 0.008 to 0.05 for the MC1 and MC2 component coercivity ranges are probably too low for IRM to be the source of either component in 12022.

3.4.2.3. VRM. As discussed in Section 5.5, our VRM acquisition experiments indicate that VRM acquired in the Earth's 50 µT magnetic field over 41 years is unlikely to explain the entire NRM in these samples. Considering that we ascribe the LC/LT component to VRM, it would be unusual for a second relatively well-defined component also to be VRM given the typically logarithmic time-dependence of VRM acquisition (Dunlop and Ozdemir, 1997). Therefore, the MC1/MT1 components of subsamples with well-defined LC/LT components (i.e., blocks 308 and 310, whose LC/LT components carry 21-40% of the total moment in each subsample) are not likely to be VRM. On the other hand, only 2 out of 4 subsamples from block 305 even had a LC/LT component (which only carried 0-11% of the moment in each subsample). Because blocks 308 and 310 had substantial VRM components, it stands to reason that block 305 would also have one. The MC1/MT1 component of block 305 carries 54-73% of the moment in each subsample. While the 200°C peak unblocking temperature of the MT1 component in block 305 exceeds the expected 125°C peak 1000-s blocking temperature for a 41 year terrestrial VRM carried by single domain kamacite (Garrick-Bethell and Weiss, 2010), this disparity may be due to the presence of multidomain grains and martensite in 12022. Therefore, our data suggest that the MC1/MT1 component in block 305 is a VRM. The MC2/MT2 component in block 305 is unlikely to be VRM because of its higher ~325°C peak unblocking temperature and the typically logarithmic time-dependence of VRM acquisition.

15

469

470   *3.4.2.4. Lunar SRM.* The normalized AF demagnetization spectra of the MC1 component and
471   PRM are similar (Fig. S8). However, even for the highest possible shock pressure experienced
472   by the sample since formation (5 GPa), an ambient magnetic field of over 300 µT is required to
473   reproduce the moment magnitude of the MC components (Section 5.4). No evidence for 300 µT
474   dynamo or crustal remanent fields has yet been reported for the Moon. Although >300 µT
475   impact plasma-generated fields are conceivable (Crawford and Schultz, 1999), the longest
476   duration (e.g., 1 day) fields at the antipodes of basin-forming impacts are not thought to have
477   exceeded ~10 µT (Hood and Artemieva, 2008). Therefore, it is unlikely that the MC1/MT1 and
478   MC2/MT2 components are SRMs.

479

480   *3.4.2.5. Nonthermal DIRM from saw cutting.* Drilling or cutting a sample may produce multiple
481   moderate coercivity, nonunidirectional magnetization, sometimes referred to as DIRM
482   (Audunsson and Levi, 1989; Burmester, 1977; Fuller et al., 1998; Jackson and Van der Voo,
483   1985; Kodama, 1984; Pinto and McWilliams, 1990). DIRM might be a PRM, a secondary IRM
484   overprint or surficial contamination from a saw blade (Burmester, 1977). It has also been
485   suggested that DIRM can result from the cutting of large multidomain grains, resulting in a
486   pressure-driven realignment of domain walls in the presence of a local field (Jackson and Van
487   der Voo, 1985). As established above, IRM cannot account for the MC components in 12022
488   (Audunsson and Levi, 1989). While the demagnetization of NRM and a 1.08 GPa PRM acquired
489   in a 750 µT field are similar over the MC coercivity range, it is unlikely that the saw cutting
490   process was able to generate the high pressures necessary to reproduce the magnetization
491   intensity of the MC components of our subsamples given ambient laboratory fields at JSC
492   (almost everywhere <100 µT in the present-day lab according to our fluxgate magnetometry
493   measurements). If saw cutting could induce such an intense PRM component that persists to
494   such high coercivities, PRM would be observed in all paleomagnetic studies with samples that
495   have been wet-cut or wet-drilled, and this is not the case.
496   Surface contamination from saw blade material is also highly unlikely to have occurred
497   in our study because prior to the demagnetization experiments, we sanded the faces of all JSC
498   saw cut and MIT wire saw cut surfaces until saw marks could no longer be seen. After several
499   subsamples (308a and 308b) had already been measured following that procedure, we decided to
500   test whether the remanence in our sample could actually have been from cutting through
501   multidomain grains at JSC.   We calculated the mass of material that would need to be sanded
502   away from each saw cut face from subsample 308c prior to measuring it such that the largest (30
503   µm diameter) multidomain iron grains were removed in the process.   Given the dimensions and
504   shapes of that subsample, ~1-1.5 mg per face would need to be sanded away to ensure the
505   removal of all cut multidomain grains from this subsample. Prior to any demagnetization
506   experiments, we removed 2 mg from each face of this subsample. The LC1 and MC1
507   components of 308c were essentially identical to those of 308a and 308b. This amount of
508   material removal (~2 mg per face) is similar to the amount sanded off for all other subsamples in
509   this study. Furthermore, two of our subsamples (305c and 305d) do not actually have any JSC
510   saw cut faces and they have the same MC1/MT1 and MC2/MT2 components and magnetization
511   directions as the other subsamples 305a and 305b from the same parent block. Therefore, DIRM
512   from cutting of multidomain grains cannot explain the MC components in any of our
513   subsamples.

514

16

3.4.2.6. pTRM from saw cutting. Another possibility is that the 12022 subsamples acquired a pTRM from frictional heating during the saw cutting process. Personal communication with former Lunar Receiving Laboratory employee David Mann revealed that circular saw cutting of Apollo 12 samples (see Section 1.2 and Fig S1a) was conducted without any liquid coolant. Mann recounted to us how the saw blade became increasingly hot during the saw cutting process until it ultimately failed and stopped cutting. This failure was ascribed to thermal expansion and warping of the saw blade in combination with smearing of the Cu-based bonding agent that attached the diamond grit to the metal base of the blade. Blades would typically fail after 20-30 minutes of use, at which point they would be replaced. Because a ~10 cm diameter rock could require changing saw blades 2-5 times, each blade was used to cut 2-5 cm into the rock. Our communication with a technician from Husqvarna, a company that produces similar tile saw blades, revealed that the melting temperature of the Cu-based bonding agent is between 680-700°C. To test the hypothesis that the MT components are from dry saw cutting, we (*i*) conducted thermal diffusion calculations, (*ii*) conducted our own dry-cutting experiment (Section 6), and (*iii*) analyzed the composition and structure of surfaces of 12022 samples that were dry cut with a circular saw at JSC.

(*i*) We conducted thermal diffusion calculations for sawing-induced heating to constrain the peak temperature as function of depth within the sample (0.5-2 cm). We modeled the basalt as a half-space with a constant temperature being applied across the surface. We assumed that diffusion is the only mechanism of heat transfer and used a conservatively low thermal diffusivity for basalt of 5×10^{-7} $m^2 s^{-1}$ (Hanley et al., 1978). Independently of the surface temperature, we find that after 100 s (a relatively short period of time compared to the ~20 minute cutting lifetime of each saw blade), a rock will reach ~65% of the surface temperature at a depth of 0.5 cm into the rock (Fig. S7a). If a surface temperature of 500°C is applied for 100 s and then removed, even 250 s after the start of heating (150 s after heat removal), the temperature will still be 215°C at a distance of 0.5 cm into the rock. After 1000 s, temperatures at 0.5 cm depth will still be nearly 100°C according to this model (Fig. S7b). Therefore, the rock will stay warm long enough to acquire significant pTRM.

(*ii*) We conducted an experiment in which we dry-cut a terrestrial andesite using a circular saw to mimic the cutting of 12022 in 1970. We then demagnetized various subsamples from both the vicinity of the saw cut face as well as control subsamples collected prior to dry saw cutting. Demagnetization data from these terrestrial subsamples suggest that dry cutting caused temperatures to reach 230°C at the saw cut face and 160°C at a distance of 3.5 mm away from the saw cut face (Section 6). Therefore, heating from dry saw cutting is likely a real contributor to the NRM of lunar samples that have been dry cut with circular or band saws.

(*iii*) Our BSEM analyses of a circular saw cut face from an additional sample, 12022,322, revealed swaths of metal smeared onto the surface of the sample (Fig. S8). Our electron microprobe analyses determined that the composition of the smeared metal was ~$Fe_{0.75}Ni_{0.15}Cr_{0.05}$. Because this composition is consistent with an alloy of steel and differs significantly from any natural metal grains observed in the sample itself (see Section 2.2.2), this metal must have originated from the circular saw blade used to cut the rock in 1970. This smearing is suggestive of elevated temperatures in the cutting interface. However, the exact temperature necessary to achieve such a smearing effect is unknown. A prior BSEM analysis of lunar impact melt breccia 73235 showed that dry cutting a sample using a band saw produced smearing of saw blade material as well as layers of glassy, amorphous material on the rock surface consistent with localized melting of the surface rock (Todd, 2012). This indicated that

17

561   73235 may have been locally exposed to temperatures between 1250-1500°C during the cutting
562   process. We did not observe any melt phases during our BSEM analysis of 12022, so we can
563   assume that while significant heating may have occurred during saw cutting of our samples, the
564   temperatures reached were certainly less than 1250°C, and probably less than 700°C since we
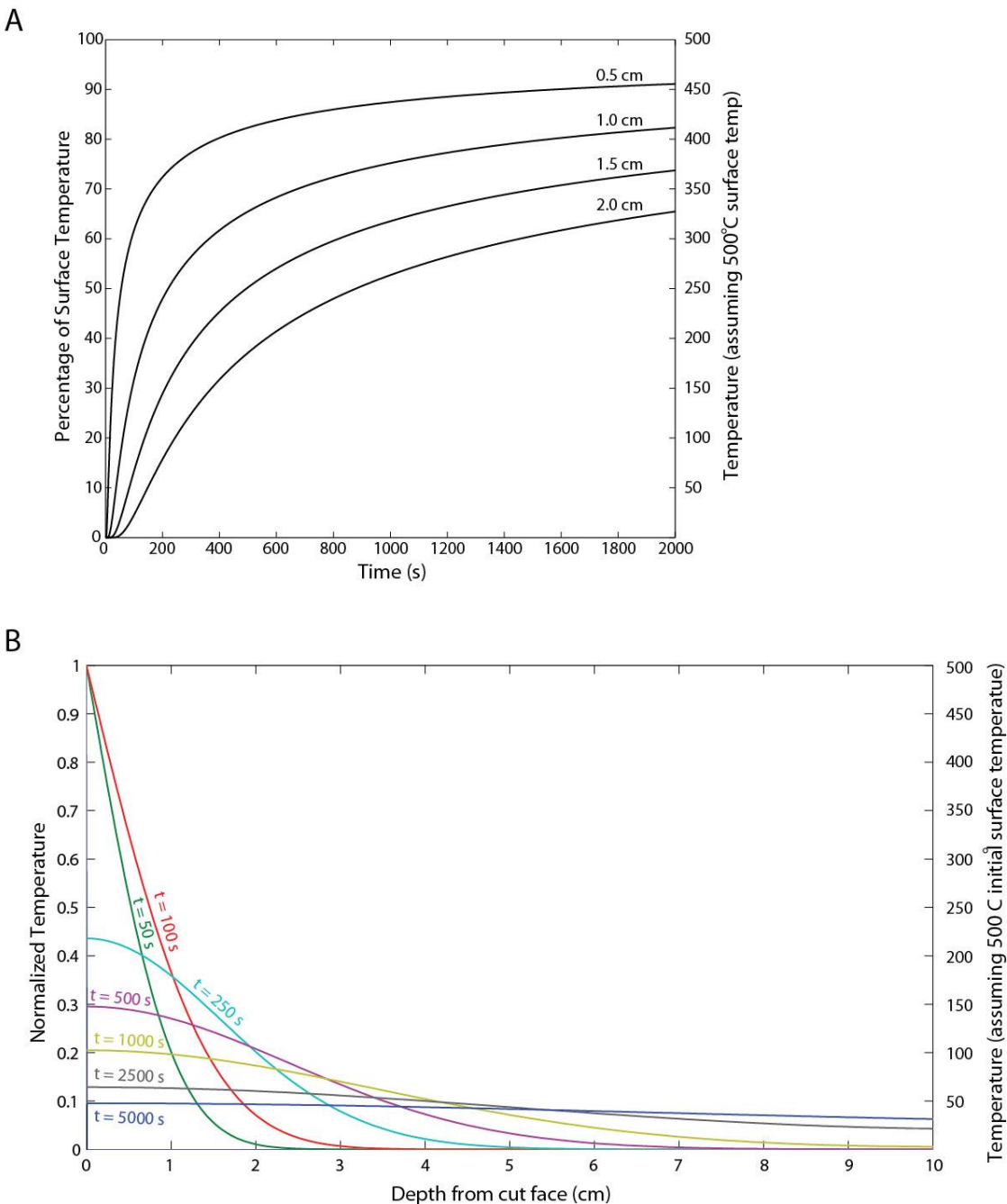
Figure S7. Half-plane model of saw cut heating. (A) Percentage of saw cut face surface temperatures reached at various depths (0.5 cm to 2 cm) into a rock for saw cutting timescales of 0 to 2000 s. (B) Percentage of saw cut face temperatures reached after cutting for 100 s followed by cooling for different periods of time. Time is defined from the beginning of heat application.

18
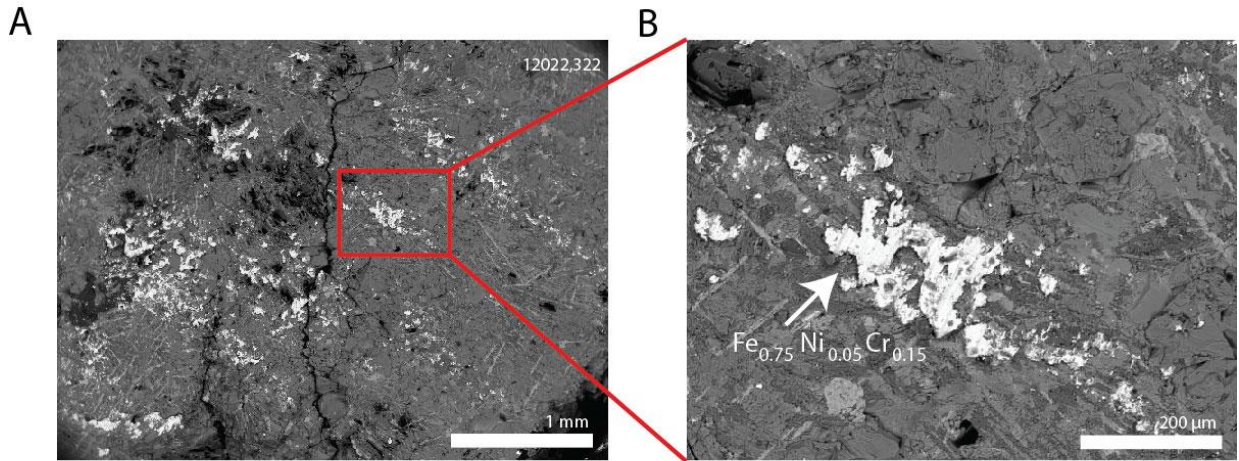
Figure S8. BSEM images of saw blade metal smeared on the circular saw cut surface of 12022,322. Figure part (B) is a magnification of part (A). Composition of smeared metal is labeled.

565 also did not observe any melted Cu-Ni bonding agent during our BSEM analyses. Ref. (Reid et
566 al., 1970) noted in their metal analysis of 12022 that they found a "single grain of approximate
567 composition Cu58, Ni22, Znl7 and Fe2 (weight percent)" which matched the composition of a
568 commercial alloy called "nickel-silver". This grain could have been either high temperature
569 melt/smearing or low temperature chipped off material from either the circular saw blade or the
570 wire from a wire saw used in sample preparation.
571   Based on these observations, it is highly likely that our samples acquired pTRM from
572 saw cut heating which reached peak temperatures between 80-700°C. This is consistent with the
573 Earth-strength paleointensity of the MC/MT components (Table S3). pTRM in multidomain
574 grains may not unblock until temperatures much higher than the temperature the remanence was
575 acquired at (Dunlop and Ozdemir, 2001). Therefore, even if the surfaces of our 12022
576 subsamples were only heated to a few hundred °C, it is possible that the MC1/MT1 component
577 of blocks 308 and 310 (which was removed by 240°C in subsample 310c) and the MC2/MT2
578 component in block 305 [which was removed by ~325°C in subsample 305d (peak temperatures
579 for each thermal step were held for ~20 minutes)], are the result of pTRM acquired during the
580 saw cutting process.
581
582 *3.4.3. High coercivity behavior.* At AF levels above the end of the MC1 or MC2 components
583 (whichever is highest in given subsample), magnetization directions were scattered and non-
584 unidirectional with respect to each other for subsamples from both within the same parent chip as
585 well as when comparing different parent chips (Fig. S9). We were therefore unable to identify
586 any additional unidirectional, stable magnetization which could be attributable to TRM acquired
587 in a lunar dynamo magnetic field using AF demagnetization.

588
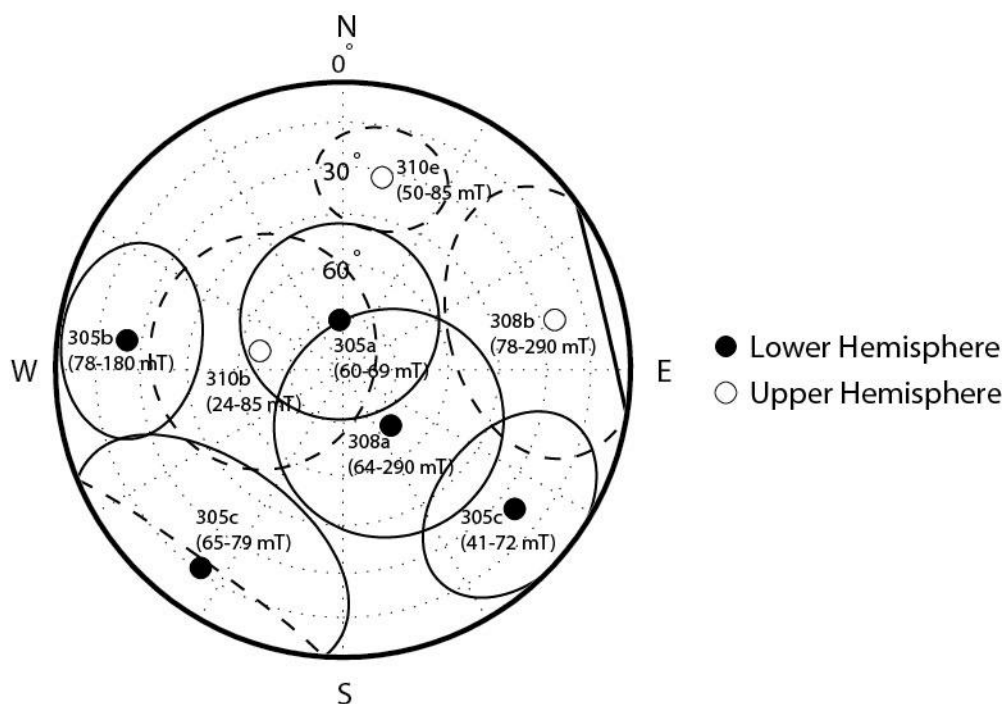
Figure S9. Equal area stereographic projections of PCA fits for high coercivity magnetization in 12022 subsamples. Subsamples and AF levels used in the PCA fits are labeled. Open circles (dashed lines) represent directions in the upper hemisphere, while filled circles (solid lines) represent directions in the lower hemisphere.

589   *3.5.   15597.* All 5 AF-demagnetized subsamples had LC components blocked up to ~5 mT
590   and the one thermally demagnetized subsample had an LT component blocked to 110°C (Table
591   S2).   The LC/LT components were nonunidirectional (i.e., mean directions were up to 120°
592   apart) (Fig. S10a). MAD values from the LC/LT PCA fits were >18° for 4 out of 6 subsamples,
593   indicating that most of these components were poorly defined. 4 out of 6 subsamples of 15597
594   also had variably defined (unconstrained MAD values ranging between 9-35°) MC1 components
595   ranging between ~5 and ~20 mT or MT1 blocked between 110 and 240°C. The MC1/MT1
596   magnetization directions were also inconsistent between subsamples (i.e., mean directions were
597   up to 130° apart) (Fig. S10b). The MC1 components of subsamples 82b and 82c are origin-
598   trending according to the DANG/MAD test. Although the MC component of a third subsample
599   failed the DANG/MAD test, using this test may yield incorrect results for samples in which
600   spurious ARM during AF demagnetization might have had a deleterious effect (Section 3.2.3).
601   We could not identify any origin-trending magnetization components during thermal
602   demagnetization of subsample 82f, possibly due to sample alteration, spontaneous (i.e., zero-
603   field) magnetization, or interaction effects.
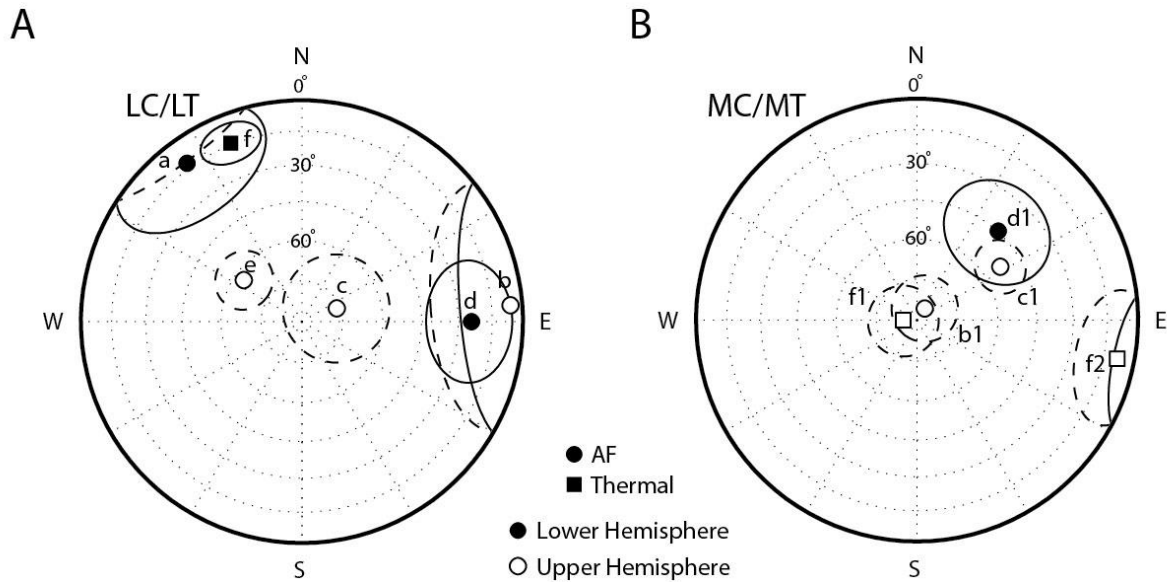
Figure S10. Equal area stereographic projections of the magnetization components observed for sample 15597. (A) LC (circles) and LT (squares) component directions. (B) MC (circles) and MT (squares) components directions. Lines encircling component directions represent the MAD associated with the component. Open symbols (dashed lines) represent directions in the upper hemisphere, while filled symbols (solid lines) represent directions in the lower hemisphere.

3.5.1. Demagnetization of subsample 15597,82a. This subsample has a poorly defined (unconstrained MAD value of 24.4°), non-origin-trending LC component that is removed by 4 mT. Beyond this AF level, no additional magnetization components could be identified. A PCA fit to the data above this level yields a MAD value of 38.1°, which approaches the MAD of a random distribution of points on a sphere (see Section 3.2.3) and indicates a nearly random set of directions. The high MAD values (> 20° for both the LC component and higher AF levels) and the associated directional scatter in magnetization directions during demagnetization suggest that the characteristic remanence in this sample might have been obscured by spurious ARM.

3.5.2. Demagnetization of subsample 15597,82b. This subsample has a LC component blocked from NRM to 6.5 mT as well as a noisy (unconstrained MAD value of 35.2°) but origin-trending MC1 component from 6.5 to 19 mT. No further magnetic components were identified.

3.5.3. Demagnetization of subsample 15597,82c. This subsample has a LC component that was removed by 4 mT, followed by a noisy (unconstrained MAD value of 25.8°), origin-trending, MC1 component up to 16 mT. No additional components could be identified.

3.5.4. Demagnetization of subsample 15597,82d. The LC component of this subsample was removed by 4 mT. The sample also had a noisy (unconstrained MAD value of 20.4°), non-origin trending MC1 component between 4.0 and 19.0 mT. The MAD for points between AF 20 mT and AF 290 mT was quite high (37.2°), indicating that the characteristic remanence in the sample was likely obscured.

3.5.5. Demagnetization of subsample 15597,82e. This subsample had a well-defined, origin-trending LC component blocked up to 9.5 mT. No additional components were identified.

3.5.6. Demagnetization of subsample 15597,82f. Thermal demagnetization (without AF pretreatment) revealed an LT component which was removed by 110°C, and a non-origin-trending MT1 component that was blocked to 240°C. A weak magnetization may exist above this temperature but it is obscured by anomalous demagnetization effects.

3.6.   Interpretation of NRM demagnetization data.

3.6.1.   LC/LT and MC/MT behavior. The lack of aqueous alteration features excludes secondary weathering CRM as the source of any magnetization in 15597. The fact that the LC/LT and MC1/MT1 components are non-unidirectional magnetization is inconsistent with either being a total TRM. As described in Section 4 of the main text, additional confirmatory evidence for a non-primary origin of these components is their low coercivity relative to the peak grain coercivities in the rock and the near-zero paleointensities retrieved for higher coercivity ranges. In contrast to 12022, pTRM from saw cutting is impossible because 15597 has never been cut with a circular saw or band saw. Normalized AF demagnetization curves comparing the NRM of subsample 82b to other forms of remanence show that the LC component of 15597 is also inconsistent with a SRM origin (Fig. S11a). As discussed above for 12022, magnetic fields on the Moon are anyway unlikely to have been strong enough to impart a SRM of equivalent intensity to the NRM of the MC1 component. The similarity of the demagnetization of the LC and MC1 components to ARM and IRM (Fig. S11b) suggests that (*i*) viscously decayed IRM and (*ii*) VRM are the most likely sources for these components. We discuss each of these possibilities below.

(*i*) While IRM is in principle capable of inducing non-unidirectional overprints due to the curved nature of fields near magnetized objects, the NRM/IRM ratios over the coercivity range of the LC and MC1 components (ranging between 0.001 and 0.016) are below the values usually indicative of an IRM origin (0.1-1). Therefore, secondary IRM from sample handling at JSC or spacecraft transport is unlikely, although it is conceivable that such an IRM could have viscously decayed during the 42 years since sample return.

(*ii*) A previous study has shown that 15597 is extremely susceptible to VRM acquisition, likely because of the presence of ultrafine iron grains in the glass portion of this vitrophyric basalt (Fuller et al., 1979). Our VRM acquisition experiments (Section 5.5) confirm this. The removal of the LT component in subsample 82f by 110°C is also suggestive of a VRM origin for the LC/LT components in 15597. The 240°C peak unblocking temperature of the MT1 component suggests that it might also be a VRM. Also consistent with a VRM origin is the approximately Earth-strength paleointensities LC/LT and MC/MT components (see Section 4 of main text). A caveat is that the overall non-unidirectionality of both the LC/LT and MC/MT1 components present in these samples seems to challenge a VRM origin. A possible explanation is that the sample was almost certainly rotated multiple times since it was returned to Earth, such that different regions within the sample acquired VRM at different rates, creating non-unidirectional magnetization within the sample.
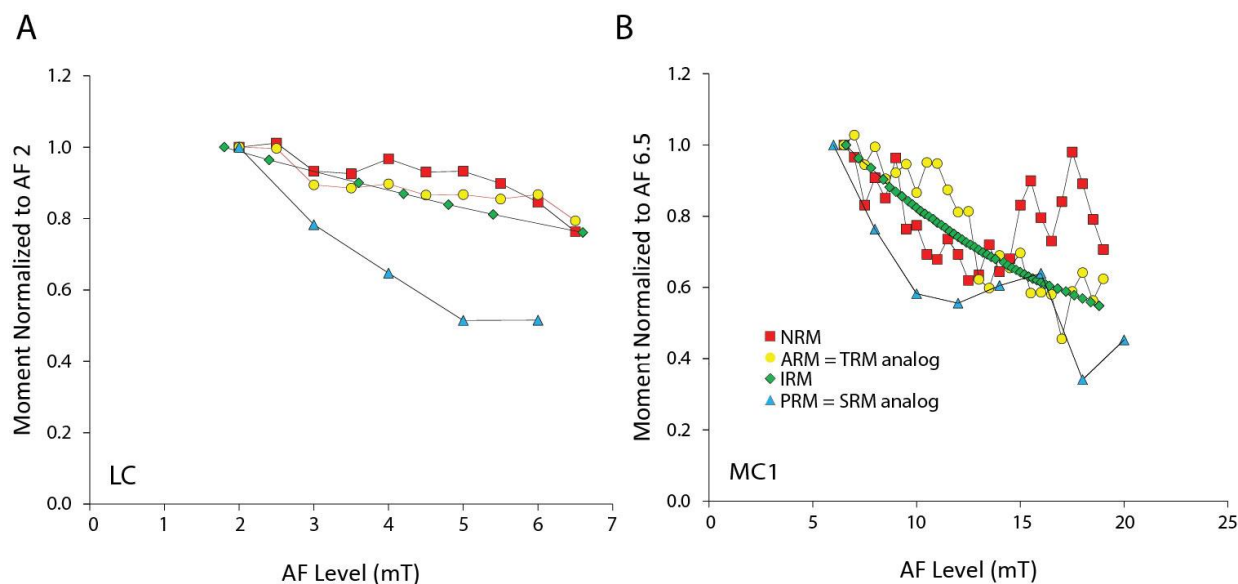
Figure S11. AF demagnetization of sample 15597,82b. Shown is the intensity of NRM (red squares) during AF demagnetization compared to that of various forms of laboratory-induced magnetization: ARM acquired in a 85 mT AC field and 0.2 mT DC bias field (yellow circles), IRM acquired in a 200 mT field (green diamonds), and PRM acquired in a field of 0.75 mT at a pressure of 1.08 GPa (blue triangles). (A) Magnetization normalized to 2 mT step to emphasize comparison between LC component and laboratory magnetizations. (B) Magnetization normalized to 6.5 mT AF step to emphasize comparison between MC1 component and laboratory magnetizations.
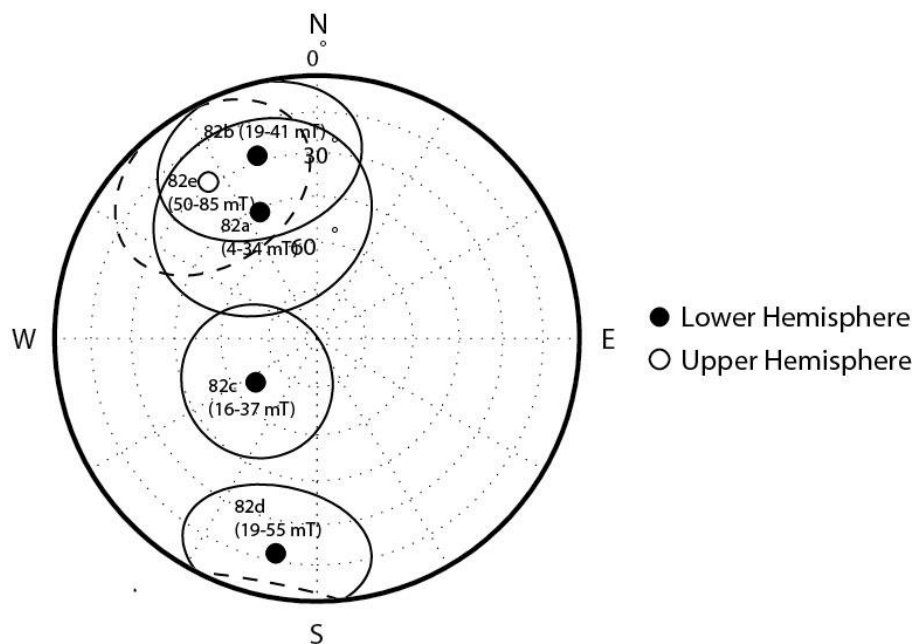
Figure S12. Equal area stereographic projections of PCA fits for high coercivity magnetization in 15597 subsamples. Subsamples and AF levels used in the PCA fits are labeled. Open circles (dashed lines) represent directions in the upper hemisphere, while filled circles (solid lines) represent directions in the lower hemisphere.

673   *3.6.2.*   *HC behavior.*   For each subsample, magnetization directions are scattered and non-
674   unidirectional with respect to each other at AF levels above the end of the highest coercivity
675   component (MC1 or MC2) (Fig. S12). This indicates that we were unable to identify any

676 unidirectional, stable magnetization which could be attributable to TRM acquired in a lunar
677 dynamo magnetic field.
678
679
680 **4.   Paleointensity**
681
682 *4.1. Methods.* We primarily used the nondestructive ARM and IRM methods to determine
683 paleointensities for the magnetization components present in our samples (Garrick-Bethell et al.,
684 2009; Shea et al., 2012; Suavet et al., 2013; Yu, 2010) rather than thermal methods which can
685 cause destructive chemical alteration to the samples. Thermal paleointensity experiments were
686 conducted on one subsample from each parent rock (12022,310c and 15597,82f).
687
688 *4.1.1. Thermal methods.* In our thermal experiments, we compared the stepwise demagnetization
689 of NRM up to 575°C with that of a pTRM acquired in a 10 µT dc field at the same peak
690 temperature. We did not use a 780°C total TRM in order to avoid reduction of ilmenite into iron
691 and rutile at temperatures >600°C (Pearce et al., 1976). Thermal demagnetization of a control
692 sample, 12022,308b, to 600°C led to a factor of 3 increase in its saturation IRM, indicating
693 significant sample alteration and the likelihood that our thermal paleointensities are
694 underestimates. Paleointensities from the pTRM method are calculated using the following
695 formula:
696
697   pTRM paleointensity in µT = (NRM lost)/(TRM lost)·(laboratory DC field)
698
699 *4.1.2. AF-based methods.* Formulas for the ARM and IRM methods are given in Section 4 of
700 the main text. As discussed in the main text, there are some uncertainties regarding the values
701 which should be used for the calibration constants (*f'* for the ARM method and *a* for the IRM
702 method). The normalized IRM paleointensity data for many samples (Muxworthy et al., 2011;
703 Weiss et al., 2007) demonstrate that the range of possible *a* values is well-approximated by a
704 lognormal distribution (Fig. S13), with ~86% and 98% of paleointensity values from Muxworthy
705 et al. (2011) contained within a factor of 3 and 5, respectively, of the mean value. We adopted
706 values of *f'* = 1.34 and *a* = 3000 µT (Gattacceca and Rochette, 2004; Stephenson and Collinson,
707 1974). An *a* value of ~4700 µT (within factor 2 of 3000 µT) was previously obtained from
708 comparing thermal paleointensity results and the NRM/IRM ratios for more than a dozen lunar
709 samples (Cisowski et al., 1983). Although these estimates for *a* may be somewhat affected by
710 alteration during heating experiments, they are all broadly consistent with the *a*-value we adopt
711 in this study. Using the ~5 µT paleointensity from Helsley (1971) and the TRM/IRM ratio
712 provided for sample 12022 by Cisowski et al. (1983), we can directly estimate that *a* has a value
713 of 1163 µT for this sample. However, we chose not to adopt this value for our paleointensity
714 determinations since it is uncertain whether it is accurate due to probable thermal alteration of
715 the sample during the calibration experiment. Because we did not give 12022 a total TRM in
716 any of our experiments (to avoid alteration from heating), we could not determine a new value
717 for *a*.
718
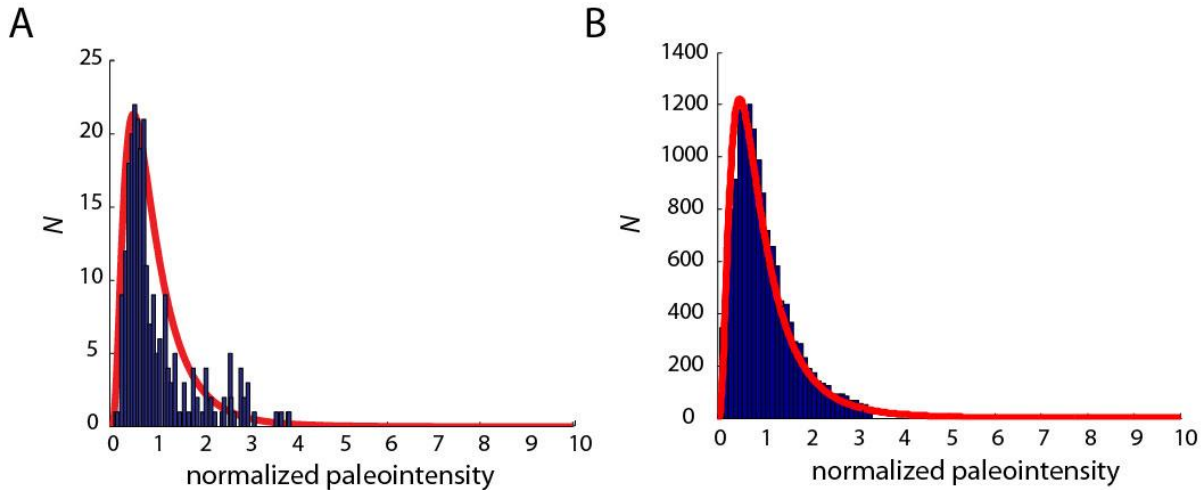
Figure S13. Histograms of normalized IRM paleointensities from two prior studies. (A) IRM paleointensities of 251 terrestrial and synthetic samples magnetized in identical field strengths. Data are from Fig. 14d of Muxworthy et al. (2011) and paleointensity values are normalized to the mean value. (B) Normalized IRM paleointensities from over 14,000 Superconducting Quantum Interference Device (SQUID) microscopy measurements obtained from a Hawaiian basalt. Data are from Fig. 2h of Weiss et al. (2007). Paleointensity values are normalized to the mean value. In (A) and (B), the vertical axes give the number of counts per bin of data and the horizontal axes contain the normalized paleointensity values. The red curves are lognormal distribution fits to the data.

719

720 *4.2. Paleointensity results.* We report slopes for NRM lost versus ARM gained, NRM lost
721 versus IRM lost, and NRM lost versus pTRM lost for all magnetization components as well as
722 computed paleointensity values for those components likely to be of VRM or pTRM origin
723 (Table S3). The paleointensity formal uncertainties quoted in the table are 95% confidence
724 intervals computed by a two-tailed Student *t*-test (Weisberg, 1985) and reflect only scatter
725 associated with linear regressions (not the aforementioned systematic uncertainties associated
726 with the unknown ratios of TRM to ARM and IRM).

727 AF-based paleointensity results are summarized in the main text. For both 12022 and
728 15597, LC, MC1, and MC2 (if present) component paleointensities are within error of the
729 Earth's field strength (mean values are several tens of µT). Above the end of the highest
730 coercivity component, paleointensities were either within error of zero or below the samples'
731 paleointensity fidelity limit (see Section 4 of main text) (Fig. S14). For subsample 12022,310c,
732 we determined thermal paleointensities of 21 ± 95 µT and 8 ± 2 µT for the LT and MT1
733 components, respectively. The formal uncertainty of the LT component is large because there
734 were only 3 data points [the linear fit of these points is acceptable (the R^2 correlation coefficient
735 value was 0.88)]. Therefore, we accept the mean value of ~21 µT as the paleointensity for this
736 component. The low thermal paleointensity we obtain for the MT1 component is similar to the
737 4.9 µT value previously obtained by Helsley (1971). Both values are lower than our ARM and
738 IRM paleointensities almost certainly because of sample alteration (Supplementary material).
739 For subsample 15597,82f, we found paleointensities of 23 ± 21 µT and 16 ± 18 µT for the LT
740 and MT1 components, respectively.

741
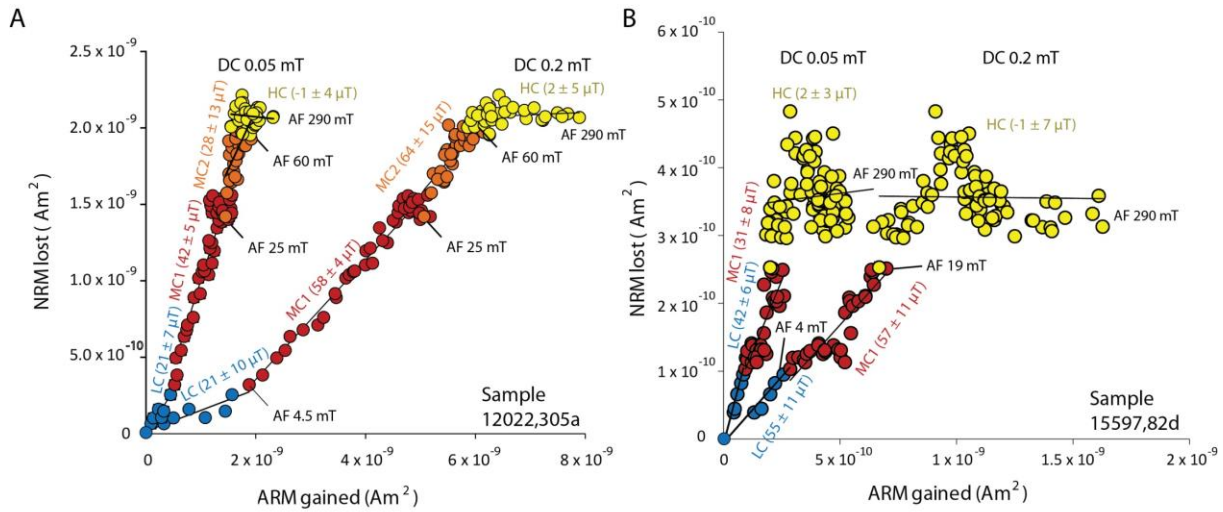
Figure S14. ARM paleointensity plots depicting NRM lost during AF demagnetization as a function of ARM gained during stepwise acquisition (AC field increasing to 85 mT, DC bias fields = 0.05 and 0.2 mT) at an equivalent AC field. (A) Sample 12022,305a, (B) Sample 15597,82d. Labels note component type, AF levels, DC bias fields, and paleointensities. Points corresponding to the LC, MC1, and MC2 components in samples are shown with blue, red, and orange circles, respectively, while demagnetization data from higher AF levels are shown in yellow.

742   **5.   Rock magnetism and domain state**

743

744   *5.1. Previous rock magnetic studies.* Hysteresis and rock magnetic parameters were previously
745   measured for samples 12022,52 and 15597,20 (Fuller et al., 1979), as well as on an additional
746   subsample of 15597 by ref. (Cournède et al., 2012).   We summarize previously determined rock
747   magnetic properties for 12022 and 15597 from these studies (Table S5).   Rock magnetic
748   parameters including the saturation magnetization (M_s), saturation remanent magnetization (M_{rs}),
749   coercivity (H_c), and remanent coercivity (H_{cr}) for sample 12022 are consistent with an overall
750   multidomain mineralogy for the sample when plotted on a Dunlop-Day plot (Dunlop, 2002).
751   The rock magnetic properties for 15597 suggest a bulk magnetic mineralogy in the pseudo-single
752   domain to multidomain range.

753

754   *5.2. Hysteresis curves.* To assess the domain state of our samples, new hysteresis loops were
755   measured for subsamples 12022,310a and 15597,82b using a Princeton Instruments MicroMag
756   Vibrating Sample Magnetometer in the paleomagnetism laboratory at CEREGE. The H_{cr} values
757   presented here were determined from remanence curve measurements at CEREGE (see Section
758   5.3). Our hysteresis properties for 12022 and 15597 (Table S5) suggest multidomain magnetic
759   mineralogies for both samples, and are similar to those previously reported in the preceding
760   section. A representative hysteresis loop is shown for sample 12022 (Fig. S15).

761

26

762   *5.3. Rock magnetic properties.*   We performed a series of rock magnetic characterization
763   experiments on subsamples 12022,310a and 15597,82b to assess their magnetic recording
764   properties. First, each sample was progressively given ARM using an AC field of 200 mT and
765   DC bias fields incrementally increasing from 0 to 2 mT. This allows one to determine the
766   Cisowski *R*-value, an indicator of the extent of magnetostatic interactions (Cisowski, 1981). The
767   final ARM applied (peak AC field = 200 mT, DC field = 2 mT) was AF demagnetized at
768   increasing fields to 290 mT. This allowed us to calculate the median destructive field (MDF; i.e.
769   the peak AC field required to reduce the magnetization by half) of ARM for each sample.
770   Similarly, we determined the median destructive field of IRM by applying and subsequently
771   stepwise AF demagnetizing a 200 mT IRM to 290 mT (Dunlop and Ozdemir, 1997). Finally,
772   IRM was acquired stepwise to 886.5 mT and subsequently AF demagnetized to 290 mT. The
773   acquisition and demagnetization of IRM allows for the construction of coercivity spectra (Fig.
774   S16) (Egli, 2003). The hysteresis properties (Section 5.2) and MDF are consistent with a
775   multidomain grain size for 12022 and 15597. Both samples have low Cisowski *R*-values (0.29-
776   0.32), indicating that the extent of magnetostatic interactions between metal grains should be
777   modest.
778
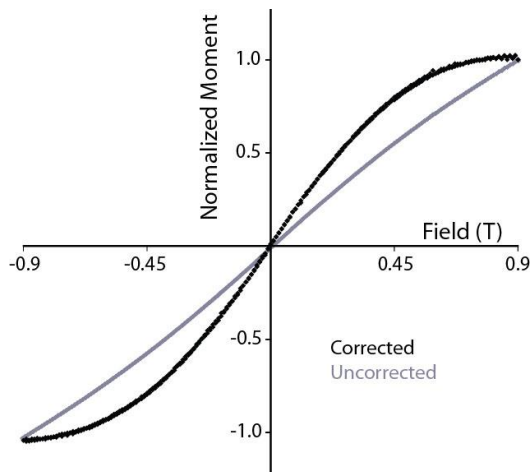
Figure S15. Room temperature hysteresis loop measured for 12022,310a. Shown is normalized sample moment
as a function of applied field. The black curve represents the hysteresis loop after subtraction of paramagnetic
and diamagnetic contributions. The gray curve represents the raw (uncorrected) data.

27
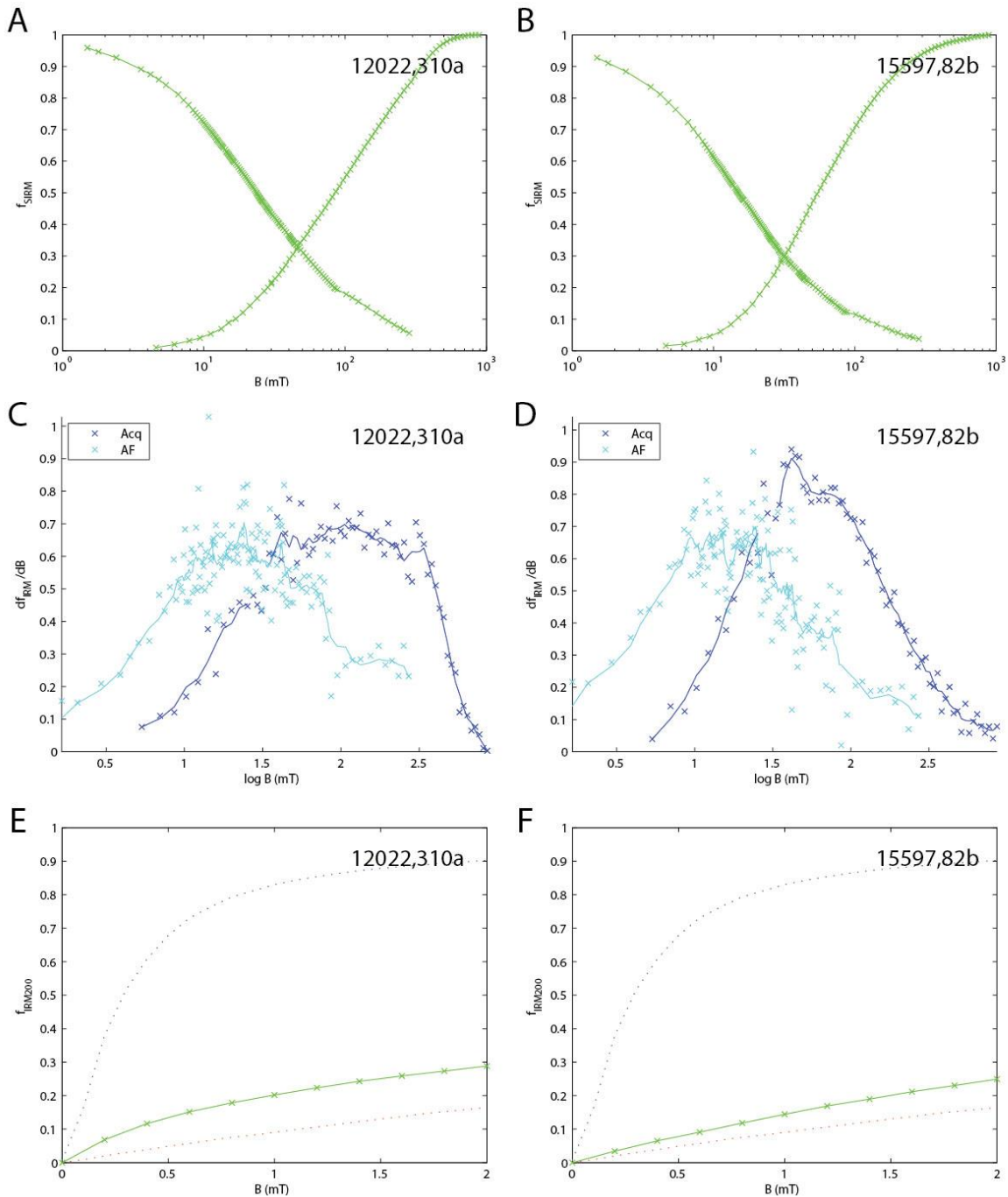
Figure S16. Rock magnetic experiments on 12022 and 15597. Moment normalized IRM acquisition and AF demagnetization curves for (A) 12022,310a and (B) 15597,82b. Coercivity spectra of samples [i.e., derivative of IRM acquisition (dark blue curve) and AF demagnetization of IRM (light blue curve)]: (C) 12022,310a and (D) 15597,82b. ARM acquisition curves for (E) 12022,310a and (F) 15597,82b. ARM was acquired in a 200 mT AC field as a function of DC bias field. Upper dotted curve is that of highly interacting chiton tooth magnetite and lower dotted curve is non-interacting magnetite in magnetotactic bacteria.

5.4. PRM acquisition experiments. It is possible that lunar samples instantaneously acquired SRM as a result of impact shocks in the presence of an ambient magnetic field. Although our petrographic studies of 12022 and 15597 indicate that neither of these samples has experienced

28

782 shocks greater than 5 GPa, shocks at lower pressures do not leave any petrographic evidence but
783 can still produce magnetization [e.g., Gattacceca et al. (2008)]. To rule out sub-5 GPa shock as
784 the source of NRM in our samples, we conducted a series of PRM experiments at CEREGE.
785 Samples were placed in a cylindrical Teflon cavity which was then filled with polyethilsiloxane
786 and placed in a non-magnetic pressure cell similar to that described in Sadykov (2008). A coil
787 surrounding the pressure cell applied a 750 µT DC field. Pressure was applied to the cell using a
788 15 T Specac manual hydraulic press. The sample was kept in-field for at least one minute before
789 the pressure was released. In this study, PRM experiments were conducted for pressures of 0.36,
790 0.72, 1.08, 1.44, and 1.8 GPa. Our procedure is identical to that previously used for lunar
791 samples 10020, 10017, and 10049 (Shea et al., 2012; Suavet et al., 2013).
792
793 As in previous studies of lunar rocks (Gattacceca et al., 2010), we found that
794 predominantly low-coercivity grains (<~20-30 mT) in 12022,310a and 15597,82b acquired
795 PRM. The confinement of PRM to low coercivities also suggests that shock demagnetization
796 processes are unlikely to have fully demagnetized 12022 (assuming PRM acquisition and
797 pressure demagnetization affect the same coercivity range). This is consistent with the pressure
798 demagnetization experiments of Bezaeva et al. (2010). Therefore, any primary TRM the sample
799 may have acquired during formation should have been retained.
800 For both samples, the LC component was more resistant to AF demagnetization than the
801 PRM acquired in our experiments. This effectively rules out SRM as the source of the LC
802 magnetizations in our samples. For undemagnetized (total) PRM, we observed a roughly linear
803 relationship between the acquired PRM intensity and pressure. For PRM after demagnetization
804 to the AF field representing the end of the LC component (80 mT for 12022,310a and 60 mT for
805 15597,82b) (Fig. S17), a roughly concave-down relationship is observed. Following Shea et al.
806 (2012), and assuming a linear relationship between demagnetized PRM and pressure, we can
807 estimate an upper limit on the intensity of a 5 GPa PRM acquired in a 750 µT field and place an
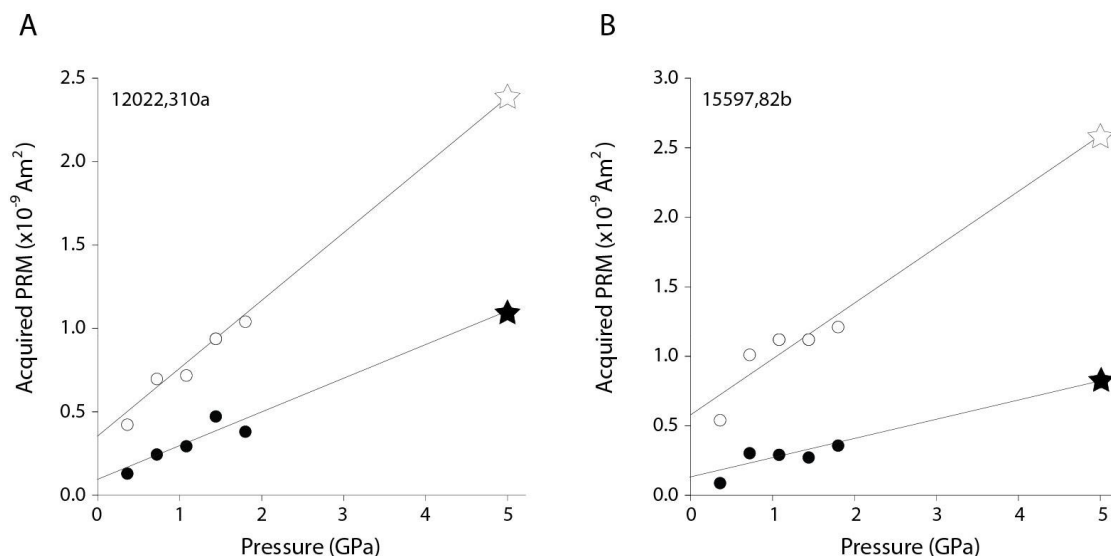
Figure S17. PRM acquisition of subsamples (A) 12022,310a and (B) 15597,82b. Shown is the PRM intensity as a function of applied pressure (0.36, 0.72, 1.08, 1.44, and 1.8 GPa) acquired in a 0.75 mT field. Empty circles are PRM normalized by the AF 0 mT step and filled circles are normalized by the AF 4 mT and AF 6 mT steps for subsamples 12022,310a and 15597,82b, respectively. Solid lines are best fit linear regression to data. Extrapolation yields a maximum estimate of the PRM acquired at 5 GPa (stars).

29

808 upper limit on the fraction of such a PRM remaining after demagnetization to an AF level
809 equivalent to the end of the LC component (stars in Fig. S17). This then allows us to calculate
810 the paleofield intensity that would have been necessary to produce the observed MC components
811 assuming they are SRM produced by a 5 GPa shock (Shea et al., 2012; Suavet et al., 2013). We
812 find that 336 μT and 242 μT fields would be required to reproduce the MC1 components of
813 12022,310a and 15597,82b, respectively. Both of these values are higher than estimates for a
814 lunar dynamo field, although it is possible that transient impact-generated fields could reach such
815 intensities, [e.g., Crawford and Schultz (1999)]. However, the non-unidirectionality of the MC
816 components within samples 12022 and 15597 provides evidence against an SRM origin.

817

818 *5.5. VRM acquisition experiments.* As discussed in Section 3, another possible source of the
819 magnetization in our samples is VRM acquired as the sample was exposed to the terrestrial
820 magnetic field at ambient temperatures for 41 years prior to our study. To assess the possible
821 contribution of VRM to the NRM of our samples, we conducted laboratory VRM acquisition
822 experiments on subsamples 12022,308b and 15597,82a. In these experiments, the samples were
823 placed in the Earth's field in a fixed position for 6 days 3 hours and 50 min (for 12022,308b) and
824 12 days 14 hours and 23 min (for 15597,82a). After exposure to the terrestrial field, each
825 subsample was returned to our magnetically shielded room, and after a ~1 minute delay,
826 subsample magnetizations were repeatedly measured to determine the intensity of the acquired
827 VRM and its decay rate with time (Fig. S18).
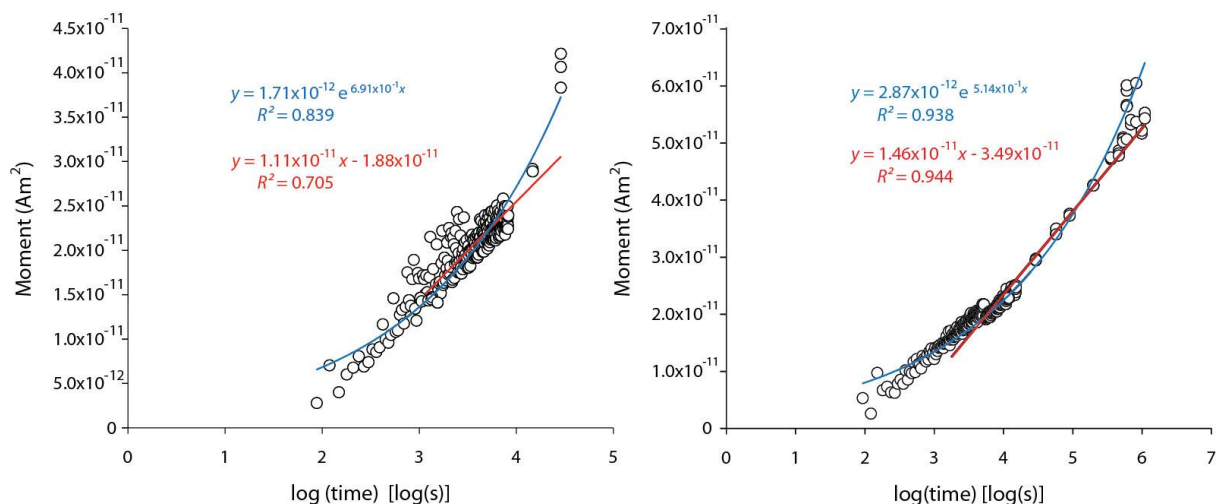
Figure S18. VRM decay experiments on samples 12022 and 15597. Samples were stored for 1-3 weeks in the terrestrial field (~50 μT) and then returned to our shielded room (< 200 nT) where their moments were semi-continuously measured (white circles). All of the data can be fit well with exponential curves (blue curves) for the moment. Equations for these fits are shown on plot with *y* representing the ordinate and *x* the intercept. Later time data can be fit with lines (red lines). (A) 12022,308b, (B) 15597,82a.

828 We found that VRM components of magnitude 8.13×10^{-11} and 3.06×10^{-10} Am^2
829 (equivalent to 11% and 160% of the initial NRM) were acquired during our experiments on
830 12022,308b and 15597,82a, respectively. As observed in prior studies (Weiss et al., 2008; Yu
831 and Tauxe, 2006), the decay rate of VRM was only approximately linear with log(time),
832 indicating that is not possible to unambiguously compute a magnetic viscosity decay coefficient

833   S_d = d(VRM lost)/d[log(time)]. Although we cannot precisely determine the VRM acquisition
834   and decay rate over 40 years without an equivalently-long experiment, we can extrapolate linear
835   and exponential fits to our weeks-long experimental data to estimate bounds on this. For sample
836   12022,308b, our linear fit (red lines in Fig. S22) predicts that the total VRM resulting from 40
837   years of exposure to the Earth's field [log(time) = 9.1 log(s)] followed by nearly a year of
838   viscous decay in our magnetically shielded room prior to our first NRM measurements
839   [log(time) = 7.5 log(s)] to be ~2.5% of the observed NRM for this sample. Alternatively, an
840   exponential fit (blue lines in Fig. S22) would predict that ~85% of the observed NRM could be a
841   VRM. A VRM origin for the LC/LT (and possibly the MC1/MT1) components in 12022 is
842   consistent with long-term storage of blocks 310, 308, and 305 in differing orientations in the
843   terrestrial field. This is because component directions were unidirectional within parent blocks,
844   but non-unidirectional when comparing parent blocks to each other (main text Fig. 2). It is less
845   likely that VRM can be the source of the MC2/MT2 because (*i*) neither our linear nor
846   exponential fits suggested that VRM could explain 100% of the magnetization in the sample and
847   (*ii*) the unblocking temperatures of the MT2 component are probably too high (Section 3.4.2.3).
848   For sample 15597,82a, our linear fit predicts that VRM could account for ~9.9% of the observed
849   NRM for this sample [using log(time) = 9.1 log(s) for VRM acquisition and log(time) = 7.4
850   log(s) for decay in our shielded room prior to our first NRM measurements]. Our exponential fit
851   predicted that ~340% of the observed NRM in that subsample could be a VRM. While VRM is
852   in principle capable of reproducing the NRM magnitude of 15597, the non-unidirectionality of
853   the LC and MC magnetizations across subsamples challenges the hypothesis that VRM is the
854   source of the LC component in that sample. However, as discussed in Section 3.6,
855   heterogeneous acquisition of VRM across the sample may explain this discrepancy.

857   *5.6. Thermal demagnetization of ARM and IRM.* To determine the peak demagnetization
858   temperature as an indicator of ferromagnetic mineralogy, we conducted stepwise thermal
859   demagnetization of an ARM (0.1 mT dc bias field) imparted on subsample 305d and a 900 mT
860   IRM imparted on subsample 308 (Fig. S19). Nearly all of the ARM and 90% of the IRM were
861   removed by 600°C. We attribute this to the transformation of martensite to taenite upon reaching
862   the austenite start temperatures: the experiments summarized in Swartzendruber et al. (1991)
863   suggest that the austenite-start temperatures should range between 580-740°C for the range of
864   observed compositions.   The fact that ~10% of the IRM remained after 600°C suggests that, in
865   addition to martensite, kamacite is also present in the sample. This is consistent with a previous
866   thermomagnetic study (which observed magnetization persisting until 780°C) (Helsley, 1971)
867   and our compositional measurements (Section 2.2).

869   *5.7. Magnetic anisotropy.* High magnetic anisotropy could bias our paleointensities and
870   paleointensity fidelity tests (see Section 4 of main text). To test for this, we conducted ARM and
871   IRM remanence anisotropy experiments on 12022,310a and 15597,82b following Shea et al.
872   (2012) and Suavet et al. (2013). ARM (DC field of 0.2 mT and AC field of 85 mT) and IRM (20
873   mT field) were applied along all three orthogonal axes. We solved for the principal axes of the
874   anisotropy ellipsoids following Stephenson et al. (1986). Following Selkin et al. (2000), we also
875   calculated anisotropy-corrected paleointensities applied along the *z*-axis (as was applied in our
876   paleointensity fidelity experiments) and found that the anisotropy of neither 12022 nor 15597
877   was sufficient to affect our paleointensity determinations.

878   For 12022,310a, degree of anisotropy values, P, ranged from 1.16 to 1.27 and shape
879 factor values, T, ranged from -0.43 to -0.69, indicating a prolate anisotropy ellipsoid.
880 Anisotropy-corrected paleointensities for this ellipsoid are within 1% of any uncorrected
881 paleointensity value. For 15597,82b, P ranged from 1.17 to 1.26 and T ranged from 0.19 to 0.73,
882 indicating an oblate anisotropy ellipsoid. Anisotropy-corrected paleointensities from this
883 ellipsoid are also within 1% of any uncorrected paleointensity value.

884
885
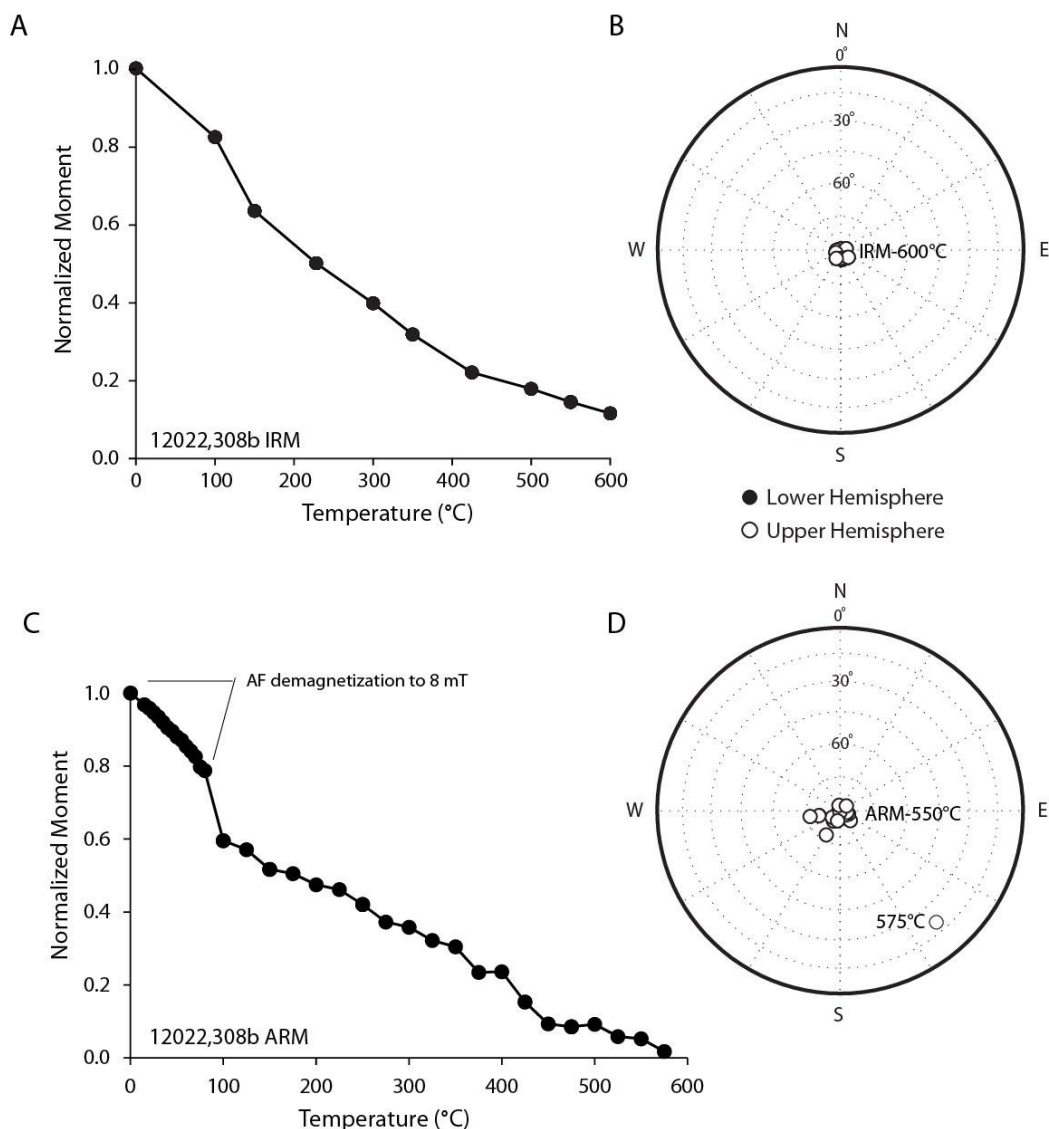
Figure S19. Thermal demagnetization of laboratory saturation IRM (A, B) and 0.1 mT ARM (C, D) for 12022.
(A, C) Normalized moment vs. temperature step. Note in part (C) that the ARM was pre-treated with AF
demagnetization to 8 mT prior to thermal demagnetization. (B, D) Equal area stereographic projections of the
thermal demagnetizations. Open circles (dashed lines) represent directions in the upper hemisphere, while filled
circles (solid lines) represent directions in the lower hemisphere. Selected temperature steps are labeled.

886
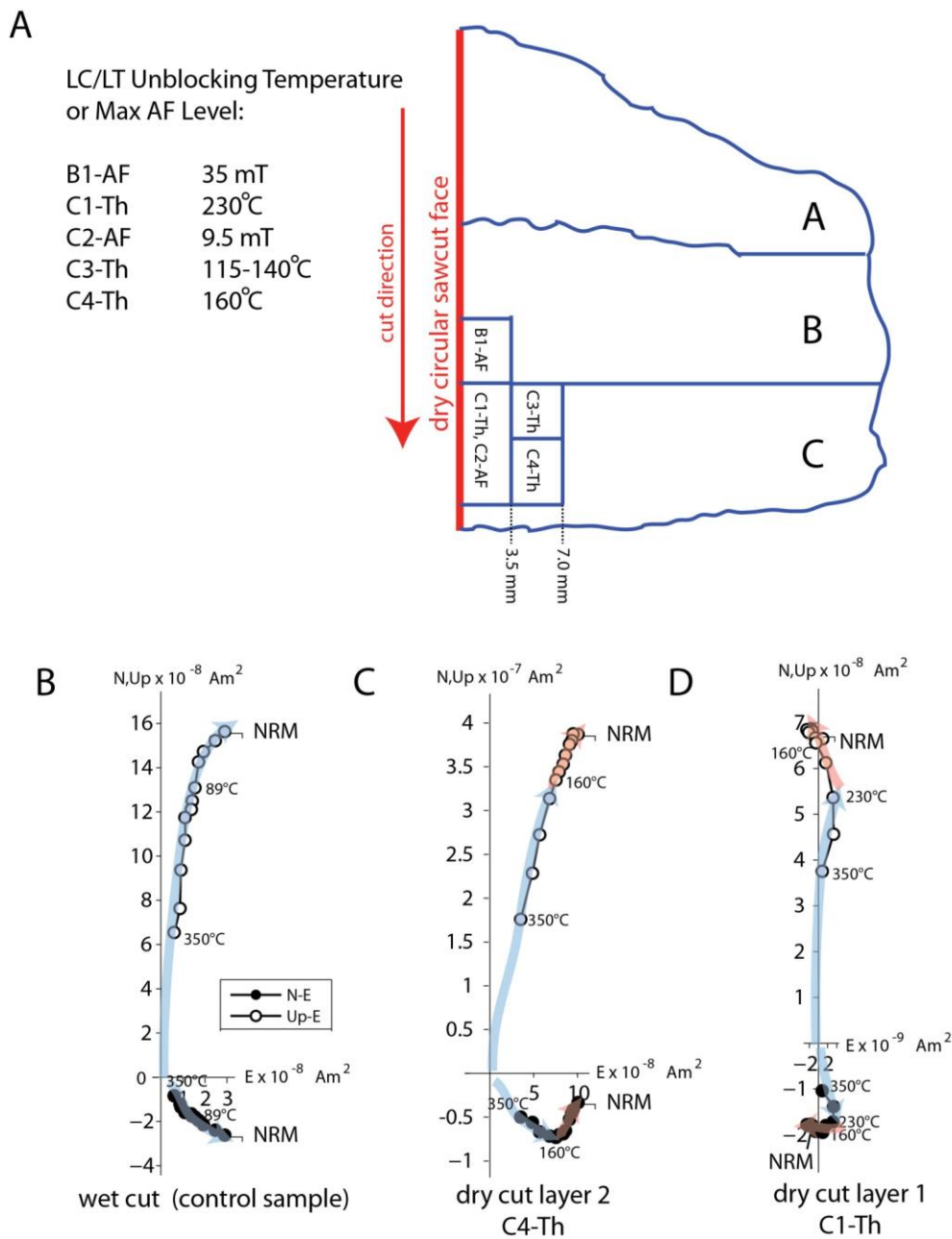
Figure S20. Schematic and data for terrestrial andesite dry saw cutting experiment. (A) Diagram of saw cut rock and locations of individual subsamples analyzed. Part A also contains a table of sample names (which denote whether AF or thermal demagnetization was conducted) and the maximum AF level or unblocking temperature that the secondary saw cut component persisted to. (B) Thermal demagnetization of a control subsample that did not undergo dry cutting. (C) Thermal demagnetization of a subsample taken from 3.5 mm away from the saw cut face. (D) Thermal demagnetization of a subsample directly collected from the saw cut face. Blue arrows denote the primary component. Red arrows denote the overprinting component.

6. Saw cutting experiment on a terrestrial rock

To experimentally test the hypothesis that dry-saw-cutting at JSC imparted a pTRM onto 12022, we dry-cut a terrestrial, magnetite-bearing andesite under similar conditions at MIT. The sample was 10 cm in diameter (approximately the same size as the lunar rocks cut at JSC) and hysteresis

33

892 measurements showed that it had a mean pseudo-single domain grain size. We used a modified
893 MK Diamond 101 circular tile saw equipped with the same size (10 inch) blade and cutting
894 speed of ~1000 revolutions per minute as was used on the Apollo 12 samples. Our modern saw
895 cut through the terrestrial andesite in approximately two minutes (~10 times faster than it took to
896 cut similarly sized lunar basalts in 1970) without any of the failures similar observed during the
897 Apollo era. We posit that due to advances in saw blade and saw manufacturing technology,
898 modern saw blades do not overheat and fail as readily as saw blades did in 1970. Approximately
899 5 seconds after the cut was finished (once the spinning blade slowed to a halt), an infrared
900 thermometer measured the temperature at the edge of the saw cut blade to be ~80°C. However,
901 the spinning blade had likely experienced a great deal of air cooling by this point. Based on this
902 experiment, we initially assumed that a lower limit temperature associated with dry saw cutting
903 would have been at least 80°C.

904 We subjected five subsamples from the vicinity of the saw cut face (either directly from
905 the face or 3.5 mm away) to stepwise AF or thermal demagnetization, as well as one control AF
906 sample and one control thermal sample collected prior to dry saw cutting. Our control samples
907 were dominated by one magnetic component that persisted up to at least 85 mT and 350°C (the
908 maximum AF levels and temperature steps used). All samples at or near the dry-cutting face
909 acquired a secondary magnetization component (Fig. S20). In two AF demagnetized subsamples
910 from directly on the saw cut face, this LC component was removed by 9.5 and 35 mT,
911 respectively. The subsample from directly on the saw cut face had its LT component removed
912 by 230°C, while those 3.5 mm deep from the saw cut face had this component removed by 115-
913 140°C and 160°C, respectively. Fluctuations in the AF level and temperature needed to remove
914 the component from different regions in the sample suggest that the rock experienced uneven
915 heating from saw cutting.

916 In total, our results indicate that pTRM magnetization components may be acquired as a
917 result of saw cutting blocked to temperatures of potentially a few hundred °C. Caution should be
918 used in the interpretation of magnetic remanence in samples obtained from the saw cut faces of
919 dry cut samples.

920
921
922
923 **7. ^{40}Ar/^{39}Ar and ^{38}Ar/^{37}Ar thermochronology**
924
925 *7.1. Analytical results.* We conducted stepwise degassing ^{40}Ar/^{39}Ar and ^{38}Ar/^{37}Ar
926 thermochronometry on one 3.2 mg whole-rock aliquot of sample 12022 at the Berkeley
927 Geochronology Center using procedures described in Cassata et al. (2009), Shea et al. (2012),
928 and Shuster et al. (2010) . We provide the complete dataset of stepwise Ar release and extraction
929 temperatures in Table S13; we report the apparent ^{40}Ar/^{39}Ar age of each degassing step (Fig.
930 S21a) relative to the Hb3gr neutron fluence monitor (age = 1081 Ma) and use the monitor age
931 and decay constants of Renne et al. (2011) and Ar isotopic abundances of Steiger and Jager
932 (1977). We also report the apparent cosmogenic ^{38}Ar exposure age of each degassing step (Fig.
933 S21b), calculated from the observed ^{38}Ar/^{37}Ar ratio and using the procedures described in
934 Cassata et al. (2010), Shea et al. (2012), and Suavet et al. (2013). To deconvolve the cosmogenic
935 Ar derived from K-glass and plagioclase, we assume phase-specific production rates of ^{38}Ar
936 (Table S14) based on the apparent K/Ca and Fe/Ca estimated in each phase following procedures
937 described in Suavet et al. (2013).

34

938

939

940   The ^{40}Ar/^{39}Ar age spectrum (Fig. S21b) has relatively low apparent ^{40}Ar/^{39}Ar ages in the

941   first 11 degassing steps (comprising the initial ~50% of ^{39}Ar released from K-glass and

942   plagioclase), that systematically increase from an initial step age of ~1125 Ma up to plateau ages

943   between 3145 and 3225 Ma observed in the subsequent 7 degassing steps (i.e., the final ~50% of

944   total ^{39}Ar). The age spectra were normalized to the total gas released in extractions 1-22 of 26,

945   which reflects Ar derived from K-glass and plagioclase. Higher temperature extractions are

946   dominated by gas released from pyroxenes as distinguished by their ^{37}Ar$_{Ca}$/^{39}Ar$_K$ ratio. The 7
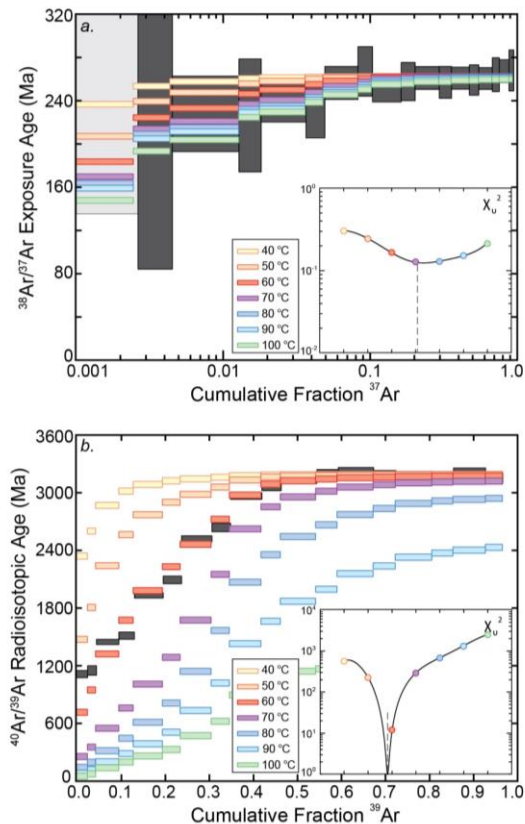
Figure S21. The predicted effects of 263 Ma of solar heating at the lunar surface, calculated using the 12022 MP-MDD model. (A) The production and diffusion of ^{38}Ar$_{cos}$. The observed exposure ages ± 1 standard deviation (gray boxes) are plotted against the cumulative release fraction of ^{37}Ar released (note the log scale). To minimize the influence of edge effects, the light gray boxes in each panel were excluded from the fit statistic calculation. The colored steps are model release spectra calculated using the MP- MDD model parameters and ^{38}Ar$_{cos}$ production rates shown in Table S14. For the diffusion of ^{38}Ar$_{cos}$ 12022 was subjected to various constant effective daytime temperatures ranging from 50 to 110°C during the last 263 Ma. ^{38}Ar$_{cos}$ is produced continuously over this duration, while diffusion occurs only over half of this period during elevated daytime temperatures. The reduced chi squared fit statistic for each model is shown in the inset, identifying ~73.4 °C as the best-fit effective mean temperature. (B) The diffusion of ^{40}Ar* due to solar heating, calculated assuming the crystallization age is 3.19 Ga [symbols and model parameters are the same as (A)]. The models include complete retention (i.e., no diffusion) of ^{40}Ar between the plateau age of the sample (3194 ± 12 Ma) and the apparent ^{38}Ar surface exposure age (262.7 ± 4.9 Ma), followed by both production and diffusion at a constant daytime temperature since the rock was exposed at the lunar surface.

947 concordant step ages correspond to a plateau age of 3194 ± 12 (one standard deviation analytical
948 uncertainty; ± 25 Ma when uncertainties in the decay constant and age of the fluence monitor are
949 included; Table S15). The apparent ^{38}Ar exposure age spectrum [Fig. S21a; see Suavet et al.
950 (2013) for calculation details] has relatively low exposure ages in the first 5 degassing steps
951 (comprising the initial ~5% of total ^{37}Ar released), that systematically increase from an initial
952 exposure age of ~200 Ma to concordant ages between 260 and 270 Ma observed in the
953 subsequent 12 steps (~93% of the extracted ^{37}Ar). These steps correspond to a weighted mean
954 ^{38}Ar exposure age of 262.7 ± 4.9 Ma (Table S15) under the assumption that all cosmogenic ^{38}Ar
955 was produced at the lunar surface.
956
957 *7.2. Thermochronological modeling results.* We calculated apparent diffusion coefficients for
958 ^{39}Ar and ^{37}Ar from the whole-rock stepwise release data (Table S13) following Fechtig and
959 Kalbitzer (1966) and procedures described in Cassata et al. (2010), Shea et al. (2012), and Suavet
960 et al. (2013). Results of these calculations are shown, along with controlled temperatures of each
961 heating step, as an Arrhenius plot in Fig. S22. Because we analyzed a whole-rock aliquot, the
962 neutron-induced ^{39}Ar and ^{37}Ar was released from multiple phases (i.e., K-glass, plagioclase, and
963 pyroxene), which each contain a range of crystal and/or diffusion domain sizes. To quantify the
964 diffusion of radiogenic ^{40}Ar and cosmogenic ^{38}Ar from the sample for various model thermal
965 scenarios, we therefore construct a multi-phase, multi-domain diffusion (MP-MDD) model fit to
966 the data shown in Fig. S22, following the procedure described in Shea et al. (2012). The MP-
967 MDD model parameters are summarized in Table S14. Additional descriptions of MDD-type
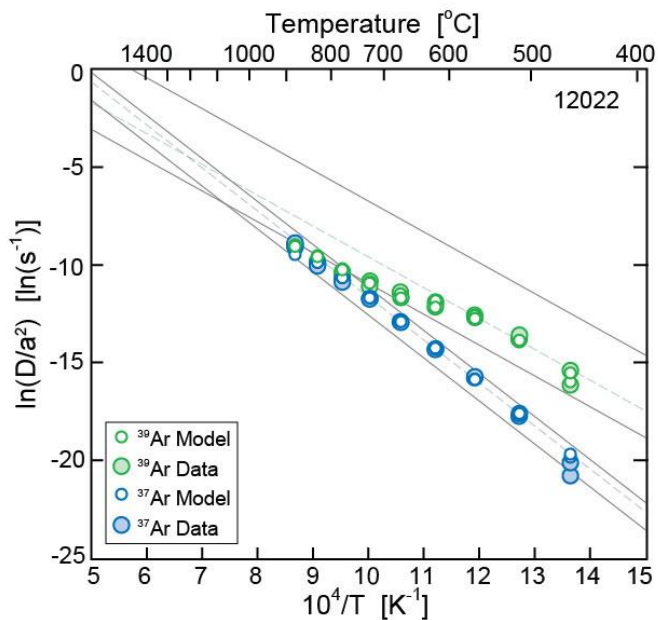
Figure S22.   Arrhenius plots with calculated diffusion coefficients for ^{39}Ar (large green symbols) and ^{37}Ar (large blue symbols) shown alongside the MP-MDD models (small white symbols) fit to the ^{39}Ar and ^{37}Ar data using our laboratory heating schedule and the 4 specified domain sizes and gas fractions listed in Table S14. Each temperature step was run twice. The grey lines indicate the input diffusion kinetics of each of the four model domains. The colored, dashed lines indicate linear regressions to extractions that yielded reproducible calculated values of D/a^2 at a given temperature, which were used to constrain the E_a for Ar diffusion in K-glass (^{39}Ar steps 2-6) and plagioclase (^{37}Ar steps 3-12).

36

968   models and their applications to samples with multiple K-bearing phases can be found in Lovera
969   et al. (1991), Cassata et al. (2010), Shea et al. (2012), and Suavet et al. (2013).

970   Discordance observed in the radiogenic and exposure age spectra is indicative of
971   thermally activated diffusive loss of ^{40}Ar* and ^{38}Ar$_{cos}$. Previous work on similar mare basalts has
972   shown such discordance results from diffusive loss associated with heating due to burial in an
973   impact ejecta blanket and/or daytime heating at or near the lunar surface (Shea et al., 2012;
974   Suavet et al., 2013; Turner, 1971). Below we explore time-temperature conditions required to
975   reproduce the observed age spectra for these heating scenarios.

976

977   *7.2.1. Daytime heating at or near the lunar surface.* In Fig. S21, we show model age spectra
978   resulting from the simultaneous production and diffusive loss of ^{40}Ar* and ^{38}Ar$_{cos}$ due to daytime
979   heating for 262.7 ± 4.9 Ma (the exposure age of 12022), calculated using our MP-MDD
980   parameters (Table S14) following procedures described in Shea et al. (2012) and Suavet et al.
981   (2013). The exposure and radioisotopic age spectra discordance is best explained by daytime
982   heating at an effective mean (i.e., square-pulse) temperature of ~60-70°C (Fig. S21). This
983   temperature corresponds to a peak temperature during the lunation cycle of ~80-90°C [see
984   Roelof (1968) for details regarding the lunation cycle and see Shea et al. (2012), Suavet et al.
985   (2013), Tremblay et al. (2014), and Turner (1971) for details regarding the relationship between
986   the effective mean temperature, peak temperature, and activation energy of the degassing phase
987   (i.e., K-glass)]. These temperatures significantly underestimate daily peak temperatures at the
988   Apollo 12 landing site [~110-115°C (Bauch et al., 2009; Huang, 2008)], which indicates that
989   12022 was shallowly buried in the regolith or shadowed by a nearby boulder for much of its near
990   surface exposure history (such that it was partially buffered from surface temperature
991   fluctuations but sufficiently shallow to accumulate cosmogenic nuclides).

992   Because 12022 was sampled from the exposed face of an ejecta mound, it has clearly
993   been subjected to daily surface temperature fluctuations for at least its most recent exposure
994   history. In Fig. S23, we show model age spectra resulting from various durations of exposure to
995   daytime heating at an effective mean temperature of 95°C, which corresponds to a peak
996   temperature of ~115°C (the daily maximum temperature at the Apollo 12 landing site). The age
997   spectrum discordance is best explained by heating at the lunar surface for 3 Ma, which indicates
998   that 12022 was only recently exposed at the surface. Measurements of cosmogenic Xe isotopes
999   in 12022 (Bogard et al., 1971) provide additional support for shallow burial throughout its near-
1000   surface exposure history. Assuming a regolith density of 2.0 g cm^{-3}, the inferred burial depth of
1001   12022, calculated according to Burnett et al. (1975) based on the measured ^{131}Xe/^{126}Xe ratio, is
1002   40 cm (greater burial depths would be calculated if a two-stage exposure model were
1003   considered). Interestingly, 12022 was sampled ~60 cm beneath the upper surface of the ~1 m
1004   thick ejecta mound mentioned above. It is thus possible that 12022 spent much of its near
1005   surface residence in this ejecta deposit, and was only recently subjected to solar heating due to a
1006   small impact event that exposed the present southeastern surface of the ejecta mound.
1007   Regardless of the exact duration for which 12022 was shallowly buried, discordance observed on
1008   both the radioisotopic and exposure age spectra can be explained by daily temperature variations.
1009   The data are thus consistent with a simple, low-temperature thermal history, and do not require
1010   temperatures in excess of ~110-115°C (i.e., surface temperatures) since the rock crystallized.
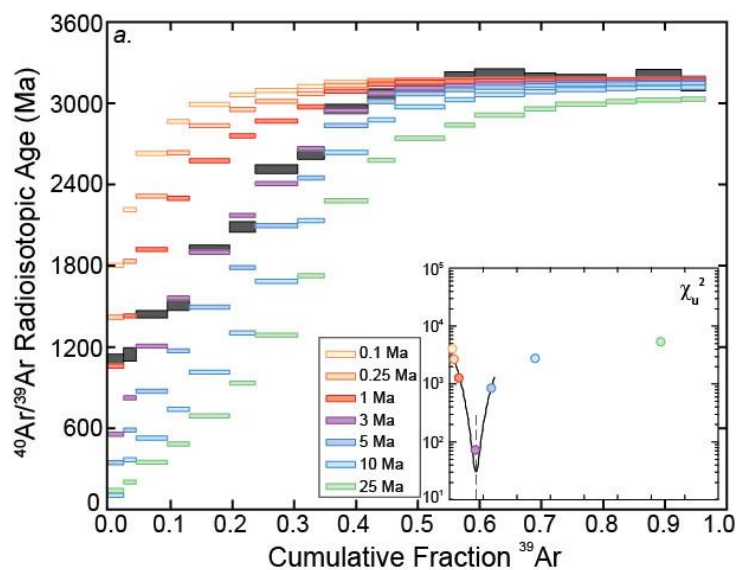
Figure S23. The predicted effects of various durations of daytime heating at an effective mean temperature of 95°C (i.e., solar heating at the Apollo 12 landing site), calculated using the 12022 MP-MDD model. Symbols and model parameters are the same as Fig. S21.

1011

1012 *7.2.2. Heating associated with burial in an ejecta blanket.* Although the data are consistent with
1013 diffusive loss of $^{40}Ar^*$ and $^{38}Ar_{cos}$ during near surface exposure, we cannot *a priori* dismiss the
1014 possibility that diffusive loss occurred during an impact event that ejected 12022 from its
1015 bedrock location. Such an event would not explain discordance observed on the exposure age
1016 spectrum, but it is possible that some diffusive loss of $^{40}Ar^*$ occurred prior to surface heating.
1017 We thus modeled two impact scenarios: (1) an event at 1 Ga (the age spectrum vertical axis
1018 intercept) and (2) an event at 263 Ma (the exposure age). To place conservative upper bounds on
1019 temperatures that could have been reached, we assumed that all of the discordance observed on
1020 the radioisotopic age spectrum occurred as a result of heating in the ejecta blanket. Fig. S24
1021 depicts the duration-temperature (*t-T*) conditions (i.e., square-pulse heating scenarios) that
1022 reproduce the age spectrum during the proposed 1.0 Ga and 263 Ma thermal events. The *t-T*
1023 curves were calculated by finding Dt/a^2 values that yielded the best-fit model age spectra (Fig.
1024 S25). Dt/a^2 values were calculated using the diffusion parameters of the smaller K-glass domain.
1025 The calculation would yield the same results if the diffusion parameters of the larger K-glass
1026 domain were used as both have the same E_a (i.e., the same temperature dependence of diffusion).
1027 Different results would be obtained if Dt/a^2 values were calculated using plagioclase diffusion
1028 parameters, although such an approach is not appropriate as most of the diffusive loss occurs in
1029 the K-glass domains. See Shuster et al. (2010), Shea et al. (2012), and Suavet et al. (2013) for
1030 additional details. These Dt/a^2 values define all possible duration-temperature conditions that
1031 yield equivalent discordance on the age spectrum.
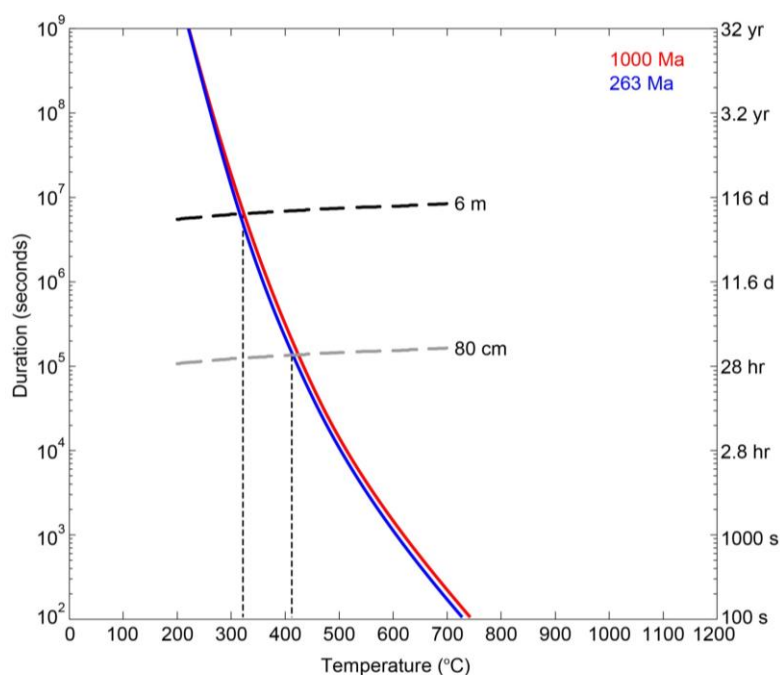
Figure S24. Duration and temperature constraints on potential heating experienced by 12022 in ejecta blankets following impact events. Solid curves are conditions at 1.0 Ga (red) and 263 Ma (blue) that would best predict the observed $^{40}Ar/^{39}Ar$ spectrum. The dashed curves predict the time required to diffusively cool from an initial temperature given by the horizontal axis to <100°C in ejecta blankets of several thicknesses. The intersection of these curves with the solid curves give the peak temperatures that would be experienced by 12022 for the various impact heating scenarios.

1032   Any ejecta blanket in which 12022 was buried prior to its exposure at 263 Ma (i.e.,
1033 during a 1 Ga impact event) must have been sufficiently thick to shield it from cosmic rays (i.e.,
1034 >3 m beneath the surface). The *t-T* curve shown in black in Fig. S24 represents the time *t*
1035 required to diffusively cool a rock from an initial temperature *T* to <100°C in the middle of a 6 m
1036 thick ejecta blanket (i.e., 3 m below the surface), assuming the thermal diffusivity is 10^{-6} m^2s^{-1}.
1037 The intersection of this curve with the *t-T* conditions that reproduce the age spectrum for a 1 Ga
1038 impact event (the red curve) approximates the maximum peak temperature experienced by 12022
1039 (~310°C). Lower peak temperatures are predicted for cooling scenarios involving thicker ejecta
1040 blankets. Any ejecta blanket in which 12022 was buried during the hypothetical 263 Ma ejection
1041 event must have been sufficiently thin such that it was not shielded from cosmic rays (i.e., <3 m
1042 beneath the surface), but sufficiently thick to produce the observed $^{131}Xe/^{126}Xe$ ratio (i.e., >40
1043 cm; see Section 7.2.1). The *t-T* curve shown in gray in Fig. S24 represents the time *t* required to
1044 diffusively cool a rock from an initial temperature *T* to <100 °C in the middle of 80 cm thick
1045 ejecta blankets (i.e., 40 cm below the surface). The intersection of this curve with the *t-T*
1046 conditions that reproduce the age spectrum for a 263 Ma impact event (the blue curve)
1047 approximates the maximum peak temperatures experienced by 12022 (~410°C). The true peak
1048 temperature experienced by 12022 during this hypothetical event would have been lower, as
1049 much, if not all, of the discordance on the age spectrum appears to have resulted from daytime
1050 heating.
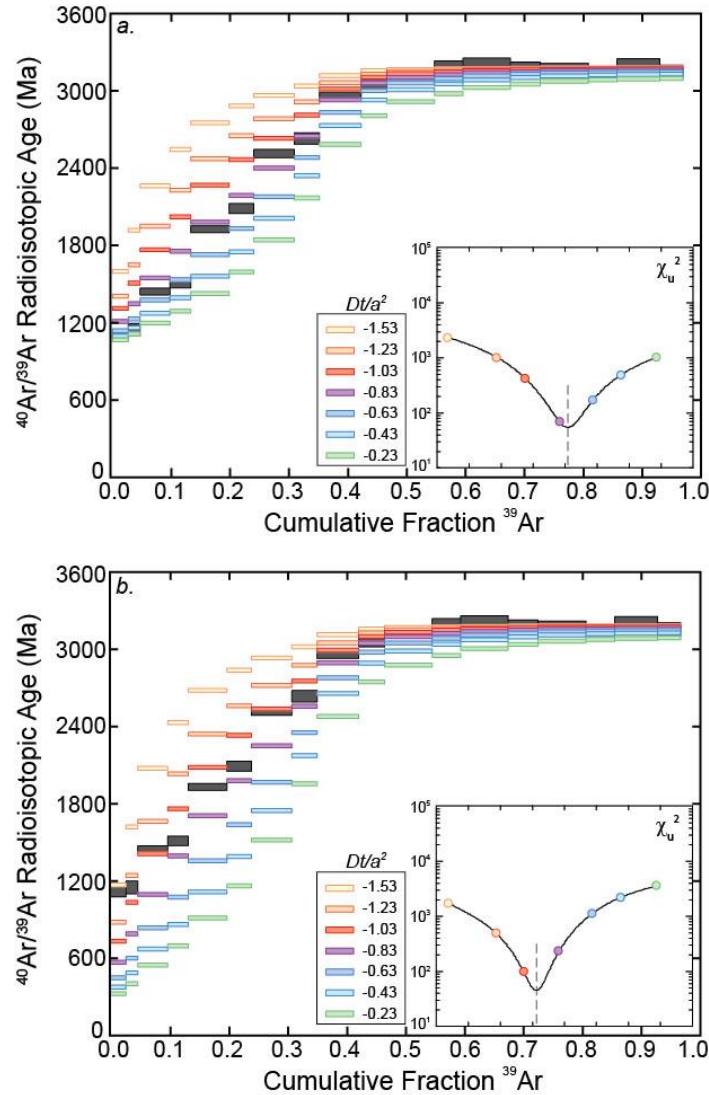
Figure S25. The predicted effects of various square-pulse heating scenarios (i.e., duration-temperature combinations, which are represented as dimensionless Dt/a^2 values), calculated using the 12022 MP-MDD model. Symbols and model parameters are the same as Fig. S21. See text for details regarding the calculation of Dt/a^2 values.

7.2.3. Saw cut heating. We also cannot *a priori* exclude diffusive loss associated with saw-cut heating as an explanation for age spectrum discordance. In Fig. S26, we show model age spectra resulting from 1000 s of heating at various temperatures. The radioisotopic age spectrum discordance is best explained by heating at ~590°C. Higher temperatures would be predicted for shorter durations of saw cut heating and vice-versa. Note that the model assumes that all discordance occurred because of saw cut heating. This assumption is not realistic because it is certain that 12022 was buried in an ejecta blanket at some point during its history and that it also must have experienced diffusive loss from daytime heating on the lunar surface. Because (as discussed in the preceding sections) the age spectrum discordance can fully be explained with a low temperature lunar thermal history, it is unlikely that saw cutting was the dominant source of

1062 diffusive loss of ^{40}Ar* and ^{38}Ar$_{cos}$. Also because the MC1 and MC2 (or the corresponding MT1
1063 and MT2) magnetization components in 12022 do not occupy the entire coercivity spectrum (or
1064 the entire blocking temperature spectrum) of the sample (see Section 4 of main text), it is clear
1065 that the peak saw cutting temperatures were probably well below the 780°C kamacite Curie
1066 temperature and the 600°C mean austenite start temperature and therefore were not high enough
1067 to completely remagnetize the sample.
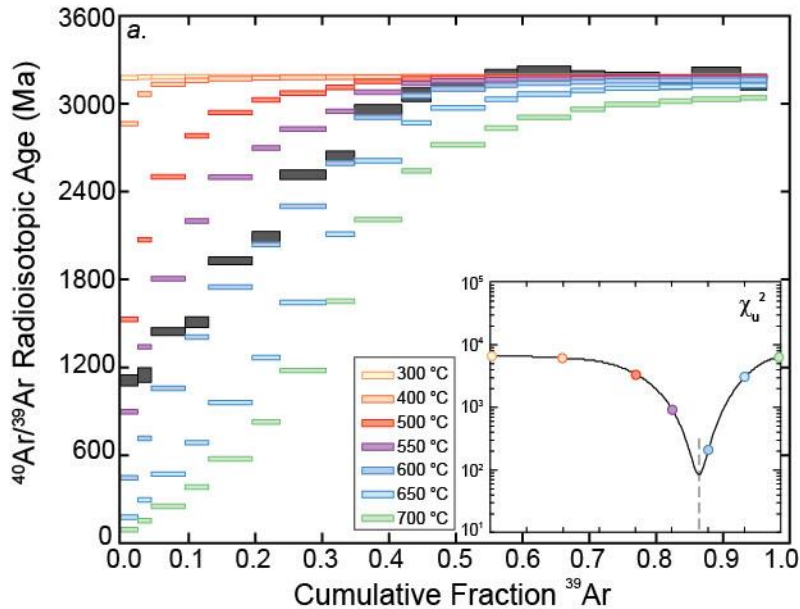
Figure S26.   The predicted effects of heating for 1000 seconds at various temperatures between 300-700°C (potentially reached during saw-cutting), calculated using the 12022 MP-MDD model. Symbols and model parameters are the same as Fig. S21.

1068 *7.2.4. Summary.* Our chronology data and thermal models indicate that the following geologic
1069 history is most probable:

1070   1. Sample 12022 crystallized at 3194 ± 25 Ma, as quantified by the plateau portion of the
1071   age spectrum.
1072   2. After ~3 Ga of quiescence, an impact event brought 12022 to the surface at 262.7 ± 4.9
1073   Ma. Peak temperatures in the ejecta blanket associated with this impact event did not
1074   exceed ~410°C, and were likely much cooler (e.g., 100-200°C).
1075   3. From 262.7 ± 4.9 Ma to the present, daytime heating caused diffusive loss of both ^{40}Ar*
1076   and ^{38}Ar$_{cos}$. Sample 12022 was shallowly buried in the regolith for much of this near
1077   surface exposure history.

1078

8. Implications for the dynamo power source

1080 As mentioned in the main text, three mechanisms have been proposed which are capable of
1081 powering a lunar core dynamo until at least 3.56 Ga: thermal core convection supported by a
1082 wet, heterogeneous mantle (Evans et al., 2013), mechanical stirring driven by mantle precession

1083　(Dwyer et al., 2011) (Tian et al., 2014a), and thermochemical convection driven by inner core
1084　crystallization (Laneuville et al., 2014; Soderlund et al., 2013; Zhang et al., 2013). In this
1085　section, we explore the possibility that the inferred precipitous drop in lunar paleointensities
1086　between 3.56 and 3.19 Ga could reflect the cessation of dynamo generated by at least one of
1087　these mechanisms.

1088　　　　Depending on factors such as core radius, mantle water content, and adiabatic threshold,
1089　thermal evolution models suggest that a thermal convection dynamo could cease sometime
1090　during this period [e.g., Evans et al. (2013)]. As discussed in the main text, a thermochemical
1091　dynamo could have persisted until well beyond 2 Ga, although conversion from bottom-up to
1092　top-down core crystallization could cause the dynamo to shut off earlier than this (Laneuville et
1093　al., 2014). Dwyer et al. (2011) suggest that the cessation time for a mantle precession dynamo
1094　largely depends on two factors: the adiabatic threshold (P_{th}) used and the semimajor axis to time
1095　(*a-t*) relationship of the lunar orbit evolution. Because the authors only utilized one P_{th} value
1096　(4.7×10^9 W), we explored a larger parameter space for P_{th} and *a-t* to determine whether a
1097　precession dynamo might be expected to cease between 3.56 and 3.19 Ga. Following Dwyer et
1098　al., we assigned dynamo cessation to the time when the total power drops below P_{th}. However,
1099　we note that mechanical forcing of core fluids may allow a precession-driven dynamo to operate
1100　subadiabatically.

1101　　　　P_{th} for the Moon is poorly constrained. From Dwyer et al. (2011):
1102

$$P_{\text{th}} = \frac{16\pi^2 k_c R_{cm}^3 \alpha_c G \rho_c T_c}{3 C_{P,c}}$$

1103

1104　where k_c is the core thermal conductivity, R_{cm} is the radius of the core-mantle boundary, α_c is
1105　the coefficient of linear thermal expansion for the core, G is the gravitational constant, ρ_c is the
1106　core density, T_c is the core temperature, and $C_{P,c}$ is the core heat capacity. Estimates for each of
1107　these parameters vary: k_c may range between 30 and 90 W m^{-1} K^{-1} (de Koker et al., 2012; Dwyer
1108　et al., 2011; Gomi et al., 2013), R_c between 2×10^5 and 4×10^5 m (Hood et al., 1999; Konopliv et
1109　al., 1998; Shimizu et al., 2013), α_c between 5.85×10^{-5} and 1×10^{-4} K^{-1} (Stegman et al., 2003;
1110　Williams and Nimmo, 2004), and ρ_c between 5.2×10^3 and 7.5×10^3 kg m^{-3} (Dwyer et al., 2011;
1111　Williams et al., 2009). We assume T_c = 1500 K and $C_{P,c}$ = 780 J kg^{-1} K^{-1} following Dwyer et al.

1112　　　　Inputting these values into the above equation, we determined maximum (3×10^{10} W) and
1113　minimum (5×10^8 W) values for P_{th}. According to Fig. 1 of Dwyer et al. (2011), these values
1114　would result in dynamo cessation at Earth-Moon separation distances between ~45-55 Earth
1115　radii. The end-member *a-t* relationships from Walker et al. (1983) [see Fig. S2 of Dwyer et al.
1116　(2011)] suggest that these Earth-Moon separation distances would correspond to dates between
1117　~3.55 Ga and ~0.6 Ga. Therefore, consideration of certain end-member parameters may permit
1118　cessation of a precession dynamo sometime between 3.56 and 3.19 Ga (Table S16). This is
1119　consistent with recent magnetohydrodynamic simulations which find that a precession dynamo
1120　would have ceased during this period for typical orbital evolution models when the mantle
1121　obliquity decreased below a critical threshold (Tian et al., 2014a; Tian et al., 2014b).
1122

Table S1. Elemental abundances of 12022 and 15597 metal grains measured by wavelength dispersive spectroscopy.

Sample	#	Al	Si	Fe	Ni	W	Ti	Cr	P	S	Co	Total
12022												
,114	2	0.02	0.03	93.59	5.06	0.00	0.22	0.96				99.89
,114	4	0.08	0.05	78.89	18.67	0.01	0.26	0.63				98.59
,114	5	0.02	0.03	89.48	8.90	0.02	0.15	0.48				99.09
,114	6	0.04	0.03	93.24	6.87	0.00	0.08	0.28				100.54
,114	7T1			89.42	7.59		0.27	1.12				98.40
,114	7T2			86.38	10.28		0.12	0.40				97.18
,114	7T3			86.98	10.30		0.11	0.18				97.56
,114	7T4			90.26	6.87		0.09	0.10				97.32
,114	7T5			88.56	9.13		0.07	0.04				97.81
,114	8T1			92.33	5.62		0.13	0.40				98.49
,114	8T2			92.62	5.15		0.18	0.61				98.56
,114	8T3			91.16	5.90		0.31	0.76				98.13
,308c*	9T1	0.01	0.03	90.85	7.58		0.14	0.55	0.01	0.02	2.41	102.00
,308c*	9T2	0.00	0.07	87.90	7.51		0.11	0.58	0.00	0.02	2.32	100.85
,308c*	10T1	0.01	0.03	91.88	7.00		0.17	0.67	0.01	0.26	2.36	102.43
,308c*	10T2	0.00	0.01	89.83	7.02		0.20	0.95	0.00	0.00	2.33	100.85
,308c*	10T3	0.02	0.04	87.65	8.20		0.21	1.13	0.02	0.03	2.64	100.88
,308c*	10T4	0.03	0.09	81.40	12.08		0.21	1.20	0.03	0.03	2.44	98.81
,308c*	10T5	0.02	0.07	74.48	18.91		0.18	0.74	0.01	0.02	1.54	96.64
,308c*	11T1	0.22	0.06	79.42	15.36		0.46	0.63	0.03	0.03	2.04	99.59
,308c*	11T2	0.01	0.03	81.92	16.08		0.62	0.64	0.01	0.01	2.20	102.13
,308c*	11T3	0.02	0.04	81.02	15.92		0.70	0.72	0.01	0.02	2.13	100.99
15597												
,13	1	0.06	0.02	90.97	7.37	0.00	0.10	0.00				98.53
,13	2	0.04	0.04	94.62	4.35	0.02	0.05	0.08				99.20
,13	3	0.05	0.04	91.83	7.16	0.00	0.09	0.00				99.17
,13	4	0.05	0.05	96.67	1.84	0.01	0.12	0.57				99.32
,13	5	0.05	0.02	93.02	6.24	0.00	0.09	0.03				99.44
,13	6	0.22	0.04	94.38	4.07	0.00	0.05	0.05				98.80
,13	7	0.04	0.03	91.72	6.78	0.02	0.10	0.01				98.70
,13	8T1			94.31	2.33		0.22	0.45				97.31
,13	8T2			95.72	2.39		0.09	0.53				98.73
,13	9T1			92.72	4.81		0.11	0.97				98.61

Sample	Grain	Al	Si	Fe	Ni	W	Ti	Cr	P	S	Co	Sum
,13	9T2			91.81	4.62		0.08	0.96				97.48
,82e*	10T1*	0.02	0.03	92.93	6.09		0.01	0.07	0.07	0.01	1.40	100.94
,82e*	10T2*	0.02	0.02	91.31	7.13		0.07	0.02	0.06	0.02	1.40	100.19
,82e*	10T3*	0.01	0.03	92.20	5.71		0.06	0.01	0.08	0.01	1.39	99.64
,82e*	11T1*	0.00	0.03	82.51	11.35		0.01	0.04	0.03	0.03	1.28	98.66
,82e*	11T2*	0.03	0.04	84.82	12.58		0.03	0.00	0.02	0.01	1.33	99.26

Note: The first column contains the sample name. Asterisks (*) denote points measured from nital-etched thick sections 12022,308c. The second column contains a number corresponding to the grain measured if there was only one data point per grain or the transect measured across a single grain if multiple points were measured (when number is preceded by a "T"). The third through twelfth columns contain the elemental abundances in mass percent for Al, Si, Fe, Ni, W, Ti, Cr, P, S and Co, respectively. The thirteenth column contains the sum (in percent) of the measured elemental abundances.

Table S2. NRM components identified for subsamples of 12022 and 15597.

Sample, Component	Mass (mg)	AF (mT) or Temperature Range (°C)	Type	Dec. (°)	Inc. (°)	MAD (°)	DANG (°)	Passes DANG-MAD test?	N
12022,310a	144								
LC		NRM-4.0	L	272.4	-77.4	9.3			7
MC1		4.0-85.0	AL	139.8	-20.6	11.7/15.4	14.9	Yes	103
12022,310b	270								
LC		NRM-8.0	L	255.6	-71.6	14			15
MC1		8.0-23.5	AL	158.8	-9.8	7.4/11.5	9.9	Yes	32
12022,310c	100								
LT		NRM-86°C	L	273.9	-72.9	13.3			3
MT1		86-240°C	L	177.5	-7.9	22.7/22.7	77.6	No	7
12022,310e	181								
LC		NRM-8.0	L	296.2	-71.3	6.3			15
MC1		5.0-50.0	L	151.3	-10.7	16.8/16.8	43	No	60
MC2(?)		50.0-85.0	AL	11.5	-32.3	16.6/35.7	40.8	No	36
12022,308a	135								
LC		NRM-4.0	L	134.2	-39.2	14.1			7

MC1		4.0-64.0	AL	124.5	-40.8	7.9/12.6	11.8	Yes	82
12022,308b	148								
LC		NRM-8.0	L	143.6	-36.8	11.6			15
MC1		8.0-85.0	AL	83.8	-42.2	9.6/15.4	14.5	Yes	95
12022,308c									
LC		NRM-5.0	L	146.2	-26.2	3.4			10
MC1		5.0-41.0	AL	116.5	-29.8	13.6/16.7	17.6	No	57
12022,305a	142								
LC		NRM-4.5	L	233.4	-34	21.7			8
MC1		4.5-25.0	L	221	10.1	12			42
MC2		25.0-60.0	AL	289.8	53.3	13.3/24.3	10.6	Yes	36
12022,305b	100								
LC		NRM-3.0	L	305.6	-46.9	24.7			5
MC1		3.0-28.0	L	225.8	-0.9	5.1			48
MC2		28.0-78.0	AL	295.8	37	10.7/17.1	6.7	Yes	51
12022,305c	129								
LC*									
MC1		NRM-22.5	L	229.3	-1.8	3.4			44
MC2		22.5-65.0	AL	278.2	37	7.7/13.5	6.3	Yes	46
12022,305d	121								
LT*									
MT1		NRM-200°C	L	220.4	-5.3	2.9			7
MT2		200-325°C	AL	274.2	38.7	6.4/8.7	7	Yes	5
15597,82a	163								
LC		NRM-4.0	L	324	12.6	24.4/24.4	28.4	No	7
15597,82b	150								
LC		NRM-6.5	L	85.5	-6	35.1			12
MC		6.5-19.0	AL	33.8	-85	12.2/35.2	9.8	Yes	26
15597,82c	167								
LC		NRM-4.0	L	69.1	-76	19.8			7
MC		4.0-16.0	AL	57.7	-53	9.6/25.8	15.8	Yes	25
15597,82d	137								

LC		NRM-4.0	L	90.0	24.3	18.9			7
MC		4.0-19.0	AL	42.4	44.7	19.3/20.4	45.2	No	31
15597,82e	145								
LC		NRM-9.5	L	305.5	-64	10.7/10.7	7.2	Yes	18
15597,82f	153								
LT		NRM-110°C	L	338.2	13.9	9.1			4
MT1		110-240°C	L	266.0	-84.9	13.0/13.0	40.0	No	6

Note: The first column identifies each subsample and specifies whether the data presented for each row refers to a low coercivity (LC) or medium coercivity (MC1 and MC2 for 12022 and MC for 15597) magnetization components. Asterisks (*) indicate that the associated component was not found in the subsample. The second column gives subsample masses. The third column specifies the AF range or temperature range for the magnetic component. The fourth column designates whether linear PCA fits for the magnetic component were forced through the origin (AL) or unconstrained (L). The fifth and sixth columns show the declination and inclination of each magnetic component. The seventh column contains the MAD of each magnetic component forced through the origin/not forced through the origin. The eighth columns contain DANG values unconstrained PCA fits for the highest coercivity MC component from each subsample. The ninth column qualitatively designates whether the given component is origin-trending according to the DANG/MAD test. The tenth column displays the number of data points (i.e., AF levels) in each component.

Table S3. Paleointensities.

Sample, Experiment	LC/LT slope	LC/LT paleointensity (μT)	MC1/MT1 slope	MC1/MT1 paleointensity (μT)	MC2/MT2 slope	MC2/MT2 paleointensity (μT)	HC range (mT)	HC slope	HC paleointensity (μT)
12022,310a									
ARM 50 μT	1.67 ± 0.64	62 ± 24	0.96 ± 0.08	36 ± 3	No MC2	No MC2	35-85	-0.09 ± 0.07	-3 ± 3
ARM 200 μT	0.63 ± 0.19	94 ± 28	0.27 ± 0.02	40 ± 2	No MC2	No MC2	35-85	-0.02 ± 0.02	-4 ± 3
IRM	0.03 ± 0.008	100 ± 24	0.013 ± 0.001	38 ± 3	No MC2	No MC2	35-85	-0.001 ± 0.001	-4 ± 3
12022,310b									
ARM 50 μT	1.05 ± 0.15	39 ± 6	1.36 ± 0.13	51 ± 5	No MC2	No MC2	23.5-85	0.14 ± 0.04	5 ± 2
ARM 200 μT	0.31 ± 0.05	46 ± 7	0.39 ± 0.02	59 ± 3	No MC2	No MC2	23.5-85	0.05 ± 0.01	7 ± 2
IRM	0.02 ± 0.003	55 ± 9	0.018 ± 0.001	55 ± 3	No MC2	No MC2	23.5-85	0.002 ±0.001	5 ± 2
12022,310e									
ARM 50 μT	1.22 ± 0.44	45 ± 16	0.66 ± 0.04	25 ± 1	No MC2	No MC2	50-85	-0.07 ± 0.06	-2 ± 2
ARM 200 μT	0.43 ± 0.09	65 ± 14	0.20 ± 0.01	29 ± 1	No MC2	No MC2	50-85	-0.02 ± 0.01	-3 ± 2
IRM	0.02 ± 0.004	70 ± 13	0.008 ± 0.0003	25 ± 1	No MC2	No MC2	50-85	-0.002 ± 0.001	-7 ± 4
12022,310c									
pTRM 10 μT	2.06 ± 9.55	21± 95	0.79 ± 0.20	8 ± 2	No MT2	No MT2			
12022,308a									
ARM 50 μT	0.75 ± 0.14	28 ± 5	0.63 ± 0.03	24 ± 1	No MC2	No MC2	64-290	0.06 ± 0.04	2 ± 2
ARM 200 μT	0.35 ± 0.09	52 ± 13	0.19 ± 0.01	28 ± 1	No MC2	No MC2	64-290	0.02 ± 0.01	2 ± 2
IRM	0.02 ± 0.005	65 ± 15	0.009 ± 0.0003	27 ± 1	No MC2	No MC2	64-290	0.002 ± 0.01	6 ± 3
12022,308b									
ARM 50 μT	0.82 ± 0.11	30 ± 4	0.69 ± 0.05	26 ± 2	No MC2	No MC2	85-290	0.01 ± 0.36	0 ± 13
ARM 200 μT	0.29 ± 0.03	43 ± 5	0.22 ± 0.01	32 ± 2	No MC2	No MC2	85-290	0.04 ±0.06	6 ± 9
12022,308c									
ARM 50 μT	0.95 ± 0.14	35 ± 5	0.98 ± 0.07	36 ± 3	No MC2	No MC2	41-290	-0.07 ± 0.04	-3 ± 2
ARM 200 μT	0.31 ± 0.05	47 ± 8	0.29 ± 0.01	43 ± 2	No MC2	No MC2	41-290	-0.02 ± 0.01	-4 ± 2
IRM	0.024 ± 0.007	73 ± 20	0.012 ± 0.007	37 ± 2	No MC2	No MC2	41-290	-0.002 ± 0.001	-5 ± 4
12022,305a									
ARM 50 μT	0.55 ± 0.18	21 ± 7	1.13 ± 0.13	42 ± 5	0.77 ± 0.35	28 ± 13	60-290	0.03 ± 0.10	1 ± 4
ARM 200 μT	0.14 ± 0.06	21 ± 10	0.39 ± 0.02	58 ± 4	0.43 ± 0.15	64 ± 15	60-290	0.04 ± 0.03	6 ± 5
IRM	0.009 ± 0.004	27 ± 12	0.03 ± 0.002	85 ± 7	0.02 ± 0.004	67 ± 13	60-290	0.006 ± 0.004	16 ± 11
12022,305b									
ARM 50 μT	0.53 ± 0.18	20 ± 7	1.85 ± 0.07	69 ± 3	0.92 ± 0.21	34 ± 8	78-290	0.02 ± 0.10	1 ± 4
ARM 200 μT	0.19 ± 0.05	28 ± 8	0.52 ± 0.01	77 ± 1	0.29 ± 0.03	42 ± 5	78-290	0.01 ± 0.03	2 ± 4

IRM	0.009 ± 0.004	27 ± 12	0.041 ± 0.002	122 ± 5	0.018 ± 0.002	54 ± 5	78-290	0.001 ± 0.004	4 ± 11
12022,305c									
ARM 50 µT	No LC	No LC	1.59 ± 0.04	59 ± 2	0.73 ± 0.19	27 ± 7	65-110	0.17 ± 0.23	6 ± 9
ARM 200 µT	No LC	No LC	0.50 ± 0.01	74 ± 1	0.22 ± 0.05	32 ± 7	65-110	0.04 ± 0.04	5 ± 6
IRM	No LC	No LC	0.048 ± 0.002	144 ± 5	0.012 ± 0.003	37 ± 8	65-110	0.005 ± 0.005	15 ± 16
Mean Values:									
ARM 50 µT	0.94 ± 0.38	35 ± 14	1.09 ± 0.43	41 ± 16	0.81 ± 0.10	30 ± 4		0.02 ± 0.09	1 ± 3
ARM 200 µT	0.33 ± 0.15	49 ± 22	0.33 ± 0.13	49 ± 19	0.31 ± 0.11	47 ± 16		0.02 ± 0.03	2 ± 4
IRM	0.019 ± 0.008	57 ± 23	0.022 ± 0.015	67 ± 46	0.017 ± 0.004	50 ± 12		0.001 ± 0.003	3 ± 6
Overall mean		46 ± 21		50 ± 31		43 ± 15			2 ± 6
15597,82a									
ARM 50 µT	0.64 ± 0.36	24 ± 13	No MC1	No MC1	No MC2	No MC2	4-290	0.08 ± 0.04	3 ± 2
ARM 200 µT	0.17 ± 0.07	26 ± 11	No MC1	No MC1	No MC2	No MC2	4-290	0.02 ± 0.01	3 ± 2
IRM	0.004 ± 0.001	11 ± 4	No MC1	No MC1	No MC2	No MC2	4-290	0.0007 ± 0.0003	2 ± 1
15597,82b									
ARM 50 µT	0.87 ± 0.67	33 ± 26	0.30 ± 0.24	11 ± 9	No MC2	No MC2	19-80	0.22 ± 0.20	8 ± 8
ARM 200 µT	0.13 ± 0.11	20 ± 16	0.09 ± 0.06	13 ± 9	No MC2	No MC2	19-80	0.05 ± 0.07	7 ± 11
IRM	0.003 ± 0.003	10 ± 9	0.002 ± 0.002	6 ± 5	No MC2	No MC2	19-80	0.002 ± 0.002	7 ± 7
15597,82c									
ARM 50 µT	1.43 ± 0.95	54 ± 36	0.38 ± 0.16	14 ± 6	No MC2	No MC2	16-290	-0.13 ± 0.14	-5 ± 5
ARM 200 µT	0.35 ± 0.21	53 ± 31	0.11 ± 0.06	17 ± 8	No MC2	No MC2	16-290	-0.10 ± 0.06	-15 ± 9
IRM	0.009 ± 0.005	26 ± 15	0.003 ± 0.001	8 ± 4	No MC2	No MC2	16-290	-0.002 ± 0.002	-6 ± 5
15597,82d									
ARM 50 µT	1.13 ± 0.17	42 ± 6	0.84 ± 0.21	31 ± 8	No MC2	No MC2	19-290	0.04 ± 0.09	2 ± 3
ARM 200 µT	0.37 ± 0.08	56 ± 11	0.38 ± 0.07	57 ± 11	No MC2	No MC2	19-290	-0.004 ± 0.04	-1 ± 7
IRM	0.011 ± 0.002	33 ± 5	0.008 ± 0.002	24 ± 5	No MC2	No MC2	19-290	0.000 ± 0.001	0 ± 4
15597,82e									
ARM 50 µT	1.87 ± 0.44	70 ± 17	No MC1	No MC1	No MC2	No MC2	9.5-85	0.03 ± 0.13	1 ± 5
ARM 200 µT	0.48 ± 0.10	72 ± 14	No MC1	No MC1	No MC2	No MC2	9.5-85	0.03 ± 0.045	4 ± 7
IRM	0.015 ± 0.003	45 ± 8	No MC1	No MC1	No MC2	No MC2	9.5-85	0.002 ± 0.001	6 ± 4
15597,82f									
pTRM	2.32 ± 2.10	23 ± 21	1.62 ± 1.84	16 ± 18	No MT2	No MT2			

Mean Values:

	slope LC/LT	paleointensity LC/LT	slope MC1/MT1	paleointensity MC1/MT1	slope MC2/MT2	paleointensity MC2/MT2	AF field range	slope flattened	paleointensity flattened
ARM 50 µT	1.19 ± 0.48	44 ± 18	0.51 ± 0.29	19 ± 11				0.05 ± 0.13	2 ± 5
ARM 200 µT	0.30 ± 0.15	45 ± 22	0.19 ± 0.17	29 ± 24				-0.001 ± 0.06	0 ± 9
IRM	0.008 ± 0.005	25 ± 15	0.004 ± 0.003	10 ± 13				-0.001 ± 0.002	2 ± 5
Overall mean		37 ± 19		20 ± 15					1 ± 6

Note: The first column identifies each subsample and the type of paleointensity experiment (ARM with bias field, IRM, or pTRM). The second column contains the slope of the NRM lost vs. either ARM gained or IRM lost or pTRM lost lines for the LC/LT components. The third column contains paleointensities ± uncertainties (in microteslas) for subsample LC/LT components. The fourth and fifth columns contain slopes and paleointensities for subsample MC1/MT1 components, respectively. The sixth and seventh columns contain slopes and paleointensities for subsample MC2/MT2 components, respectively. The eighth column contains the AF field range (in mT) beyond which the paleointensity plots for each subsample flatten out (see Fig. 3 of main text for examples). The ninth and tenth columns contain slopes and paleointensities this flattened range of AF steps. AF levels for LC, MC1, and MC2 components, as well as temperature steps for LT, MT1, and MT2 components can be found in Table S2. Uncertainties are 95% confidence intervals determined using a two-tailed Student *t*-test (in µT). Uncertainties on mean values are observed 1 standard deviation from multiple samples. All paleointensity values are computed assuming the components are thermally activated remanences.

Table S4. Paleointensity fidelity tests.

Sample	ARM bias field (µT)	TRM-equivalent field (µT)	Retrieved Paleointensity (µT)	Difference (%)	Uncertainty (µT)
12022,310b	200	149.3	100.7	32.6	8.9
	100	74.6	58.9	21.0	5.3
	50	37.3	29.3	21.6	2.8
	20	14.9	12.3	17.7	1.5
	10	7.5	13.9	86.3	1.7
	6	4.5	7.9	76.4	1.5
	3	2.2	6.2	172.9	1.5
15597,82b	200	149.3	154.7	3.7	5.8
	100	74.6	78.6	5.3	3.9
	50	37.3	46.6	25.0	3.4
	20	14.9	11.8	21.0	3.2
	10	7.5	8.8	18.2	2.0
	3	2.2	11.3	404.2	3.6
15556,221g	200	149.3	152.3	2.0	21.4
	100	74.6	51.6	30.8	13.3
	50	37.3	9.6	74.3	11.0
	20	14.9	39.2	163.1	12.0
	10	7.5	-9.6	228.0	7.9
	3	2.2	-1.4	163.6	5.3
12017,12a1c	200	149.3	48.9	67.2	11.1
	100	74.6	21.0	71.8	8.9
	50	37.3	19.7	47.2	8.6
	20	14.9	32.8	120.1	9.1
	10	7.5	19.6	161.3	9.6
	3	2.2	18.4	736.4	10.1
15016,b21	100	74.6	89.8	20.4	11.5
	50	37.3	49.4	32.4	9.8
	20	14.9	40.9	174.5	12.3
	10	7.5	13.2	76.0	16.3
	3	2.2	8.7	295.5	13.1

Note: The first column identifies each subsample. The second column contains the strength of the ARM bias field in µT used to simulate TRM. The third column contains the TRM-equivalent field strength for the given ARM µT. The fourth column contains the retrieved paleointensity in µT. The fifth column contains the percentage difference between the retrieved paleointensity and the TRM-equivalent applied field. Uncertainties (sixth column) are 95% confidence intervals determined using a two-tailed Student *t*-test (in µT). Data for samples 15556, 15016, and 12017 are modified from ref. (Tikoo et al., 2012) (see discussion in Section 4.3 of the main text).

Table S5. Rock magnetic and hysteresis parameters

Sample	M_{rs} (Am²kg⁻¹)	M_s (Am²kg⁻¹)	M_{rs}/M_s	H_{cr} (mT)	H_c (mT)	H_{cr}/H_c	Cisowski R-value	MDF_{IRM} (mT)	MDF_{ARM} (mT)	Source
15597,82b	5.66×10^{-4}			32.5			0.29	15.0	17.7	this study
15597,82a	7.13×10^{-4}	4.90×10^{-2}	1.46×10^{-2}	26	2.15	12.1				this study
15597	4.00×10^{-4}	5.80×10^{-2}	6.90×10^{-3}	77	2	38.5		52	63	(Cournède et al., 2012)
15597,20	4.80×10^{-4}	4.60×10^{-2}	1.04×10^{-2}	55	6	9.2		25-30		(Fuller et al., 1979)
12022,52	4.20×10^{-4}	4.90×10^{-2}	8.57×10^{-3}	62	8.5	7.3		33	20	(Fuller et al., 1979)
12022,310a	8.84×10^{-4}	7.70×10^{-2}	1.15×10^{-2}	48.5	2.19	22.2				this study
12022,310a	5.16×10^{-4}			47.8			0.32	23.6	20.2	this study

Note: The first column gives the subsample name, the second column shows the saturation remanent magnetization normalized by mass, the third column shows the saturation magnetization normalized by mass, the fourth column shows the ratio of saturation remanent magnetization to saturation magnetization, the fifth column shows coercivity of remanence (H_{cr}), the sixth column shows coercivity, the seventh column shows the ratio of coercivity of remanence to coercivity, the eighth column shows the Cisowski R-value (Cisowski, 1981), and the ninth and tenth columns show the MDF for IRM and ARM (Dunlop and Ozdemir, 1997). During our MDF experiments, we imparted ARM using a 200 mT AC field and a 2 mT DC field and IRM using a 200 mT DC field. These experimental conditions differ from those of refs. (Cournède et al., 2012) (which used a 110 mT AC field and 0.4 mT DC field ARM and a 3 T saturation IRM) and (Fuller et al., 1979) (which used a 100 mT AC field and 0.05 mT DC field ARM and a saturation IRM given at an unreported field strength). This difference may account for some variation in MDF values between studies. The eleventh column shows the sources for any data not acquired by this study.

Table S6. Modal mineralogy of 12022 and 15597 from refs. (Neal et al., 1994) and (Ryder, 1985).

Sample, Mineral	Abundance
12022	
Olivine	19.50%
Pyroxene	56%
Plagioclase	12.20%
Opaques	~9%
Silica	0.20%
Mesostasis	2.30%
15597	
Olivine	-
Pyroxene	59%
Plagioclase	-
Opaques	0.30%
Groundmass/Glass	41%

Table S7. Composition of plagioclase grains in 12022,114.

#	SiO$_2$	CaO	FeO	Na$_2$O	Al$_2$O3	K$_2$O	MgO	Total	An	Ab	Or	Ca/K
1	50.54	16.71	1.35	1.29	31.07	0.05	0.25	101.26	0.87	0.12	0.003	261.61
2	49.94	16.89	1.25	1.28	31.43	0.06	0.25	101.10	0.88	0.12	0.003	256.88
3	49.31	17.20	1.19	1.21	31.87	0.05	0.21	101.03	0.88	0.11	0.003	299.29
4	51.09	16.28	1.27	1.55	30.60	0.06	0.30	101.14	0.85	0.15	0.004	239.39
5	51.63	16.11	1.37	1.60	29.99	0.07	0.32	101.09	0.84	0.15	0.004	195.25
6	51.00	16.25	1.47	1.52	29.99	0.06	0.34	100.63	0.85	0.14	0.004	226.57
7	54.40	15.55	1.42	1.22	27.99	0.20	0.14	100.92	0.86	0.12	0.013	65.30
8	49.25	17.30	1.20	1.03	32.08	0.05	0.17	101.08	0.90	0.10	0.003	263.13
9	51.08	16.41	1.40	1.35	30.67	0.05	0.32	101.27	0.87	0.13	0.003	265.00
10	52.00	15.99	1.46	1.49	29.62	0.03	0.42	101.01	0.85	0.14	0.002	407.89
11	51.42	16.37	1.32	1.45	29.80	0.05	0.38	100.79	0.86	0.14	0.003	265.67
12	50.59	16.77	1.22	1.34	30.62	0.06	0.34	100.93	0.87	0.13	0.003	255.00
13	49.74	16.98	1.29	1.20	31.13	0.07	0.17	100.58	0.88	0.11	0.005	193.02
14	59.31	13.28	1.32	0.93	23.67	0.19	0.10	98.80	0.87	0.11	0.015	57.41
23	48.24	17.51	1.10	1.03	31.98	0.11	0.00	99.96	0.90	0.10	0.007	132.92
24	51.04	16.24	1.03	1.28	29.99	0.02	0.17	99.77	0.87	0.12	0.001	612.31
25	49.72	16.96	1.04	1.16	30.78	0.01	0.17	99.84	0.89	0.11	0.000	2085.00
26	48.53	17.39	0.96	1.05	32.06	0.03	0.04	100.06	0.90	0.10	0.002	428.00
27	48.74	17.43	1.12	1.05	31.81	0.09	0.00	100.24	0.90	0.10	0.005	171.40

Table S8. Composition of pyroxene grains in 12022,114.

#	TiO$_2$	SiO$_2$	K$_2$O	MnO	Na$_2$O	Cr$_2$O$_3$	Al$_2$O$_3$	CaO	FeO	MgO	Total
1.00	0.92	49.34	0.00	0.43	0.00	0.03	0.79	7.91	29.75	10.35	99.52
2.00	1.34	48.87	0.00	0.34	0.00	0.02	1.40	14.64	22.69	9.49	98.79
3.00	3.38	46.60	0.00	0.21	0.00	0.30	5.45	18.10	13.14	11.70	98.88
4.00	2.46	48.00	0.02	0.32	0.07	0.15	4.36	15.21	18.76	9.58	98.93
5.00	3.49	46.59	0.00	0.23	0.03	0.33	5.45	17.32	13.22	12.02	98.69
6.00	3.59	46.37	0.00	0.24	0.05	0.41	5.69	16.35	13.82	12.42	98.93
7.00	3.57	46.50	0.00	0.24	0.04	0.35	5.67	16.51	13.85	12.32	99.05
8.00	3.40	46.81	0.00	0.25	0.06	0.38	5.61	16.68	13.70	12.36	99.25
9.00	2.78	47.69	0.00	0.26	0.04	0.29	4.51	16.15	14.54	12.99	99.25
10.00	3.36	46.72	0.00	0.25	0.09	0.30	5.56	16.41	13.87	12.37	98.93
11.00	2.86	38.99	0.00	0.20	0.00	0.39	4.48	13.35	11.00	8.72	80.00
12.00	3.48	47.28	0.01	0.26	0.19	0.73	5.54	16.77	14.40	12.18	100.89
13.00	3.27	46.69	0.01	0.26	0.22	0.61	5.84	16.60	15.17	11.73	100.43
14.00	2.08	45.73	0.01	0.34	0.12	0.38	3.02	11.19	21.40	10.59	94.92
15.00	1.35	48.18	0.03	0.49	0.07	0.57	1.19	8.97	32.94	6.85	100.74
16.00	1.31	47.66	0.04	0.50	0.19	0.53	1.90	8.38	34.86	5.60	101.07
17.00	1.65	48.83	0.02	0.47	0.11	0.46	1.58	8.23	28.02	11.34	100.78
18.00	1.67	48.88	0.03	0.45	0.14	0.45	1.48	9.91	27.58	10.16	100.83
19.00	1.61	48.87	0.02	0.44	0.08	0.51	1.57	11.69	26.48	9.65	101.01
20.00	1.62	48.82	0.03	0.44	0.12	0.46	1.59	13.03	26.04	8.73	100.94
21.00	1.00	47.51	0.00	0.45	0.02	0.00	1.42	10.02	36.20	2.81	99.43
22.00	0.91	46.22	0.02	0.54	0.06	0.00	1.08	8.47	40.24	0.92	98.48
23.00	1.36	48.05	0.01	0.41	0.00	0.00	1.50	12.20	28.47	6.99	98.98
24.00	1.41	48.20	0.00	0.43	0.08	0.00	1.19	11.46	27.91	8.39	99.07
25.00	1.33	48.69	0.00	0.40	0.00	0.00	1.13	7.48	29.26	10.58	98.87
26.00	1.24	48.76	0.00	0.43	0.00	0.00	1.12	5.79	29.42	12.15	98.91
27.00	2.16	47.37	0.00	0.39	0.01	0.00	2.79	7.04	26.95	12.13	98.84
28.00	2.83	46.81	0.01	0.41	0.00	0.00	3.68	7.66	25.29	12.10	98.79
29.00	2.30	47.60	0.00	0.41	0.00	0.00	2.70	8.23	25.60	11.71	98.55

Table S9. Composition of olivine grains in 12022,114.

#	CaO	SiO$_2$	MnO	FeO	MgO	TiO$_2$	Al$_2$O$_3$	NiO	Na$_2$O	K$_2$O	Total
1	0.30	36.96	0.30	28.74	34.13	0.05	0.00	0.00	0.04	0.08	100.60
2	0.25	37.42	0.19	25.24	37.56	0.03	0.00	0.00	0.16	0.03	100.87
3	0.14	27.53	0.11	15.98	16.96	0.00	0.66	0.00	0.02	0.08	61.48
4	0.25	37.94	0.19	24.00	38.20	0.04	0.00	0.00	0.05	0.06	100.72
5	0.31	37.00	0.30	29.37	33.68	0.08	0.00	0.00	0.10	0.06	100.90
6	0.35	36.23	0.31	32.78	31.16	0.12	0.00	0.01	0.08	0.04	101.07
7	0.30	36.66	0.28	29.97	32.78	0.09	0.00	0.00	0.07	0.05	100.19
8	0.32	36.55	0.28	31.78	32.28	0.10	0.02	0.01	0.03	0.05	101.41
9	0.40	36.12	0.35	32.95	31.01	0.17	0.00	0.00	0.00	0.05	101.05

Table S10. Composition of high-K glass in 12022,114.

#	SiO$_2$	CaO	FeO	Na$_2$O	Al$_2$O$_3$	K$_2$O	MgO	Total
15	71.87	3.13	2.90	0.23	13.32	4.28	0.01	95.74
16	66.29	1.13	2.99	0.38	13.50	4.76	0.00	89.05
17	75.04	1.09	2.45	0.05	12.49	4.80	0.00	95.93
18	78.13	0.55	1.79	0.25	11.62	4.01	0.03	96.38
19	76.37	0.61	2.30	0.26	11.73	6.06	0.01	97.35
20	78.67	0.81	1.71	0.18	12.47	4.35	0.00	98.19
21	75.20	2.83	1.99	0.30	15.33	4.50	0.00	100.15
22	77.62	0.50	1.85	0.16	11.50	4.30	0.00	95.93

Table S11. Composition of pyroxene in 15597,13.

#	TiO$_2$	SiO$_2$	K$_2$O	MnO	Na$_2$O	Cr$_2$O$_3$	Al$_2$O$_3$	CaO	FeO	MgO	Total
30	1.57	49.25	0.18	0.22	0.41	0.00	15.28	9.48	21.11	0.80	98.30
31	3.76	41.98	0.03	0.28	0.07	0.00	10.22	15.41	21.40	5.92	99.07
32	3.27	41.35	0.15	0.25	0.41	0.00	9.78	16.83	17.98	8.36	98.37
33	2.41	45.94	0.01	0.27	0.03	0.28	7.90	15.32	18.15	9.84	100.15
34	1.76	46.90	0.01	0.24	0.05	0.68	6.24	15.64	16.13	12.13	99.78
35	0.61	50.58	0.02	0.34	0.00	0.99	3.12	6.63	20.23	18.19	100.71
36	0.47	51.49	0.01	0.30	0.00	1.14	2.24	4.59	18.07	22.09	100.40
37	0.33	52.00	0.69	0.26	1.21	0.89	1.62	2.99	15.98	23.71	99.68
38	0.18	53.36	0.01	0.23	0.00	0.72	1.05	2.93	15.93	25.58	100.00
39	1.67	47.15	0.01	0.30	0.00	0.34	6.16	8.50	23.26	12.88	100.27
40	2.53	45.24	0.10	0.26	0.55	0.04	13.87	9.75	25.20	1.65	99.19
41	1.68	48.68	0.20	0.20	0.98	0.01	16.50	9.23	16.36	0.51	94.34
42	0.33	53.38	0.00	0.26	0.06	0.85	1.20	3.29	17.09	24.92	101.38
43	0.37	53.42	0.01	0.28	0.00	0.86	1.26	2.73	16.38	25.88	101.19
44	0.27	48.89	0.31	0.27	0.29	0.70	1.36	2.85	16.40	25.02	96.35
45	0.46	51.76	0.00	0.33	0.06	1.23	2.18	3.65	17.98	22.97	100.63
46	0.57	50.89	0.00	0.32	0.05	1.26	2.70	4.98	19.42	20.25	100.44
47	1.30	48.70	0.01	0.31	0.02	0.53	4.08	12.41	19.48	13.70	100.54
48	2.14	46.74	0.01	0.30	0.00	0.36	6.89	14.99	18.63	10.50	100.56
49	2.64	45.24	0.00	0.34	0.00	0.17	8.08	15.10	20.36	8.39	100.33
50	3.56	40.02	0.01	0.38	0.06	0.17	11.67	12.58	26.39	3.56	98.42
51	2.98	42.65	0.00	0.32	0.03	0.00	9.98	12.89	24.53	6.03	99.43
52	2.67	44.87	0.01	0.31	0.13	0.09	8.07	14.17	20.68	9.05	100.05
53	1.07	48.50	0.00	0.36	0.11	0.71	4.14	9.56	19.83	15.32	99.61
54	0.54	52.10	0.00	0.30	0.00	1.11	2.68	5.44	18.71	20.25	101.14
55	0.38	52.04	0.00	0.30	0.00	1.03	1.96	4.06	17.52	22.70	99.99
56	0.38	52.61	0.00	0.29	0.00	0.97	1.66	3.39	16.86	24.00	100.16
57	0.28	53.23	0.00	0.28	0.00	0.81	1.34	2.87	16.32	24.89	100.02
58	0.25	52.90	0.00	0.28	0.00	0.78	1.24	2.77	16.21	25.16	99.59
59	1.00	48.95	0.00	0.27	0.03	1.30	4.18	12.87	15.38	15.33	99.31
60	0.20	53.20	0.00	0.27	0.00	0.61	1.22	2.87	16.54	24.89	99.80
61	0.31	53.94	0.00	0.25	0.05	0.91	1.11	2.40	16.18	25.70	100.86
62	0.36	53.34	0.00	0.28	0.06	0.99	1.38	2.63	16.16	24.93	100.16
63	0.37	53.39	0.00	0.28	0.10	0.91	1.33	2.74	16.44	24.58	100.16
64	0.43	52.38	0.00	0.27	0.10	1.17	1.87	3.15	17.05	23.28	99.73
65	0.44	50.75	0.01	0.31	0.08	1.21	2.36	4.02	18.31	20.76	98.26
66	0.96	49.11	0.00	0.34	0.15	1.49	3.75	8.86	17.66	16.84	99.18
67	1.48	48.71	0.01	0.34	0.07	0.86	6.07	14.39	17.20	11.96	101.14
68	2.14	46.08	0.01	0.30	0.18	0.35	7.19	14.55	20.29	9.22	100.37
69	2.88	43.59	0.00	0.35	0.10	0.15	9.47	13.90	23.85	5.90	100.26

Table S12. Composition of groundmass glass in 15597,13.

#	SiO$_2$	CaO	FeO	Na$_2$O	Al$_2$O3	K$_2$O	MgO	Total
1	50.41	9.32	20.49	0.85	16.53	0.15	0.36	98.12
2	49.51	9.62	20.93	0.86	16.38	0.12	0.44	97.86
3	49.09	9.46	21.00	0.74	16.17	0.13	0.39	96.97
4	49.16	9.34	21.77	0.68	16.16	0.12	0.35	97.58
5	49.78	9.73	20.82	0.94	16.49	0.13	0.37	98.27
6	49.41	9.80	19.47	1.01	16.99	0.15	0.37	97.20
7	49.03	9.78	19.61	1.00	16.80	0.14	0.44	96.79
8	48.78	9.28	20.64	0.88	16.37	0.14	0.39	96.48
9	49.50	9.42	19.92	0.80	16.98	0.15	0.30	97.07
10	49.83	9.36	19.41	1.05	16.89	0.14	0.35	97.03
11	53.20	9.25	15.35	1.35	19.24	0.21	0.14	98.73
12	52.90	9.41	15.27	1.44	19.84	0.18	0.17	99.21
13	51.97	9.20	15.87	1.40	19.42	0.20	0.13	98.20

Note: Analyses presented as wt% oxides rounded to the nearest decimal place. Calculations were conducted using raw data. Detection limits as follows (in wt%): Metals; Ni-0.019, Fe-0.027. Silicates; Ni-0.017, Fe-0.015 (0.0375 in feldspar), K-0.01, Cr-0.008, Na-0.14 (0.022 in pyroxene). ‡An, Ab, and Or data are presented as relative percentage (e.g., An = CaO/(Na2O+CaO+K2O) and rounded to the nearest decimal place. FeO, CaO, TiO2, Mn, MgO, K2O, and Na2O are presented as mass percents. Standards for Fe and Ni analyses are were pure Fe and Ni metal. Silicate standards were synthetic orthoclase (K), clinopyroxene (Ca),rutile (Ti), rhodonite (Mn), and orthopyroxene (Fe, Mg).

Table S13. Complete $^{40}Ar/^{39}Ar$ incremental heating results.

#	Temp (°C)	Time (s)	^{40}Ar ± 1σ	^{39}Ar ± 1σ	^{38}Ar ± 1σ	^{37}Ar ± 1σ	^{36}Ar ± 1σ	$^{40}Ar^*$ (%)	$^{39}Ar_k$ (%)	$^{38}Ar_{cos}$ (%)	$^{38}Ar_{trap}$ (%)	$^{38}Ar_{Cl}$ (%)	$^{36}Ar_{cos}$ (%)	$^{36}Ar_{trap}$ (%)	Ca/K	Apparent Age ± 1σ (Ma)
	12022		whole-rock fragment													
1	460 °C	596	0.38691 ± 0.00054	0.00586 ± 0.00025	0.00160 ± 0.00010	0.01537 ± 0.00291	0.00100 ± 0.00009	100.0	99.8	95.4	0.0	0.0	100.0	0.0	5.2	1106 ± 37
2	460 °C	597	0.30387 ± 0.00071	0.00440 ± 0.00025	0.00106 ± 0.00010	0.01102 ± 0.00296	0.00063 ± 0.00009	100.0	99.8	95.4	-0.4	0.0	103.5	-4.0	4.9	1143 ± 49
3	514 °C	597	1.05638 ± 0.00131	0.01109 ± 0.00026	0.00436 ± 0.00010	0.04846 ± 0.00316	0.00288 ± 0.00010	100.0	99.7	96.2	0.6	0.0	94.5	5.1	8.6	1440 ± 27
4	513 °C	597	0.78765 ± 0.00076	0.00775 ± 0.00025	0.00284 ± 0.00010	0.03134 ± 0.00311	0.00188 ± 0.00009	100.0	99.7	96.0	0.7	0.0	94.1	5.5	7.9	1506 ± 36
5	567 °C	597	2.12475 ± 0.00211	0.01433 ± 0.00026	0.00939 ± 0.00010	0.10779 ± 0.00348	0.00624 ± 0.00010	100.0	99.5	97.6	0.6	0.0	95.1	4.5	14.8	1925 ± 27
6	566 °C	597	1.55205 ± 0.00141	0.00916 ± 0.00026	0.00622 ± 0.00010	0.07405 ± 0.00344	0.00407 ± 0.00010	100.0	99.4	97.8	0.3	0.0	96.7	2.8	15.9	2087 ± 39
7	620 °C	596	3.56077 ± 0.00361	0.01518 ± 0.00029	0.01729 ± 0.00011	0.19574 ± 0.00403	0.01145 ± 0.00010	100.0	99.1	98.5	0.4	0.0	96.4	3.2	25.5	2514 ± 32
8	620 °C	597	2.40319 ± 0.00310	0.00941 ± 0.00027	0.01139 ± 0.00011	0.12430 ± 0.00359	0.00747 ± 0.00010	100.0	99.1	98.7	0.3	0.0	97.5	2.1	26.1	2632 ± 44
9	673 °C	596	5.02659 ± 0.00391	0.01572 ± 0.00030	0.02872 ± 0.00013	0.34447 ± 0.00479	0.01867 ± 0.00011	100.0	98.5	99.2	0.1	0.0	98.9	0.6	43.6	2959 ± 34
10	672 °C	596	3.32875 ± 0.00291	0.00972 ± 0.00027	0.01985 ± 0.00011	0.23286 ± 0.00425	0.01303 ± 0.00010	100.0	98.3	99.2	0.2	0.0	97.8	1.7	47.7	3062 ± 46
11	725 °C	597	6.41133 ± 0.00501	0.01806 ± 0.00030	0.04626 ± 0.00016	0.54356 ± 0.00566	0.02983 ± 0.00012	100.0	97.9	99.6	-0.1	0.0	100.0	-0.5	60.2	3122 ± 32
12	725 °C	597	4.02188 ± 0.00231	0.01084 ± 0.00027	0.03053 ± 0.00013	0.36628 ± 0.00463	0.01977 ± 0.00011	100.0	97.7	99.6	0.0	0.0	99.6	-0.1	67.8	3192 ± 43
13	777 °C	596	6.81132 ± 0.00541	0.01800 ± 0.00030	0.05690 ± 0.00015	0.67554 ± 0.00601	0.03701 ± 0.00012	100.0	97.4	99.6	0.0	0.0	99.1	0.4	75.5	3225 ± 33
14	777 °C	597	4.20162 ± 0.00302	0.01142 ± 0.00027	0.03638 ± 0.00014	0.43469 ± 0.00473	0.02385 ± 0.00011	100.0	97.4	99.4	0.2	0.0	98.3	1.3	76.6	3184 ± 42
15	829 °C	597	6.74730 ± 0.00551	0.01839 ± 0.00031	0.06394 ± 0.00019	0.76221 ± 0.00650	0.04225 ± 0.00012	100.0	97.1	99.4	0.3	0.0	97.4	2.1	83.7	3184 ± 32
16	829 °C	596	3.91312 ± 0.00342	0.01096 ± 0.00029	0.03891 ± 0.00013	0.45798 ± 0.00538	0.02562 ± 0.00012	100.0	97.1	99.4	0.2	0.0	97.8	1.7	84.4	3144 ± 45
17	880 °C	596	6.14474 ± 0.00471	0.01640 ± 0.00028	0.06262 ± 0.00018	0.72984 ± 0.00603	0.04153 ± 0.00012	100.0	96.9	99.4	0.3	0.0	97.0	2.5	90.0	3218 ± 33
18	880 °C	597	3.16103 ± 0.00331	0.00884 ± 0.00029	0.03400 ± 0.00013	0.39523 ± 0.00453	0.02258 ± 0.00011	100.0	96.9	99.3	0.3	0.0	96.9	2.7	90.5	3149 ± 54
19	931 °C	596	5.23921 ± 0.00472	0.01602 ± 0.00029	0.05180 ± 0.00016	0.59694 ± 0.00592	0.03469 ± 0.00012	100.0	97.4	99.1	0.5	0.0	95.9	3.7	75.0	3009 ± 33
20	931 °C	596	1.83638 ± 0.00163	0.00559 ± 0.00027	0.02096 ± 0.00012	0.22510 ± 0.00473	0.01401 ± 0.00010	100.0	97.2	99.2	0.4	0.0	96.1	3.4	81.2	3018 ± 76
21	982 °C	597	4.73551 ± 0.00434	0.01568 ± 0.00029	0.08386 ± 0.00020	0.88846 ± 0.00680	0.05754 ± 0.00012	100.0	96.1	99.0	0.8	0.0	93.4	6.2	115.6	2913 ± 34
22	983 °C	595	1.43461 ± 0.00099	0.00460 ± 0.00026	0.02638 ± 0.00012	0.26784 ± 0.00504	0.01750 ± 0.00011	100.0	96.0	99.5	0.3	0.0	97.1	2.5	119.0	2962 ± 89
23	1033 °C	596	3.94103 ± 0.00421	0.01339 ± 0.00029	0.22521 ± 0.00041	2.33627 ± 0.01087	0.14332 ± 0.00025	100.0	87.9	100.2	-0.3	0.0	102.0	-2.4	389.2	3005 ± 41
24	1033 °C	596	1.16708 ± 0.00135	0.00425 ± 0.00025	0.06846 ± 0.00021	0.72190 ± 0.00675	0.04449 ± 0.00014	100.0	88.2	99.9	0.0	0.0	99.6	0.0	377.6	2899 ± 100
25	1083 °C	596	7.89628 ± 0.00493	0.02961 ± 0.00035	0.90790 ± 0.00086	9.61541 ± 0.02535	0.58699 ± 0.00067	100.0	77.4	100.0	-0.1	0.0	100.2	-0.6	821.9	3046 ± 30
26	1084 °C	596	0.00134 ± 0.00033	0.00009 ± 0.00025	-0.00010 ± 0.00010	0.00377 ± 0.00377	0.00003 ± 0.00009	100.0	97.0	122.6	-21.5	0.0	-227.3	324.4	88.6	336 ± 912

Isotope abundances given in nanoamps (spectrometer sensitivity is ~1.8 x 10^{-14} moles/nA),

    and corrected for ^{37}Ar and ^{39}Ar decay, with half-lives of 35.2 days and 269 years, respectively,

    and for spectrometer discrimination per atomic mass unit of 1.00095 ± 0.00199.

Isotope sources calculated using the reactor constants in Renne et al. (2005),

    and assuming $(^{38}Ar/^{36}Ar)_{cos}$ = 1.54, $(^{38}Ar/^{36}Ar)_{trap}$ = 0.188, and $(^{40}Ar/^{36}Ar)_{trap}$ = 0.

No corrections were made for cosmogenic ^{40}Ar.

Ages were calculated using the decay constants and standard age calibration of Renne et al. (2011) and K isotope abundances of Steiger and Jäger (1977)

    and calculated relative to Hb3gr fluence monitor (1081.0 ± 1.2 Ma).

J-Value is 0.012746 ± 0.0001683 (analytical uncertainties only, excludes uncertainty on the standard age).

Uncertainties on apparent step ages include anlytical uncertainties on isotope measurements, interference corrections, and the J-value, but exclude decay constant and standard age uncertainties.

The plateau age was calculated from the weighted average $^{40}Ar^*/^{39}Ar_K$ ratio of steps 12-18.

Average analytical blanks are: ^{40}Ar = 0.03; ^{39}Ar = 0.0009; ^{38}Ar = 0.0002; ^{37}Ar = 0.00005; ^{36}Ar = 0.0002 (nanoamps).

Temperature was controlled with approximately ± 5 °C precision and ± 10 °C accuracy.

Data shown in gray are indeterminate or negligibly above the detection limit.

Table S14. Summary of MP-MDD model parameters with cosmogenic ^{38}Ar production rates for 12022.

Phase	E_a (kJ/mol)	$\ln(D_o/a^2)_1$ $(\ln(s^{-1}))$	F_{39-1}	F_{37-1}	K/Ca_1	Fe/Ca_1	$P38_{Ca-1}$ (mol/g$_{Ca}$/Ma)	$\ln(D_o/a^2)_2$ $(\ln(s^{-1}))$	F_{39-2}	F_{37-2}	K/Ca_2	Fe/Ca_2	$P38_{Ca-2}$ (mol/g$_{Ca}$/Ma)
12022													
Plagioclase	182	10.8	0.060	0.599	0.0019	0.063	6.29×10^{-13}	9.4	0.052	0.398	0.0025	0.063	6.29×10^{-13}
K-Glass	131	9.0	0.210	0.001	4.01	1.55	4.80×10^{-12}	4.8	0.678	0.002	6.47	1.55	7.35×10^{-12}

Note: Each phase is fit with a two domain model. F is the fraction of ^{39}Ar$_K$ or ^{37}Ar$_{Ca}$ contained within a given domain and was calculated relative to the total gas released in the first 18 extractions and half of the 19th extraction. P38$_{Ca}$ is the domain-specific production rate for ^{38}Ar$_{cos}$ and is calculated based on the relative concentrations of Ca, K, and Fe in plagioclase and K-glass using the ^{38}Ar production rate from Ca of Turner al. (1971) and the relative K/Ca and Fe/Ca production rates of Eugster and Michel (1995). Total ^{39}Ar$_K$, ^{37}Ar$_{Ca}$, and ^{38}Ar$_{cos}$ signals are 0.219, 5.85, and 0.494 nanoamps, respectively.

Table S15. Summary of ^{40}Ar/^{39}Ar chronology for 12022.

^{40}Ar/^{39}Ar Radioisotopic Age (Ma)			^{38}Ar/^{37}Ar Exposure Age (Ma)		
Steps	MSWD	Age ± 1σ *	Steps	MSWD	Age ± 1σ
12-18	0.82	3194 ± 12 (25)	7-19	0.15	262.7 ± 4.9

Note: MSWD = mean square weighted deviation for age fits to release listed steps. Errors reflect analytical uncertainties on isotope measurements and do not include decay constant, standard age, J-Value, or production rate uncertainties. * 1σ error is 25 Ma when J-Value, standard age, and decay constant uncertainty are included.

Table S16. Paleointensities generated by the precession dynamo for various a-t relationships and P_{th} values.

a-t model	P_{th} (W)	Paleointensity at 3.56 Ga (µT)	Paleointensity at 3.19 Ga (µT)	Factor Decrease in Paleointensity
4	5×10^8	1.68	0.97	1.74
4	7.5×10^8	1.68	0.97	1.74
4	1×10^9	1.68	0.97	1.74
4	2.5×10^9	1.68	0.97	1.74
4	5×10^9	1.68	0.97	1.74
4	7.5×10^9	1.68	0.96	1.74
4	1×10^{10}	1.68	0.96	1.75
4	2.5×10^{10}	1.68	0.95	1.76
Nominal	5×10^8	0.83	0.40	2.10
Nominal	7.5×10^8	0.83	0.40	2.11
Nominal	1×10^9	0.83	0.39	2.11
Nominal	2.5×10^9	0.83	0.39	2.15
Nominal	5×10^9	0.83	0.37	2.21
Nominal	7.5×10^9	0.83	0.36	2.28
Nominal	1×10^{10}	0.82	0.35	2.37
Nominal	2.5×10^{10}	0.81	0.22	3.66
2	5×10^8	0.38	0.24	1.56
2	7.5×10^8	0.38	0.24	1.58
2	1×10^9	0.37	0.24	1.59
2	2.5×10^9	0.37	0.21	1.71
2	5×10^9	0.35	0.17	2.12
2	7.5×10^9	0.34	0.00	dynamo ceased
2	1×10^{10}	0.32	0.00	dynamo ceased
2	2.5×10^{10}	0.13	0.00	dynamo ceased

Note: The first column contains the semimajor axis to time (*a-t*) relationships utilized by Dwyer et al. (2011), which represent end-member (#2 and #4) (Walker et al., 1983) and nominal (Webb, 1982) models for the lunar orbit evolution. The second column contains the adiabatic threshold (P_{th}). The third and fourth columns contain the paleointensity determined for the given *a-t* relationship at 3.56 and 3.19 Ga, respectively, using the scaling law of Christensen et al. (2009) and assuming the same parameters used by Dwyer et al. (2011). We assumed that the ratio of the dipolar to total field at the core-mantle boundary was 1/7. The fifth column contains the factor decrease in paleointensity between 3.56 and 3.19 Ga.

Supplement References

Arvidson, R., Crozaz, G., Drozd, R.J., Hohenberg, C.M., Morgan, C.J., 1975. Cosmic ray exposure ages of features and events at the Apollo landing sites. The Moon 13, 259-276.

Audunsson, H., Levi, S., 1989. Drilling-induced remanent magnetization in basalt drill cores. Geophys. J. 98, 613-622.

Bauch, K.E., Hiesinger, H., Helbert, J., 2009. Estimation of lunar surface temperatures: A numerical model. Proc. Lunar Planet. Sci. Conf. 40th 1789.

Bezaeva, N.S., Gattacceca, J., Rochette, P., Sadykov, R.A., Trukhin, V.I., 2010. Demagnetization of terrestrial and extraterrestrial rocks under hydrostatic pressure up to 1.2 Ga. Phys. Earth Planet. Inter. 179, 7-20.

Bogard, D.D., Funkhouser, J.G., Schaeffer, O.A., Zahringer, J., 1971. Noble gas abundances in lunar material--Cosmic-ray spallation products and radiation ages from the Sea of Tranquility and the Ocean of Storms. J. Geophys. Res. 76, 2757-2779.

Brett, R., Butler, P., Meyer, C., Reid, A.M., Takeda, H., Williams, R., 1971. Apollo 12 igneous rocks 12004, 12008, 12009 and 12022: A mineralogical and petrological study. Proc. Lunar Sci. Conf. 2nd 301-317.

Burmester, R.F., 1977. Origin and stability of drilling induced remanence. Geophys. J. Roy. Astr. S. 48, 1-14.

Burnett, D.S., Drozd, R.J., Morgan, C.J., Podosek, F.A., 1975. Exposure histories of Bench Crater rocks. Proc. Lunar Sci. Conf. 6th 2219-2240.

Cassata, W., Shuster, D.L., Renne, P.R., Weiss, B.P., 2010. Evidence for shock heating and constraints on Martian surface temperatures revealed by $^{40}Ar/^{39}Ar$ thermochronometry of Martian meteorites Geochimica et Cosmochimica Acta 74, 6900-6920.

Cassata, W.S., Renne, P.R., Shuster, D.L., 2009. Argon diffusion in plagioclase and implications for thermochronometry: A case study from the Bushveld Complex, South Africa. Geochimica et Cosmochimica Acta 73, 6600-6612.

Chowdhary, S.K., Collinson, D.W., Stephenson, A., Runcorn, S.K., 1985. Further investigations into lunar paleointensity determinations. Proc. Lunar Planet. Sci. 16th 121-122.

Chowdhary, S.K., Collinson, D.W., Stephenson, A., Runcorn, S.K., 1987. Further investigations into lunar paleointensity determinations. Phys. Earth Planet. Inter. 49, 133-141.

Christensen, U.R., Holzwarth, V., Rainers, A., 2009. Energy flux determines magnetic field strength of planets and stars. Nature 457, 167-169.

Cisowski, S., Hale, C., Fuller, M., 1977. On the intensity of ancient lunar fields. Proc. Lunar. Sci. Conf. 8th 725-750.

Cisowski, S., 1981. Interacting vs. non-interacting single-domain behavior in natural and synthetic samples. Phys. Earth Planet. Inter. 26, 56-62.

Cisowski, S.M., Collinson, D.W., Runcorn, S.K., Stephenson, A., Fuller, M., 1983. A review of lunar paleointensity data and implications for the origin of lunar magnetism. Proc. Lunar Planet. Sci. Conf.13th A691-A704.

Cournède, C., Gattacceca, J., Rochette, P., 2012. Magnetic study of large Apollo samples: Possible evidence for an ancient centered dipolar field on the Moon. Earth Planet. Sci. Lett. 331-332, 31-42.

Crawford, D.A., Schultz, P.H., 1999. Electromagnetic properties of impact-generated plasma, vapor and debris. Int. J. Impact Eng. 23, 169-180.

de Koker, N., Steinle-Neumann, G., Vlček, V., 2012. Electrical resistivity and thermal conductivity of liquid Fe alloys at high P and T, and heat flux in the Earth's core. Proc. Natl. Acad. Sci. USA 109, 4070-4073.

Dixon, J.R., Papike, J.J., 1975. Petrology of anorthosites from the Descartes region of the moon: Apollo 16. Proc. Lunar Sci. Conf. 6th.

Dunlop, D.J., Ozdemir, O., 1997. Rock Magnetism: Fundamentals and Frontiers. Cambridge University Press, New York. 573 pp.

Dunlop, D.J., Ozdemir, O., 2001. Beyond Néel's theories: thermal demagnetization of narrow-band partial thermoremanent magnetizations. Phys. Earth Planet. Inter. 126, 43-57.

Dunlop, D.J., 2002. Theory and application of the Day plot (Mrs/Ms versus Hcr/Hc) - 1. Theoretical curves and tests using titanomagnetite data. J. Geophys. Res. 107, doi:10.1029/2001JB000486.

Dwyer, C.A., Stevenson, D.J., Nimmo, F., 2011. A long-lived lunar dynamo driven by continuous mechanical stirring. Nature 479.

Egli, R., 2003. Analysis of the field dependence of remanent magnetization curves. J. Geophys. Res. 108, 2081.

Evans, A.J., Zuber, M.T., Weiss, B.P., Tikoo, S.M., 2013. A wet, heterogeneous lunar interior: lower mantle & core dynamo evolution. J. Geophys. Res. Submitted.

Evensen, N.M., Murthy, V.R., Coscio, M.R., 1973. Rb-Sr ages of some mare basalts and the isotopic and trace element systematics in lunar fines. Proc. Lunar Sci. Conf. 4th 1707-1724.

Fechtig, H., Kalbitzer, S.T., 1966. The diffusion of argon in potassium-bearing solids. In: Schaeffer, O.A., Zahringer, J. (Eds.), Potassium Argon Dating, Springer-Verlag, New York. pp. 68-107.

Fuller, M., Meshkov, E., Cisowski, S., Hale, C., 1979. On the natural remanent magnetization of certain mare basalts. Proc. Lunar Planet. Sci. 10th 2211-2233.

Fuller, M., Hastedt, M., Herr, B., 1998. Coring-induced magnetization of recovered sediment. In: Weaver, P., Schmincke, H.-U., Firth, J., Duffield, W. (Eds.), Proceedings of the Ocean Drilling Program, Scientific Results 157. pp. 47-56.

Garrick-Bethell, I., Weiss, B.P., Shuster, D.L., Buz, J., 2009. Early lunar magnetism. Science 323, 356-359.

Garrick-Bethell, I., Weiss, B.P., 2010. Kamacite blocking temperatures and applications to lunar magnetism. Earth Planet. Sci. Lett. 294, 1-7.

Gattacceca, J., Rochette, P., 2004. Toward a robust normalized magnetic paleointensity method applied to meteorites. Earth Planet. Sci. Lett. 227, 377-393.

Gattacceca, J., Berthe, L., Boustie, M., Vadeboin, F., Rochette, P., De Resseguier, T., 2008. On the efficiency of shock magnetization processes. Phys. Earth Planet. Inter. 166, 1-10.

Gattacceca, J., Boustie, M., Hood, L.L., Cuq-Lelandais, J.-P., Fuller, M., Bezaeva, N.S., de Resseguier, T., Berthe, L., 2010. Can the lunar crust be magnetized by shock: Experimental groundtruth. Earth Planet. Sci. Lett. 299, 42-53.

Gomi, H., Ohta, K., Hirose, K., Labrosse, S., Caracas, R., Verstraete, M.J., Hernlud, J.W., 2013. The high conductivity of iron and thermal evolution of the Earth's core. Phys. Earth Planet. Inter. 224, 88-103.

Grove, T.L., Walker, D., 1977. Cooling histories of Apollo 15 quartz-normative basalts. Proc. Lunar Planet. Sci. Conf. 8th 1501-1520.

Hanley, E.J., Dewitt, D.P., Roy, R.F., 1978. The thermal diffusivity of eight well-characterizedrocks for the temperature range 300-1000 K. Eng. Geology 12, 31-47.

Helsley, C.E., 1971. Evidence for an ancient lunar magnetic field. Proc. Lunar Planet. Sci. 3rd. 2485-2490.

Hood, L.L., Mitchell, D.L., Lin, R.P., Acuna, M.H., Binder, A.B., 1999. Initial measurements of the lunar induced magnetic dipole moment using Lunar Prospector magnetometer data. Geophys. Res. Lett. 26, 2327-2330.

Hood, L.L., Artemieva, N.A., 2008. Antipodal effects of lunar basin-forming impacts: Initial 3D simulations and comparisons with observations. Icarus 193, 485-502.

Horn, P., Kirsten, T., Jessberger, E.K., 1975. Are there A 12 mare basalts younger than 3.1 b.y. Unsuccessful search for A 12 mare basalts with crystallization ages below 3.1 b.y. Meteoritics 10, 417-418.

Huang, S., 2008. Surface temperatures at the nearside of the Moon as a record of the radiation budget of Earth's climate system. Adv. Space Res. 41, 1853-1860.

Jackson, M., Van der Voo, R., 1985. Drilling-induced remanence in carbonate rocks: occurrence, stability and grain-size dependence. Geophys. J. Roy. Astr. S. 81, 75-87.

James, O.B., Wright, T.L., 1972. Apollo 11 and 12 mare basalts and gabbros: Classification, compositional variations and possible petrogenetic relations. Geol. Soc. Am. Bull. 83, 2357-2382.

Kaufman, L., Cohen, M., 1956. The martensitic transformation in the iron-nickel system. T. Am. I. Min. Met. Eng. 206, 1393-1401.

Kirsten, T., Deubner, J., Horn, P., Kaneoka, I., Kiko, J., Schaeffer, O.A., Thio, S.K., 1972. The rare gas record of Apollo 14 and 15 samples. Proc. Lunar Planet. Sci. Conf. 3rd 1865-1889.

Kirsten, T., Horn, P., Kiko, J., 1973. Ar40-Ar39 dating of Apollo 16 and Apollo 15 rocks and rare gas analysis of Apollo 16 soils. Proc. Lunar Sci. Conf. 4th 438-440.

Kodama, K.P., 1984. Palaeomagnetism of granitic intrusives from the Precambrian basement under eastern Kansas: orienting drill cores using secondary magnetization. Geophys. J. Roy. Astr. S. 76, 273-287.

Konopliv, A.S., Binder, A.B., Hood, L.L., Kucinskas, A.B., Sjogren, W.L., Williams, J.G., 1998. Improved gravity field of the Moon from Lunar Prospector. Science 281, 1476-1480.

Laneuville, M., Wieczorek, M.A., Breuer, D., Aubert, J., Morard, G., Rückriemen, T., 2014. A long-lived lunar dynamo powered by core crystallization. Earth Planet. Sci. Lett. submitted.

Lawrence, K., Johnson, C., Tauxe, L., Gee, J.S., 2008. Lunar paleointensity measurements: Implications for lunar magnetic evolution. Phys. Earth Planet. Inter. 168, 71-87.

Lovera, O.M., Richter, F.M., Harrison, T.M., 1991. Diffusion domains determined by ^{39}Ar released during step heating. J. Geophys. Res. 96, 2057-2069.

Marti, K., Lugmair, G.W., 1971. Kr81-Kr and K-Ar40 ages, cosmic-ray spallation products, and neutron effects in lunar samples from Oceanus Procellarum. Proc. Lunar Sci. Conf. 2nd 1591-1605.

Muxworthy, A.R., Heslop, D., Paterson, G.A., Michalk, D., 2011. A Preisach method for estimating absolute paleofield intensity under the constraint of using only isothermal measurements: 2. Experimental testing. J. Geophys. Res. 116, 1-20.

Neal, C.R., Hacker, M.D., Snyder, G.A., Taylor, L.A., Liu, Y.-G., Schmitt, R.A., 1994. Basalt generation at the Apollo 12 site. Part 2: Source heterogeneity, multiple melts, and crustal contamination. Meteoritics 29, 349-361.

Papike, J.J., Hodges, F.N., Bence, A.E., Cameron, M., Rhodes, J.M., 1976. Mare basalts: Crystal chemistry, mineralogy and petrology. Rev. Geophys. Space Phys. 14, 475-540.

Pearce, G.W., Hoye, G.S., Strangway, D.W., 1976. Some complexities in the determination of lunar paleointensities. Proc. Lunar Sci. Conf. 7th 3271-3297.

Phinney, D., Kahl, S.B., Reynolds, J.H., 1975. 40Ar-39Ar dating of Apollo 16 and 17 rocks. Proc. Lunar Sci. Conf. 6th 1593-1608.

Pinto, M.J., McWilliams, M., 1990. Drilling-induced isothermal remanent magnetization. Geophysics 55, 111-115.

Reid, A.M., Meyer, C., Harmon, R.S., Brett, R., 1970. Metal grains in Apollo 12 igneous rocks. Earth Planet. Sci. Lett. 9, 1-5.

Reisener, R.J., Goldstein, J.I., 2003. Ordinary chondrite metallography: Part 1. Fe-Ni taenite cooling experiments. Meteorit. Planet Sci. 38, 1669-1678.

Renne, P.R., Mundil, R., Balco, G., Min, K., Ludwig, K., 2010. Joint determination of 40K decay constants and 40Ar*/40K for the Fish Canyon sanidine standard, and improved accuracy for 40Ar/39Ar geochronology. Geochim. Cosmochim. Ac. 74, 5349-5367.

Renne, P.R., Balco, G., Ludwig, K., Mundil, R., Min, K., 2011. Response to the Comment by W. H. Schwarz et al. on "Joint determination of 40K decay constants and 40Ar*/40K for the Fish Canyon sanidine standard, and improved accuracy for 40Ar/39Ar geochronology" by P.R. Renne et al. (2010). Geochimica et Cosmochimica Acta 75, 5097.

Rhodes, J.M., Hubbard, N.J., 1973. Chemistry, classification, and petrogenesis of Apollo 15 mare basalts. Proc. Lunar Sci. Conf. 4th 1127-1148.

Roelof, E.C., 1968. Thermal behavior of rocks on the lunar surface. Icarus 8, 138-159.

Romig, A.D., Goldstein, J.I., 1981. Low temperature phase equilibria in the Fe-Ni and Fe-Ni-P systems: application to the thermal history of metallic phases in meteorites. Geochim. Cosmochim. Ac. 45, 1187-1197.

Ryder, G., (Ed.) Catalog of Apollo 15 Rocks, NASA Curatorial Branch, Houston, 1985.

Sadykov, R.A., 2008. Nonmagnetic high pressure cell for magnetic remanence measurements up to 1.5 GPa in a superconducting quantum interference device magnetometer. Rev. Sci. Instrum. 79, 115102.

Schaeffer, O.A., Husain, L., 1974. Chronology of lunar basin formation. Proc. Lunar Sci. Conf. 5th 2, 1541-1555.

Sclar, C.B., Bauer, J.F., Pickart, S.J., Alperin, H.A., 1973. Shock effects in experimentally shocked terrestrial ilmenite, lunar ilmenite of rock fragments in 1-10 mm fines (10085) an lunar rock 60015,127. Proc. Lunar Sci. Conf. 4th 841-859.

Sclar, C.B., Bauer, J.F., 1974. Shock-induced melting in anorthositic rock 60015 and a fragment of anorthositic breccia from the picking pot. Proc. Lunar Sci. Conf. 5th 319-336.

See, T.H., 1986. Apollo 16 impact-melt splashes: Petrography and major-element composition. Proc. Lunar Planet. Sci. Conf. 17th E3-E20.

Selkin, P.A., Gee, J.S., Tauxe, L., Meurer, W.P., Newell, A.J., 2000. The effect of remanence anisotropy on paleointensity estimates: A case study from the Archean Stillwater Complex. Earth Planet. Sci. Lett. 183, 403.

Shea, E.K., Weiss, B.P., Cassata, W.S., Shuster, D.L., Tikoo, S.M., Gattacceca, J., Grove, T.L., Fuller, M.D., 2012. A long-lived lunar core dynamo. Science 335, 453-456.

Shimizu, H., Matsushima, F., Takahashi, F., Shibuya, H., Tsunakawa, H., 2013. Constraint on the lunar core size from electromagnetic sounding based on magnetic field observations by an orbiting satellite. Icarus 222, 32-43.

Shoemaker, E.M., Batson, R.M., Bean, A.L., Conrad, C., Dahlem, D.H., Goddard, E.N., Hait, M.H., 1970. Preliminary geologic investigation of the Apollo 12 landing site, Apollo 12 Preliminary Science Report, NASA Publication SP-235. pp. 113-156.

Shuster, D.L., Balco, G., Cassata, W.S., Fernandes, V.A., Garrick-Bethell, I., Weiss, B.P., 2010. A record of impacts preserved in the lunar regolith. Earth Planet. Sci. Lett. 290, 155-165.

Soderlund, K.M., Schubert, G., Scheinberg, A.L., 2013. Persistence fo the lunar dynamo: The role of compositional convection. American Geophysical Union Fall Meeting #GP41D-1157.

Spudis, P.D., Swann, G.A., Greeley, R., 1988. The formation of Hadley Rille and implications for the geology of the Apollo 15 region. Proc. Lunar Planet. Sci. Conf. 18th 243.

Stegman, D.R., Jellinek, A.M., Zatman, S.A., Baumgardner, J.R., Richards, M.A., 2003. An early lunar dynamo driven by thermochemical mantle convection. Nature 421, 143-146.

Steiger, R.H., Jager, E., 1977. Subcommission on geochronology: Convention on the use of decay constants in geo- and cosmochronology. Earth Planet. Sci. Lett. 36, 359-362.

Stephenson, A., Collinson, D.W., 1974. Lunar magnetic field paleointensities determined by an anhysteretic remanent magnetization method. Earth Planet. Sci. Lett. 23, 220-228.

Stephenson, A., Sadikun, S., Potter, D.K., 1986. A theoretical and experimental comparison of the anisotropies of magnetic susceptibility and remanence in rocks and minerals. Geophys. J. Roy. Astr. S. 84, 185-200.

Stettler, A., Eberhardt, P., Geiss, J., Grogler, N., Maurer, P., 1973. Ar39-Ar40 ages and Ar37-Ar38 exposure ages of lunar rocks. Proc. Lunar Sci. Conf. 4th 1865-1888.

Stöffler, D., Ryder, G., Ivanov, B.A., Artemieva, N.A., Cintala, M.J., Grieve, R.A.F., 2006. Cratering history and lunar chronology. Rev. Mineral. Geochem. 60, 519-596.

Suavet, C., Weiss, B.P., Cassata, W.S., Shuster, D.L., Gattacceca, J., Chan, L., Garrick-Bethell, I., Head, J.W., Grove, T.L., Fuller, M.D., 2013. Persistence and origin of the lunar core dynamo. Proc. Natl. Acad. Sci. USA 110, 8453-8458.

Swann, G.A., Bailey, N.G., Batson, R.M., Freeman, V.L., Hait, M.H., 1972. Preliminary geologic investigation of the Apollo 15 landing site, Apollo 15 Preliminary Science Report, NASA Publication SP-289. pp. 5.1-5.112.

Swartzendruber, L.J., Itkin, V.P., Alcock, C.B., 1991. The Fe-Ni (iron-nickel) system. J. Phase Equil. 12, 288-312.

Thellier, E., Thellier, O., 1959. Sur l'intensité du champ magnétique terrestre dans le passé historique et géologique. Ann. Geophys. 15, 285-376.

Tian, B.Y., Stanley, S., Tikoo, S., Weiss, B., Wisdom, J., 2014a. A precession-driven lunar dynamo model. Geophys. Res. Abs. 16, EGU2014-8914-2011.

Tian, B.Y., Stanley, S., Tikoo, S.M., Weiss, B.P., 2014b. A precession-driven lunar dynamo. Science submitted.

Tikoo, S.M., Weiss, B.P., Buz, J., Lima, E.A., Shea, E.K., Melo, G., Grove, T.L., 2012. Magnetic fidelity of lunar samples and implications for an ancient core dynamo. Earth Planet. Sci. Lett. 337-338, 93-103.

Tremblay, M.M., Shuster, D.L., Balco, G., 2014. Cosmogenic noble gas paleothermometry. Earth Planet. Sci. Lett. 400, 195-205.

Turner, G., 1971. ^{40}Ar-^{39}Ar ages from the lunar maria. Earth Planet. Sci. Lett. 11, 161-191.

Walker, J.C.G., Klein, C., Schidlowski, M., Schopf, J.W., Stevenson, D.J., Walter, M.R., 1983. Environmental Evolution of the Archean-Early Proterozoic Earth. In: Schopf, J. (Ed.), Earth's Earliest Biosphere: its Origin and Evolution, Princeton Univ. Press, Princeton, NJ, USA. pp. 260-290.

Wanke, H., Wlotzka, F., Baddenhausen, H., Balacescu, A., Spettel, B., Teschke, F., Jagoutz, E., Kruse, H., Quijano-Rico, M., Rieder, R., 1971. Apollo 12 samples: Chemical composition and its relation to sample locations and exposure ages, the two component origin of the various soil samples and studies on lunar metallic particles. Proc. Lunar Sci. Conf. 2nd 1187-1208.

Wasilewski, P., 1981. Magnetization in small iron-nickel spheres. Phys. Earth Planet. Inter. 26, 149-161.

Webb, D.J., 1982. Tides and the evolution of the Earth-Moon system. Geophys. J. Roy. Astr. S. 70, 261-271.

Weigand, P.W., Hollister, L.S., 1973. Basaltic vitrophyre 15597 - an undifferentiated melt sample. Earth Planet. Sci. Lett. 19, 61-74.

Weisberg, S.W., 1985. Applied Linear Regression. John Wiley and Sons, New York.

Weiss, B.P., Lima, E.A., Fong, L.E., Baudenbacher, F.J., 2007. Paleointensity of the Earth's magnetic field using SQUID microscopy. Earth Planet. Sci. Lett. 264, 61-71.

Weiss, B.P., Berdahl, J.S., Elkins-Tanton, L.T., Stanley, S., Lima, E.A., Carporzen, L., 2008. Magnetism on the angrite parent body and the early differentiation of planetesimals. Science 322, 713-716.

Williams, J.P., Nimmo, F., 2004. Thermal evolution of the Martian core: Implications for an early dynamo. Geology 32, 97-100.

Wood, J.A., 1964. The cooling rates and parent planets of several iron meteorites. Icarus 3, 429-459.

Yu, Y., Tauxe, L., 2006. Acquisition of viscous remanent magnetization. Phys. Earth Planet. Inter. 159, 32-42.

Yu, Y., 2010. Paleointensity determination using anhysteretic remanence and saturation isothermal remanence. Geochem. Geophy. Geosy. 11, Q02Z12.

Zhang, N., Parmentier, E.M., Liang, Y., 2013. A 3-D numerical study of the thermal evolution of the Moon after cumulate mantle overturn: The importance of rheology and core solidification. J. Geophys. Res. 118, 1789-1804.